MICRO-LASER ASSISTED MACHINING OF SEMICONDUCTORS AND CERAMICS

Hüseyin Boğaç POYRAZ

PhD Dissertation

Ceramic Engineering

Aug-2011

This study was supported by the US National Science Foundation (NSF) under Grant no. CMMI-0757339

JÜRİ VE ENSTİTÜ ONAYI

Hüseyin Boğaç POYRAZ'ın **"Micro-Laser Assisted Machining of Semiconductors and Ceramics"** başlıklı **Seramik Mühendisliği** Anabilim Dalındaki, Doktora Tezi 02.08.2011 tarihinde, aşağıdaki jüri tarafından Anadolu Üniversitesi Lisansüstü Eğitim-Öğretim ve Sınav Yönetmeliğinin ilgili maddeleri uyarınca değerlendirilerek kabul edilmiştir.

	Adı-Soyadı	**İmza**
Üye (Tez Danışmanı) :	**Doç. Dr. ENGİN TIRAŞ**	**………**
Üye :	**Prof. Dr. AYDIN DOĞAN**	**………**
Üye :	**Prof. Dr. RIDVAN SAY**	**………**
Üye :	**Doç. Dr. R. MUSTAFA ÖKSÜZOĞLU**	**………**
Üye :	**Yard. Doç. Dr. SERTAÇ EROĞLU**	**………**

Anadolu Üniversitesi Fen Bilimleri Enstitüsü Yönetim Kurulu'nun……………… tarih ve ………… sayılı kararıyla onaylanmıştır.

Enstitü Müdürü

ÖZET

Doktora Tezi

YARI İLETKENLERİN VE SERAMİKLERİN MİKRO LAZER DESTEKLİ İŞLENMESİ

Hüseyin Boğaç POYRAZ

Anadolu Üniversitesi
Fen Bilimleri Enstitüsü
Seramik Mühendisliği Ana Bilim Dalı

Danışman: Doç. Dr. Engin TIRAŞ

2011, 178 sayfa

Bu doktora tezinin amaci; çok sert ve son derece kırılgan olduğundan geleneksel yöntemler ile işlenmesi çok zor olan Si ve SiC gibi seramikler ve yarı iletkenler için mikro (μ) Lazer Destekli İşlemenin (LAM) hassas işleme sürecine sağladığı potensiyel iyileştirmeyi belirlemektir. μ-LAM sistemi tasarlanmış, kurulmuş, test edilmiş ve değerlendirilmiştir. Deneyler, yarı iletken ve seramik altlıklar üzerine lazer ısıtma ve termal yumuşatmadan kaynaklanan işleme sürecindeki etkiyi ve gelişmeyi değerlendirmek üzere yapılmıştır. Temel bilim ve deneysel hipotez, kesici uç ile temas halinde olan altlık malzemenin lazer ile tercihli olarak ısıtılmasıdır. Bu ısıtma, altlık malzemenin termal yumuşaması ile sonuçlanan deformasyon bölgesinde (çip formasyonu ve malzeme giderme) oluşur ve bu işleme kuvvetlerini azaltarak kesici uç ömrünü uzatır. Yeni geliştirilen bu μ-LAM teknolojisi ile, lazer ısıtma kullanarak malzeme deformasyon süreci boyunca Si ve SiC ün yüksek basınçtaki fazının tercihli olarak ısıtılabileceği ispatlanmıştır. Bölgesel ısıtmadan kaynaklanan termal yumuşatma etkisi sünekliği arttırır ve böylece malzemenin işlenebilirliğini geliştirir.

Anahtar Kelimeler: Lazer destekli işleme (LAM), lazer ısıtma, sünek rejimde işleme, yüksek basınç faz dönüşümleri (HPPT)

ABSTRACT

PhD Dissertation

MICRO-LASER ASSISTED MACHINING OF SEMICONDUCTORS AND CERAMICS

Hüseyin Boğaç POYRAZ

Anadolu University
Graduate School of Sciences
Ceramic Engineering Program

Supervisor: Assoc. Prof. Dr. Engin TIRAŞ

2011, 178 pages

The aim of this PhD dissertation is to determine the potential enhancement that micro (µ) Laser Assisted Machining (LAM) provides to the precision machining process for semiconductors and ceramics such as, Si and SiC, which are typically very hard and extremely brittle and therefore very difficult to machine by conventional methods. The µ-LAM system has been designed, built, tested and evaluated. Experiments were conducted on semiconductor and ceramic wafers to evaluate the effect and improvement to the machining process resulting from the laser heating and thermal softening. The underlying science and experimental hypothesis are that the laser is selectively heating the work piece material in contact with the cutting tool. This heating occurs in the deformation zone (chip formation and material removal) resulting in thermal softening of the work piece material and leading to reduced machining forces and improved tool life. It has been demonstrated by this novel µ-LAM technology that it is feasible to preferentially heat the high pressure metallic phase of Si and SiC during the material deformation process using laser heating. The thermal softening effect resulting from the localized heating enhances the ductility, and thus improves the material’s machinability.

Key Words: Laser-Assisted Machining (LAM), laser heating, ductile regime machining, high pressure phase transformation (HPPT)

ACKNOWLEDGEMENTS

Though only my name appears on the cover of this dissertation, a great many people have contributed to its production. I owe my gratitude to all those people who have made this dissertation possible and because of whom my graduate experience has been one that I will cherish forever.

First of all, I would like to thank my home university (Anadolu University, Turkey) and my home department (Materials Science & Engineering Dept.) to give this opportunity to do my PhD research studies in USA.

My deepest gratitude is to my advisor from USA, Dr. John A. Patten, who has guided me, inspired me and encouraged me throughout my thesis with his invaluable patience, advice and knowledge. It has been a good opportunity and a great learning experience for me to work with Dr. John A. Patten. His patience and support helped me overcome many crisis situations on this project. I am deeply grateful to him for the long discussions that helped me sort out the technical details of my work. His expertise knowledge on the topic of high pressure phase transformations, ductile machining of brittle materials and laser-assisted machining has been a great source of discussion. Numerous discussions and lectures on related topics helped me improve my knowledge in the area.

My co-advisor from Turkey, Dr. Engin Tıraş, has been always there to listen and give his advice. Dr. Engin Tıraş has guided me not only through technical advice on the research project, he also helped me understand what a Ph.D. student should achieve in general.

I would like to thank my advisory committee members, Dr. Rıdvan Say and Dr. Aydın Doğan, for their valuable suggestions on my research project. I would also like to thank Dr. R. Mustafa Öksüzoğlu and Dr. Sertaç Eroğlu for serving as defense committee members.

I gratefully acknowledge Co-PI of the NSF project, Dr. Muralidhar Ghantasala for his many valuable suggestions on this project and his generosity of allowing my extensive usage of the equipments in his lab.

I also would like to extend my sincere thanks to Deepak Ravindra, who is one of the members of Dr. Patten's research team, for being part of this project and making this research a success.

I would like to thank Glenn Hall (machine shop laboratory technician) for machining some parts for the experimental apparatus. I would also like to thank the following individuals for their noted contributions: Dr. David Gosztola from Center for Nanoscale Materials (CNM) at Argonne National Laboratory (ANL) for his help on the micro-Raman spectroscopy work; Nobuo Imaizumi and Akinori Sugimura from Adamant Kogyo Company Limited in Japan for their contribution on the μ-LAM project; Dr. Rob Eversole at WMU imaging center for allowing me to use the scanning electron microscope (SEM) at WMU Imaging Center; Dr. Richard Hathaway for lending me some instruments of his and allowing me to use the optics laboratory for some of my tests; Dr. Lei Dong for providing instructions on how to operate the laser system; Subash Gokanakonda for helping me to operate the vapor-deposition coating device.

I also wish to thank the following individuals for help on various aspects of this project and personal encouragement: Lei Dong, Amir Rahimpour Shayan, Saurabh Virkar, Himanshu Lohani and Mayank Garg.

I would like to acknowledge USA Department of Energy (DoE) National Science Foundation (NSF) (Grant#: CMMI-0757339) and Michigan Universities Commercialization Initiative (MUCI) for funding this project.

I am also grateful to the following former or current staff at Western Michigan University, for their various forms of support during my PhD study; Sue Ketchum (Administrative Specialist at WMU College of Engineering & Applied Sciences), Barbara Wygant (Research & Program Officer at WMU College of Engineering & Applied Sciences), Hanna Wells (Office Coordinator at WMU College of Engineering & Applied Sciences) and Tamara Bergman (Office Associate at WMU College of Engineering & Applied Sciences).

Most importantly, none of this would have been possible without the love and patience of my family. My immediate family to whom this dissertation is dedicated to, has been a constant source of love, concern, support and strength all these years. I would like to express my heart-felt gratitude to my family.

TABLE OF CONTENTS

LIST OF FIGURES

LIST OF TABLES

1. INTRODUCTION

Engineering materials are usually classified into five groups: metals, ceramics, polymers, semiconductors, and composite materials [1]. Each type of material has different structures and properties, which subsequently determines their engineering applications. Semiconductors and ceramics share the common characteristics of being nominally hard and brittle, which stem from their covalent chemical bonding and crystal structure. Both types of materials are important in many engineering applications, but they are particularly difficult to machine in traditional manufacturing processes due to their extreme hardness and brittleness.

Advanced ceramics and semiconductors (i.e. SiC, Si, etc.) are increasingly being used for industrial applications. These ceramics/semiconductors are hard, strong, inert, and light weight. This combination of properties and the unique electrical behavior of semiconducting materials make them ideal candidates for tribological, semiconductor, MEMS and optoelectronic applications and electronic devices such as transistors, diodes, and integrated circuits. Ceramic materials have many desirable properties, like excellent wear resistance, chemical stability, and high strength even at elevated temperatures. These outstanding properties make them good candidates for long lasting components in harsh or extreme working environments, such as seals and bearings in engines [2].

In many engineering applications products require a high quality surface finish and close tolerances to function properly. This is often the case for products made of semiconductor or ceramic materials. Manufacturing these materials without causing surface and subsurface damage is extremely challenging due to their high hardness, brittle characteristics and poor machinability and it remains a major obstacle that limits the wider application of these materials. The plastic deformation in these brittle materials at room temperature is much less or at a smaller size scale, than in metals, which means they are prone to fracture during material deformation and removal processes. Surface cracks generated during machining are routinely and subsequently removed via lapping and polishing, which significantly increases the machining cost [3]. When it comes to ultra fine surface machining, such as precision machining, the surface of an optical lens or mirror, developing a cost effective method to achieve a fracture free surface presents great challenges. Machining mirror-like surface finishes contribute significantly to the total cost of a part. In some cases, grinding alone can account for 60-90% of the cost of final product [2].

Semiconductor and ceramic materials are amongst the most challenging to machine. When attempting to machine ceramics such as silicon carbide (SiC), especially to improve the surface finish, it is important to carry out a 'damage free' machining operation. This often can be achieved by ductile mode machining (DMM) or in other words machining a nominally hard and brittle material in the ductile regime.

In the nanomachining of semiconductors and ceramics, especially brittle materials such as silicon (Si) and silicon carbide (SiC), the presence of high pressure phase transformation (HPPT) is of great importance for accomplishing ductile regime machining [4-7]. To augment the ductile regime machining of these nominally brittle materials, the high pressure phase can be preferentially heated and thermally softened by using concentrated energy sources such as laser beams.

In this study the micro laser assisted machining (μ-LAM) system was designed, built, tested and evaluated. The μ-LAM system can be used to process difficult to machine materials, such as ceramics and semiconductors, which are typically very hard and extremely brittle and therefore not easily formed or shaped. The research objective of this project is to modify the material, in-situ during manufacturing, so as to render these materials easier to machine and make it more cost effective to generate useful end products. The μ-LAM system achieved enhanced ductility through reduced hardness and decreased brittleness resulting from laser heating and thermal softening, to promote a more efficient, productive and less costly overall manufacturing process. LAM processes do not ablate (evaporate) material as in other micro-machining processes, and μ-LAM uses low power laser as contrasted with other LAM processes, which use higher power lasers. The µ-LAM process, which will be discussed in this dissertation, showed positive results in addressing the challenges faced in conventional ductile regime machining of Si and SiC.

2. LITERATURE REVIEW

2.1. Silicon Carbide (SiC)

Silicon carbide (SiC) is a wide band gap semiconductor, which is very promising for many applications in opto and micro-electronics. Its physical properties, such as high breakdown field, high saturated drift velocity and high thermal conductivity, make it an ideal candidate for applications in which high temperature, high radiation intensity, high voltage or high power dissipation are involved [8].

Although SiC has been around since 1891, it was not until the mid-1990's that this material was introduced into the precision manufacturing industry. SiC is well known for its excellent material properties, high durability, high wear resistance, light weight and extreme hardness. However, SiC is also well known for its low fracture toughness, extreme brittleness and poor machinability. All of these properties make SiC an exceptional candidate in harsh environments, such as high temperature, strong radiation, and corrosive and abrasive media.

SiC is commercially available in various forms/phases (polytypes) such as single crystal, polycrystalline (sintered and CVD) and amorphous. Polished single crystal wafers are becoming more common in the high power, high temperature electronics device industry. In the last years, most of the research activities have been focused on 4H and 6H-SiC single crystal polytypes because of the mature bulk crystal technologies. The 4H single crystal SiC wafer is typically used for:

- Optoelectronic Devices
- High-Power Devices
- High Temperature Devices
- High-Frequency Power Devices
- III-V Nitride Deposition [9].

Some of the application fields where SiC is introduced include automobile, aerospace, petroleum, nuclear, military and biological/medical industries. Manufacturing this material is extremely challenging due to its high hardness, brittle characteristics and poor machinability. Severe fracture can result when trying to machine SiC due to its low fracture toughness. However, from past experience it has been proven that ductile regime machining of silicon carbide is possible [5, 10-12].

2.1.1. Crystal Structure

SiC exhibits a one-dimensional polymorphism called polytypism. All polytypes of SiC have an identical planar arrangement of Si and C atoms, which are distinguished by differences in the stacking sequence of the identical planes. Disorder in the stacking periodicity of similar planes results in a material that has numerous crystal structures (polytypes), all with the same atomic composition.

Despite the large number of polytypes, only three crystalline structures exist: cubic, hexagonal and rhombohedral. The origin of the polytypism can be visualized as follows. In Figure 2.1, the solid circles represent spheres closely packed in a plane; which is called as "plane 1". To place another such set of spheres on top of plane 1 as closely as possible, one would place each sphere in the hole between any three neighboring spheres in plane 1 (dotted circles, plane 2). But there is another way of accomplishing this: the dashed circles in plane 3. The order of stacking of the planes determines the types of close-packed structures and their symmetry properties. According to conventional nomenclature, a SiC polytype is represented by the number of Si-C double layers in the unit cell. The appending letter C, H, or R indicating a cubic, hexagonal or rhombohedral symmetry. For example, the 6H hexagonal lattice has six layers in the primitive cell with the following succession of the upper planes: 1,2,3,1,3,2,1,2,3,1,3,2; the 3C lattice is built up as 1,2,3,1,2,3; 2H-SiC corresponds to 1,2,1,2; and 4H-SiC corresponds to 1,2,1,3,1,2,1,3. [13].

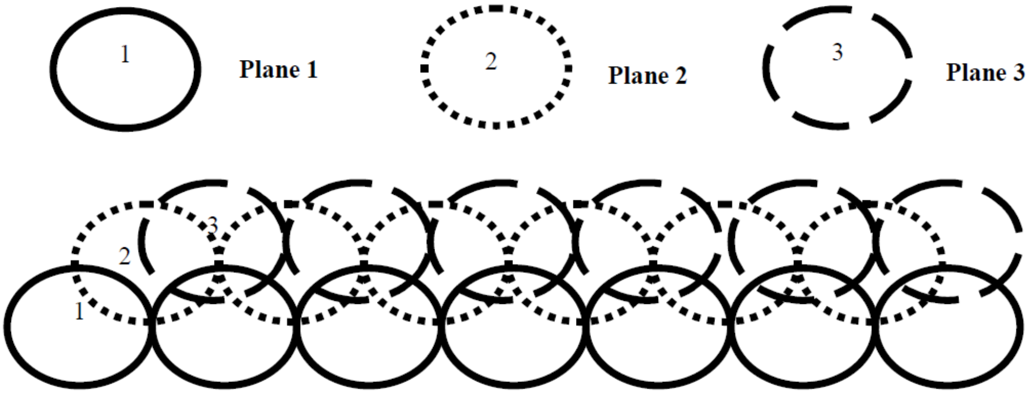

Figure 2.1. Schematic diagram of atomic arrangements in the different SiC polytypes.

In the case of SiC, the basic units are tetrahedrons with a C (Si) atom at the center, surrounded by four Si (C) atoms covalently bonded. These units are periodically repeated in closed-packed hexagonal layers, whose stacking sequence gives rise to the different polytypes. With reference to Figure 2.2, if the first Si-C layer is labelled A, the next layer that can be placed according to a closed packed structure that will be placed either on B or C. The different polytypes are constructed by permutations of these three positions. In Figure 2.2 the stacking sequence is shown for the four most common polytypes of SiC; 2H, 3C, 4H and 6H.

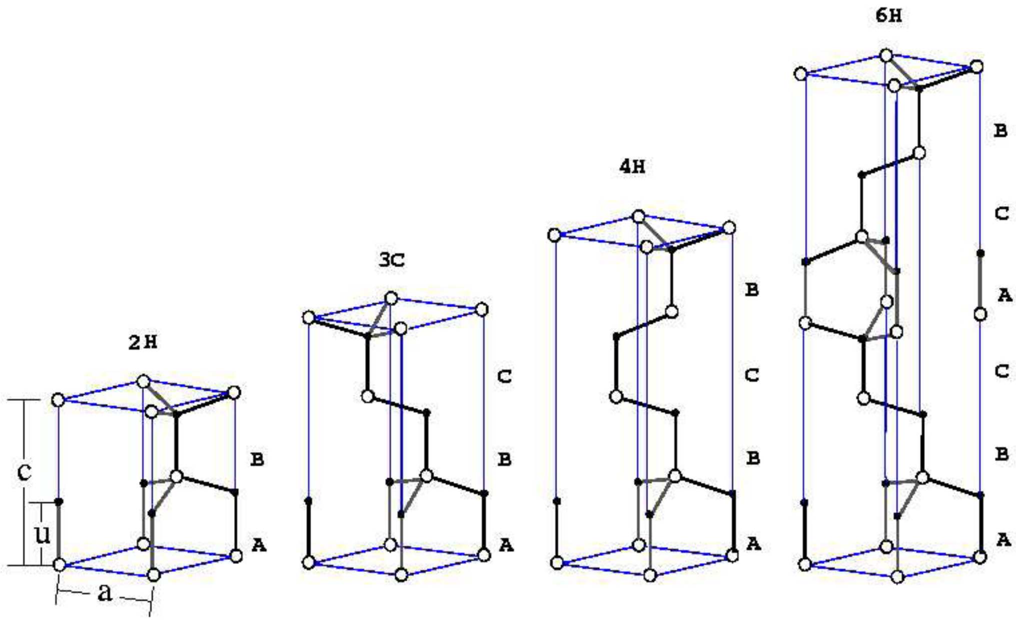

Figure 2.2. Schematic representation of the stacking sequence of hexagonal SiC bilayers for 2H, 3C, 4H and 6H polytypes.

2.1.2. Physical Properties

Owing to the different arrangement of Si and C atoms within the SiC crystal lattice, each SiC polytype exhibits unique fundamental electrical and optical properties. Some of the most significant electrical properties of the 3C, 4H and 6H SiC polytypes are given in Table 2.1, where Si and GaAs are also reported as a reference.

Table 2.1. Comparison of selected electronic properties of major SiC polytypes, Si and GaAs [13]. (The electron mobility and the hole mobility refer to a doping concentration of about 10^{16} cm^3 of donors and accpetors respectively).

Property	Si	GaAs	4H-SiC	6H-SiC	3C-SiC
Band Gap (eV)	1.1	1.4	3.2	3.0	2.3
Breakdown Field (MV/cm)	0.6	0.6	$\parallel$ c: 3.0	$\parallel$ c: 3.2 $\perp$ c: > 1	> 1.5
Thermal Conduct. (W/cm-K)	1.5	0.5	3.0-5.0	3.0-5.0	3.0-5.0
Intrinsic carrier concentration (cm^{-3})	10^{10}	1.8 10^6	$\sim 10^{-7}$	$\sim 10^{-5}$	~ 10
Electron Mobility (cm^2/V-s)	1200	6500	$\parallel$ c: 800 $\perp$ c: 800	$\parallel$ c: 60 $\perp$ c: 400	750
Hole Mobility (cm^2/V-s)	420	320	115	90	40
Saturated Electron Velocity (10^7cm/s)	1.0	1.2	2	2	2.5

The most common SiC polytypes exhibit advantages and disadvantages in basic material properties of SiC over Si listed in Table 2.1. The most beneficial inherent material superiorities of SiC over Si are its exceptionally high breakdown electric field, wide band gap energy, high thermal conductivity, and high carrier saturation velocity. For instance, the band gap for SiC ranges from 2.3eV for 3C-SiC to 3.2eV for 4H-SiC [13].

SiC has always been noted for its excellent mechanical properties, specifically, hardness and wear resistance. In terms of hardness, SiC has a Mohs hardness of 9, which compares favorably with values for other hard materials such as diamond (ten) and topaz (eight). In terms of wear resistance, SiC has a value of 9.15, as compared with 10.00 for diamond and 9.00 for Al_2O_3. SiC is not attacked by most acids and it can only be etched by alkaline hydroxide bases (i.e. KOH) at molten temperatures (> 600°C). SiC does not melt, but sublimes at about 1800°C. The surface of SiC can be passivized by the formation of a thermal SiO_2 layer, even though the oxidation rate is very slow when compared with Si. The above properties are not generally polytype dependent.

2.2. Machining Processes

The manufacturing processes such as casting, forming, joining, etc. are extensively used in the industry. However, most of the shapes manufactured by these processes must be subjected to secondary processes for converting them into useful fully finished products. One of the most important secondary processes is the machining process. Machining involves removal of material from a workpiece for converting it into the desired shape with size and tolerances per design specification. It is difficult to imagine a manufactured product which does not require machining for at least one of its components. Since the machining adds value to the finished product, material removal processes have gained considerable importance to control the overall economics of the process. Large number of machining processes have been developed and used with varying degree of success for machining different materials. Still, one machining method might be exceptionally good for one material and it may be totally unacceptable for another in terms of machining cost and quality.

The machining processes have been broadly categorized into traditional and nontraditional machining processes based on the mechanism of material removal [14].

2.2.1. Traditional Machining Processes

Conventional machining involves material removal due to mechanical stresses, exceeding the strength of the material, induced by the tool. The basic machining mechanism involves the localized shear deformation on the workpiece material ahead of the cutting edge of the tool. The material is removed in the form of a chip formed by deformation along the successive shear planes which are inclined to the cutting direction. The process is analogous to the sliding of cards ahead of the cutting edge of the tool (Figure 2.3). The two deformation zones in metal cutting are identified as primary and secondary deformation zones. The primary deformation zone is due to shear deformation ahead of the cutting tool due to compression of the workpiece material during cutting action, whereas the secondary deformation zone is due to shear and sliding of the chip as it passes over the rake face of the cutting tool [15].

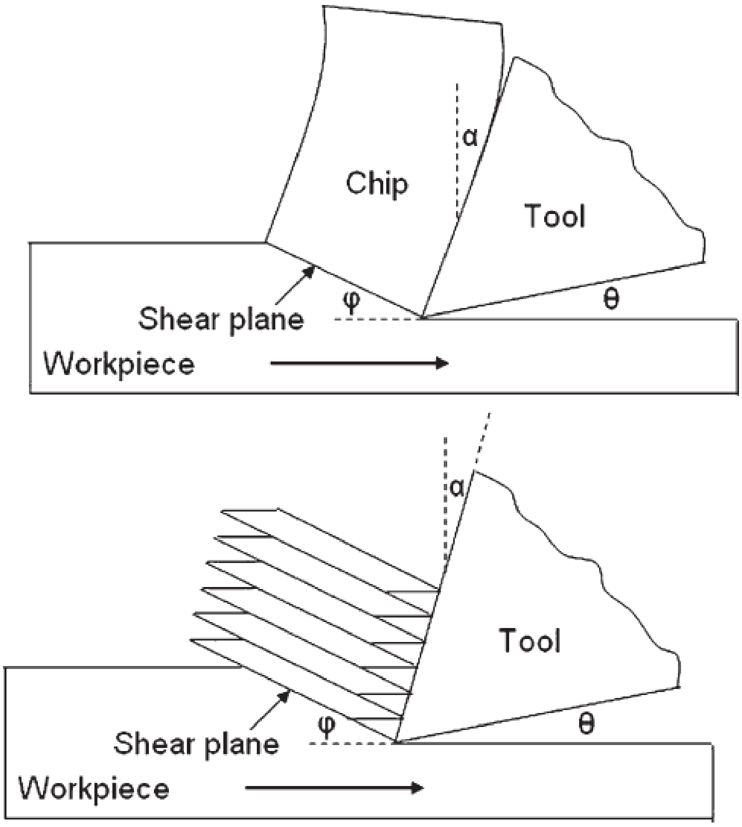

Figure 2.3. Schematic model of the orthogonal geometry and chip formation during machining [15].

A large variety of material removal processes are used in industrial practices primarily based on processes like turning, drilling, milling, shaping, abrasive machining, sawing, etc (see Figure 2.4) [16-18].

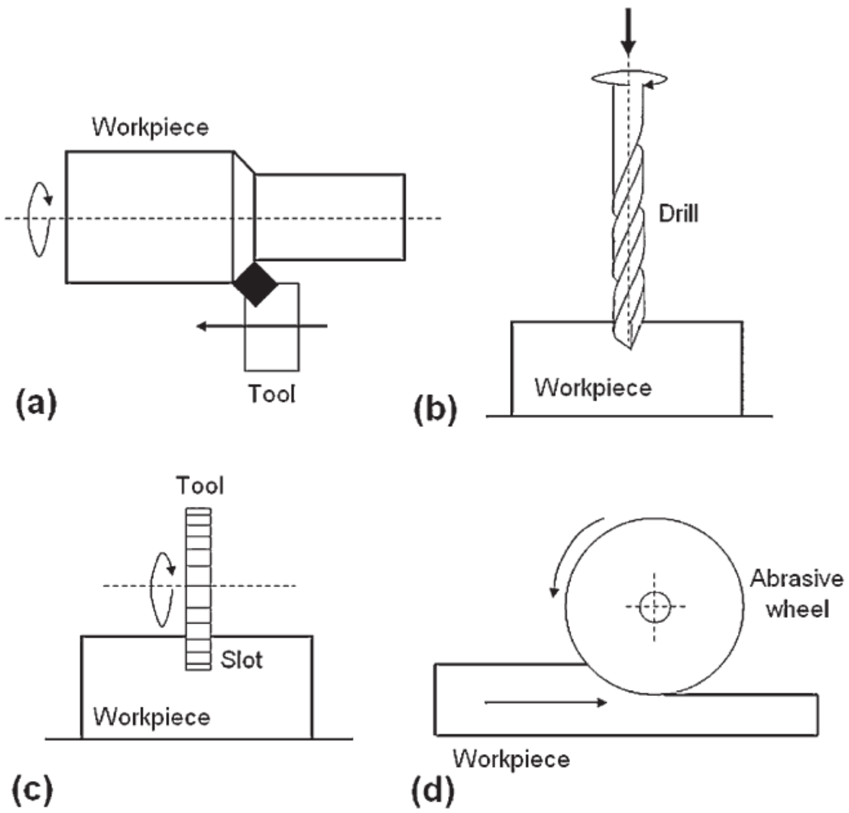

Figure 2.4. Schematic of some of the common traditional machining processes:

(a) turning,

(b) drilling,

(c) milling, and

(d) grinding. [16-18].

2.2.2. Nontraditional Machining Processes

Nontraditional machining processes have evolved to meet the special machining needs for use in situations that the conventional machining proves unsatisfactory, both in terms of economics and achievable machining quality. Most of these needs come from the rapid technological advancement in the areas of materials development for advanced applications in aerospace, automotive, and nuclear power industries. Increasing development and utilization of super-hard, high-strength, high-temperature, and high-performance materials in these applications is increasingly demanding complex machining requirements for difficult-to-machine materials. Some of these difficult-to-machine materials are titanium, nimonics, metal matrix composites, advanced ceramics, aluminides, etc. Conventional machining is limited mainly due to unavailability of ultrahard tool material for economical machining of these difficult-to-machine materials. In most of the cases, nontraditional machining is the most economical and effective way of machining these materials [19].

Nontraditional machining processes are generally considered to be manufacturing processes that use common energy forms in new ways or that applies new forms of energy. Nontraditional machining processes are categorized based on the form of energy employed such as mechanical, electrical, thermal, and chemical. Table 2.2 lists the details of nontraditional machining processes [20].

Table 2.2. Various nontraditional machining processes [20].

Class	Mechanism	Examples
Mechanical	Materials removal due to abrasive action of powder particles, water, slurry, etc.	Abrasive jet machining Waterjet machining Abrasive waterjet machining Ultrasonic machining
Electrical	Material removal in the electrolyte due electrochemical reactions	Electrochemical machining Electrochemical grinding Electrochemical discharge grinding
Thermal	Material removal using electrical sparks, electrons, photons, etc.	Electrical discharge machining Electron beam machining Laser beam machining
Chemical	Material removal due to chemical action	Chemical milling Photochemical machining

In thermal methods of machining, high energy source concentrates energy on a small area of the workpiece so that the material removal takes place by localized melting and/or evaporation. The various energy sources may be electrons, photons, electrical sparks, etc. The material removal rate is independent of the hardness and strength of the material and hence the thermal methods are often applied for machining extremely hard and difficult-to-machine materials.

2.3. Precision Machining of Semiconductor and Ceramic Materials

In many engineering applications, products require a high quality surface finish and close tolerances to function properly. This is often the case for products made of semiconductor or ceramic materials. For example, the surface finish and subsurface quality of a silicon wafer are required to be defect-free in order to obtain a properly functioning final device [21].

On the other hand, semiconductor and ceramic materials are known to be difficult to machine due to their high hardness and brittleness. Some ceramics are even unmachinable using conventional machining processes [22]. The physical properties that make them desirable, particularly their high strength and high hardness at elevated temperature, also make them difficult to machine.

Currently, fine grinding, lapping and polishing are typically used to obtain smooth fracture-free surfaces for semiconductor and ceramic materials. These machining methods are capable of producing satisfactory surface finish, but they are costly processes in terms of tool cost and machining time. Consequently, machining these mirror-like surface finishes contribute significantly in the total cost of a part. In some cases, grinding alone can account for 60-90% of the final product [23]. The real challenge is to produce an ultra-precision surface finish in these nominally brittle materials at low total machining cost.

Current problems for brittle material machining include the high cost of machining and product reliability. The cost is mainly due to the high tool cost, rapid tool wear, long machining time, low production rate and the manufacturing of satisfactory surface figure and form. The low product reliability is primarily due to the occurrence of surface and subsurface damage and brittle fracture. To overcome these obstacles, developing advanced precision machining techniques become critical for cost effective production. Ductile regime machining method, a very promising precision machining process, has been continuously studied in the last several decades [4-7, 24-31]. Cost effective methods for precision part machining continues to be a critical issue.

2.4. High Pressure Phase Transformations (HPPT) in Semiconductor and Ceramic Materials

Knowledge of phases and phase transformations is a prerequisite for understanding materials and their properties. In materials science, phase is defined as a homogenous part of a system [32]. A crystal change to a new or different structure is called a phase transformation. Phase transformations involve liquids to solids, solids to solids, etc. changes. The subject of phase transformations herein, is limited to crystal structure changes in solid-state semiconductor materials and ceramics. The size and distribution of the phases present in a multi phase material, together with grain and grain boundaries, affect the material's properties [32].

Pressure and temperature are the two most important external variables that affect a material system comprising a single pure material. For a polycrystalline solid, the grain size is also equally important. At high pressures, new and sometimes unexpected chemical and physical events occur [33], such as the production of man-made diamond. Material within this transformed zone behaves quite different from the bulk because of the change in the crystal structure under high pressure.

Over a specific range of pressure and temperature, some phase transformations are reversible while some are not [34]. For example in silicon, it has been demonstrated that the HPPT is a reversible process between the amorphous phase and the β-tin phase [35, 36]. Amorphous silicon resulted from rapid unloading of β-tin phase transforms back to β-tin phase upon subsequent loading cycles [37]. There are thirteen high pressure phases of silicon discovered so far during loading/unloading processes in high pressure experiments, such as an indentation tests and diamond anvil cells (DAC). The crystal structures and phase transformation pressure regions of the high pressure phases of silicon (Si) commonly observed in compression tests [38] are listed in Table 2.3.

Table 2.3. High pressure phases of Si.

Phase	Structure	Pressure region (GPa)
Si-I	Cubic diamond	0~11
Si-II	Body-centeredTetragonal (β-Sn)	~11-15
Si-III	Body-centerd cubic	~10-0*
Si-V	Primitive hexagonal	~14-40
Si-VII	Hexagonal close-packed	~40

** formed during unloading of Si-II.*

The term HPPT as used here, refers to the crystalline structural change (phase change) in covalent materials within the contact interface or surface layer of the material due to an externally applied pressure (>6GPa), and in the presence of an accompanied shear stress (as occurs in indenting, scratching, and machining) [39]. Unlike the classical concepts of phase and phase transformations in metallurgy (which are generally composition and temperature dependent, and that generally occur at atmospheric pressure or sometimes in a vacuum), the HPPT in this study is a localized surface and subsurface phenomenon [20]. The size scale of these HPPT in semiconductors and ceramic materials is limited from nanometers to micrometers in extent [40]. Beyond this size scale, these materials usually exhibit a brittle rather than a ductile response, i.e. the ductile to brittle transition (DBT) [41]. The most studied materials that experience HPPT include some common semiconductor materials, such as silicon and germanium, and ceramic materials such as silicon nitride and silicon carbide [42]. For example, silicon and silicon carbide may undergo HPPT in the size range from a few nanometers to a few hundred nanometers in extend, i.e. in the nanotechnology realm, generally measured as a depth from or beneath the surface [5]. Silicon nitride may experience a HPPT at a larger size scale, up to 40 micrometers in extent or depth [4]. The pressure that is applied to induce such phase transformations is usually on the order of the material's hardness (approximately 10 to 30 GPa for the materials of interest). This agreement between the two characteristic pressures in fact reveals the internal relationships between them. The measured hardness of these materials is in essence equivalent to the semiconductor-metallic transition pressure [43], and indicates that the measured hardness is in actuality associated with the HPPT.

The HPPT is the origin of the ductile removal mechanism in semiconductor material machining processes at room temperature [26]. During machining of silicon and germanium, the material under the diamond tool transforms from the semiconducting covalent phase to a high pressure metallic phase when the contact pressure reaches the phase transformation pressure, i.e corresponding to the material's hardness [44]. In theory and in practice, the high pressure metallic phase of silicon is ductile while the covalent phase is ideally brittle [45].

Covalent materials tend to be difficult to deform at low pressure and low temperature conditions [46]. Increasing the temperature helps improve the material's plastic deformation, by assisting dislocation mobility [22]. If the pressure is high enough to generate the HPPT in covalent materials, then plastic deformation of the high pressure metallic phase can be achieved at low temperature, such as room temperature [47].

HPPT research is of the interest because of its scientific value as well as its practical use. Some of the beneficial material properties associated with or resulting from HPPT are advantageous for precision manufacturing processes due to the enhanced material ductility. For example, in some semiconductor and ceramic materials, under a pressure within the range of the material's hardness, a metallic phase develops that exhibits high electrical conductivity that is comparable to a metal [48]. This high pressure metallic phase, as contrasted to the material's normal brittle covalent phase, provides for or enhances the material's plastic deformation behavior and even helps to prevent or minimize fracture [49]. Furthermore, the metallic nature of the high pressure phase, such as its enhanced electrical conductivity, can be selectively used in novel ways to enhance the ductile response [50].

Normally in the process of the HPPT in semiconductor and ceramic materials, more than one new phase is generated under different loading/unloading conditions [51-54]. The one HPPT that has caused the most interest is the covalent-to-metallic phase transformation. This β-tin phase, referred to as Si-II for silicon, is the first and most likely HPPT to occur in semiconductors and ceramics during mechanical deformation processes, such as indenting, scratching and machining [36]. This phase transformation (from Si-I to Si-II) is given special attention, from the machining point of view, due to its potential to provide and account for the observed ductility of this normally brittle material. The high pressure metallic phase of silicon (β-tin or Si-II phase) is softer and more ductile than the diamond cubic covalent Si-I phase [55], which explains its role in the ductile regime processing, such as indenting, scratching and machining.

The HPPT phenomenon in semiconductor and ceramic materials has been investigated for over 50 years, mostly in the fields of physics and materials science. Under very high pressures, comparable to their hardness, many covalent materials transform to a metallic state [56]. X-ray diffraction studies showed a series of phase transformations depending on the material and their deforming conditions, among which the most representative one was the covalent-to-metallic phase transformation [57, 58]. With the advent of powerful analytical tools, such as AFM, SEM, TEM, x-ray diffraction and Raman Spectroscopy, the knowledge and understanding of HPPT have increased significantly. Experimental studies show that this covalent-to-metallic phase transformation takes place in the machining process of many other semiconductor crystals, compounds and ceramic materials [59].

2.4.1. Instruments Used in HPPT Research

High pressure experimental techniques, and the associated instrumentation, are important research fields. The world-respected high pressure research pioneer during the first half of 20th century was P.J. Bridgman, who invented many apparatus and instruments that could achieve high pressures (up to 400,000 atm) to study the behavior of materials at high pressure. The first man-made diamond in 1954 was also a milestone for the high pressure research community [37, 38]. Today, there are numerous instruments and devices developed to obtain very high pressures for all kinds of purposes.

In physics and materials science, high pressure research is a fundamental tool to study the deformation mechanism and physical material properties. Three types of devices are frequently adopted by researchers in the field of HPPT of semiconductor and ceramic materials, these are:

- the Diamond Anvil Cell (DAC),
- nanoindenter,
- scratching/scribing equipment and

The core design concept in all these three devices is basically the same; the contact area is made extremely small (μm^2), so that a relatively small normal load (mN) can generate very high pressures (GPa) over the contact area.

2.4.2. Evidence of HPPT in Semiconductor and Ceramic Materials

The widely accepted experimental evidence for the covalent to metallic transformation is the electrical conductivity measurement during diamond anvil cell (DAC) or indentation, and the load versus displacement curves from indentation hardness measurements. The increased electrical conductivity and decreased hardness (or actually the measured hardness) are also indicative of a covalent to metallic HPPT. Direct observation through X-ray crystal structure measurement in DAC is another method of the existence of covalent-metallic phase transformation.

There are additional evidences of the metallic high pressure phase of silicon from post process analysis using micro-Raman and TEM [53, 54, 55]. From micro-Raman analysis, Si-XII and Si-III phases are detected, which are the result of a back transformation of Si-XII from Si-II. This confirms the existence of β-tin Silicon because in order to generate Si-XII (and then Si VII and Si III), Si-II or the β-tin phase has to be present as a precursor.

2.5. Ductile Regime Machining of Semiconductor and Ceramic Materials

Ductile regime machining of brittle materials has been studied for the last 25 years. The knowledge of ductile machining of brittle materials was originally gained from practical experience, i.e., trial-and-error. It was known that ductile regime machining of these materials could be achieved within a particular range or set of machining conditions, namely, feed, depth of cut, cutting edge radius and rake angle. Size dependent (scale effect) brittle to ductile transition in crystals was particularly noticed [60]. However, there was a lack of a scientific or theoretical explanation for the observed ductile behavior of these nominally brittle materials.

In 1991, Bifano, T.G. Dow and R.O. Scattergood reported their new technology: ductile-regime grinding [61]. Fracture-free surfaces were obtained in germanium and thus for the first time demonstrated that ductile machining of a brittle material could be achieved. According to the grinding research carried out by Bifano et al. in 1991, there are two types of material removal mechanisms associated with the machining process: ductile; plastic flow of material in the form of severely sheared machining chips, and brittle; material removal through crack propagation. This previous research discusses several physical parameters that influence the ductile to brittle transition in grinding of brittle materials. The researchers were successful in performing ductile mode grinding on brittle materials. However, these researchers did not propose or confirm a model or suitable explanation for the origin of this ductile regime. Bifano et al. also proposed a model defining the ductile to brittle transition (DBT) of a nominally brittle material based on the material's brittle fracture properties and characteristics. A critical depth of cut model was introduced based on the Griffith fracture propagation criteria. The critical depth of cut ($d_{c)}$ formula is as follows:

$$d_c = (E \cdot R) / H^2 \tag{2.1}$$

where E is the elastic modulus, H is the hardness and R is the fracture energy. The value of the fracture energy (R) can be evaluated using the relation:

$$R \sim K_c^2 / H \tag{2.2}$$

where K_c is the fracture toughness of the material. The above two equations can be combined to represent the critical depth (d_c) as a measure of the brittle transition depth of cut:

$$d_c \sim (E / H) \cdot (K_c / H)^2 \tag{2.3}$$

The researchers were successful in determining a correlation between the calculated critical depth of cut and the measured depth (grinding infeed rate). The constant of proportionality was estimated as to be 0.15 and this is now added into Equation (2.3) to generate a more accurate empirical equation:

$$d_c \sim 0.15 \cdot (E / H) \cdot (K_c / H)^2 \tag{2.4}$$

The breakthrough came in 1995, when Morris *et al*. published a paper [26] stating that ductile machining of germanium had been achieved. The authors asserted that the high pressure phase transformation (HPPT), to a metallic phase that was presumed to be ductile, accounts for the ductile mode deformation during precision machining of brittle materials, such as semiconductors and ceramics. More recently, collective work from a group of researchers confirms achieving ductile machining in silicon and some other brittle materials, most notably silicon nitride and silicon carbide [5, 30, 31, 62, 63]. This work and subsequent studies indicate that the HPPT produces a high pressure metallic phase, which deforms plastically in the precision machining process when the depth of cut is small enough to avoid brittle fracture, i.e., below the ductile to brittle transition (DBT).

In ductile regime machining of brittle materials (in particular covalently bonded semiconductors and ceramics), given the proper combination of tool geometries and machining parameters, there is a metastable intermediate high pressure metallic phase generated in front of and under the tool, referred to as the β-tin phase (due to a resulting crystal structure similar to tin). This new phase is shown to possess physical properties similar to metals, such as plastic deformation and high electrical conductivity compared to covalent materials [64].

These new scientific findings have since opened up promising scientific and engineering research opportunities in precision machining of semiconductor and ceramic materials. To date, ductile machining of silicon, germanium, silicon nitride and silicon carbide has already been successfully achieved in laboratory studies [4, 5, 26, 29-31, 62, 63]. It appears increasingly promising to apply these experimental laboratory scale processes to mass production applications in industry.

2.5.1. Mechanism of Ductile Regime Machining in Semiconductor and Ceramic Materials

Previously, the mechanism used to explain the material removal mode for brittle materials was based upon brittle fracture processes (crack initiation and propagation). The breakthrough came when plastic deformation and curly chips were observed to dominate the ductile cutting process [57]. Brittle fracture mechanisms cannot explain the observed ductile chips. With the previous background provided, it is clear that the ductile-machining of semiconductors and ceramics is possible and feasible. Numerous studies have shown ductile chip formation and fracture-free surfaces generated using ductile-machining [26, 58, 59]. Figure 2.5 shows an example of ductile chips formed from Si_3N_4. Many other authors have demonstrated similar chip morphology for silicon and germanium [64]. Figure 2.6 shows an SEM photomicrograph illustrating a typical silicon chip turned in the ductile regime [65]. In several studies ribbon-like chips are formed during cutting in the same way as is observed when ductile metals are cut.

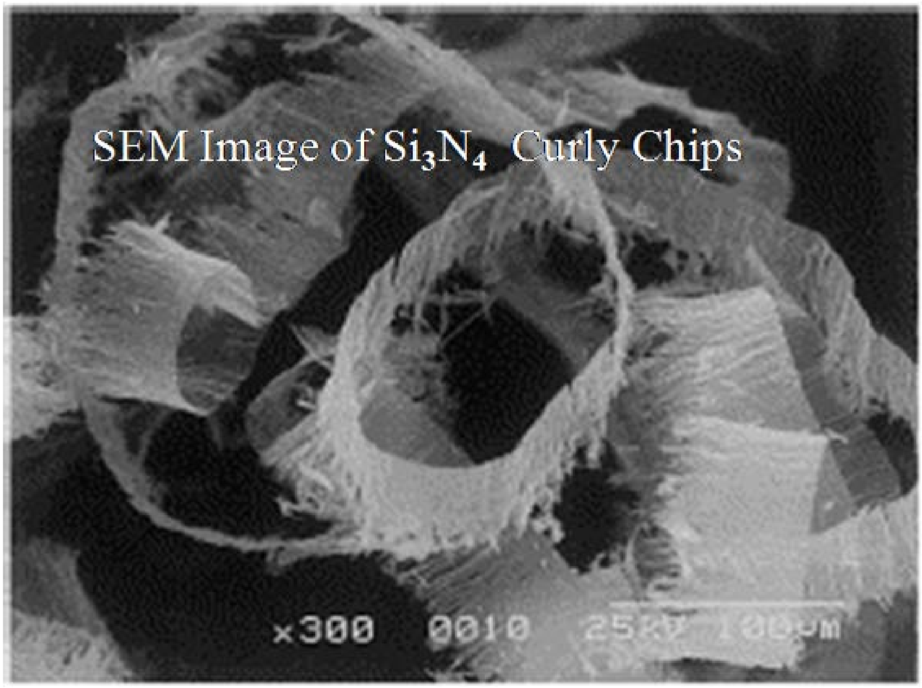

Figure 2.5. SEM micrograph of an Si_3N_4 ductile chip [64].

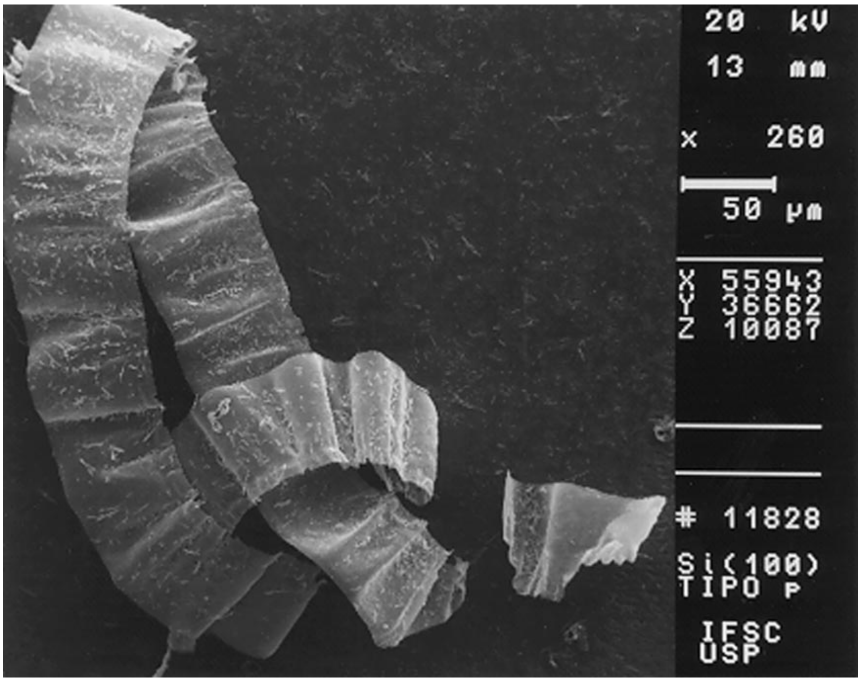

Figure 2.6. Photomicrograph of typical ribbon-like Silicon machining chip which demonstrates that the chip formation mechanism involves plastic deformation and shear [65].

For metals, dislocation based plastic deformation mechanisms prevail, i.e., chips are formed and separated from the bulk work piece through a shear deformation process [66]. But in the case of brittle materials, fracture dominates the material removal mode for most machining or material removal processes, e.g. grinding [67]. Brittle chips are usually formed when machining semiconductors and ceramics, and subsequent material removal occurs due to the material fracturing. Surface fracture can extend beneath the surface, creating sub-surface damage such as cracks. The ductile regime machining behavior of nominally brittle materials could not be rationalized based upon these fracture process mechanisms, because the brittle behavior is inconsistent with the ductile or plastic deformation mechanism. Schematic illustrations of brittle and ductile machining mechanisms are shown in Figure 2.7 While the material removal was accurately described as ductile by Bifano [57], no corresponding satisfactory process mechanism was proposed at the time that would explain the observed ductile behavior.

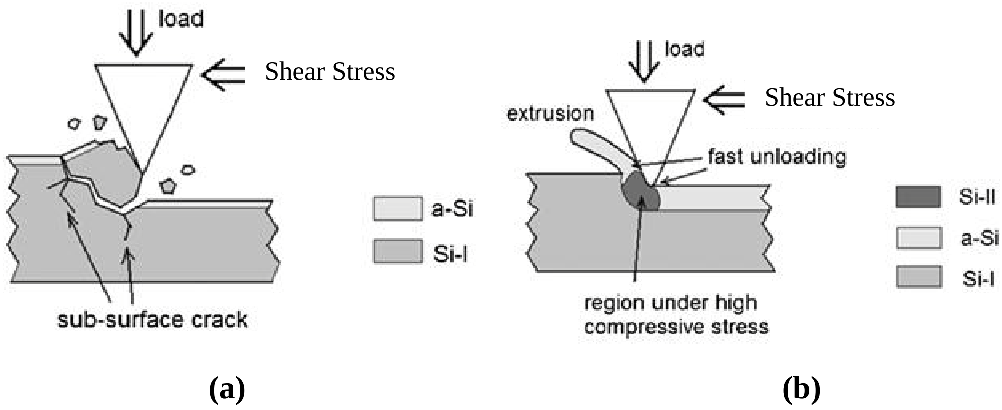

Figure 2.7. Schematic illustrations of

(*a*) brittle and

(*b*) ductile machining mechanisms.

The concept of 'ductile machining' did not originally include the connection between the high pressure phase transformation and the cutting-plastic deformation mechanism. Previously, the practical understanding about the ductile regime machining process was accepted as occurring due to a size effect [68] or slip orientation factor [69]. However, the origin of the ductility of normally brittle materials was eventually answered [26] and the role of the HPPT relative to the materials' ductile response was thus scientifically and empirically established.

HPPT of nominally brittle materials have been observed since around 1940s [56]. But it was not until the mid 1990s that researchers adopted the HPPT as one of the material deformation mechanisms that account for the ductile response of hard and brittle materials, e.g. semiconductors and ceramics [26]. Since then, research efforts have been directed towards gaining a better understanding of the mechanisms underlying ductile-regime machining, especially relative to the HPPT [59]. The establishment of the HPPT as the main deformation mechanism for the ductile machining of brittle materials provides answers to many fundamental questions. These HPPT can occur at room temperature conditions where dislocation mobility in these hard brittle materials is practically non-existent [70]. The traditional dislocation based plastic deformation mechanism is practically inoperative at room temperature in covalent semiconductors and ceramics except for very low strain rates [71]. And our assumption is that these dislocations are responsible for the ductile nature of the high pressure metallic phase.

Single-point diamond turning (SPDT) was originally developed to machine nonferrous metal optical parts, which have high surface finish quality requirements. The technique has been adapted to machine brittle materials such as semiconductors and ceramics. This is possible by employing diamond as the cutting tool, which is harder that the workpiece material. SPDT is a very promising machining technology for hard brittle materials. There are other methods that don't consider or require the HPPT as the central plastic or ductile deformation mechanism, such as laser-assisted machining (LAM). This process relies on thermally softening of the grain boundaries in polycrystalline materials, such as sintered ceramics [72], to achieve a ductile response.

Although SiC is naturally very brittle, micro/nanomachining this material is possible if sufficient compressive stress is generated to cause a ductile mode behavior, in which the material is removed by plastic deformation instead of brittle fracture. This micro-scale phenomenon is also related to the High Pressure Phase Transformation (HPPT) or direct amorphization of the material [5, 7]. Figure 2.8 shows a graphical representation of the highly stressed (hydrostatic and shear) zone that results in ductile regime machining.

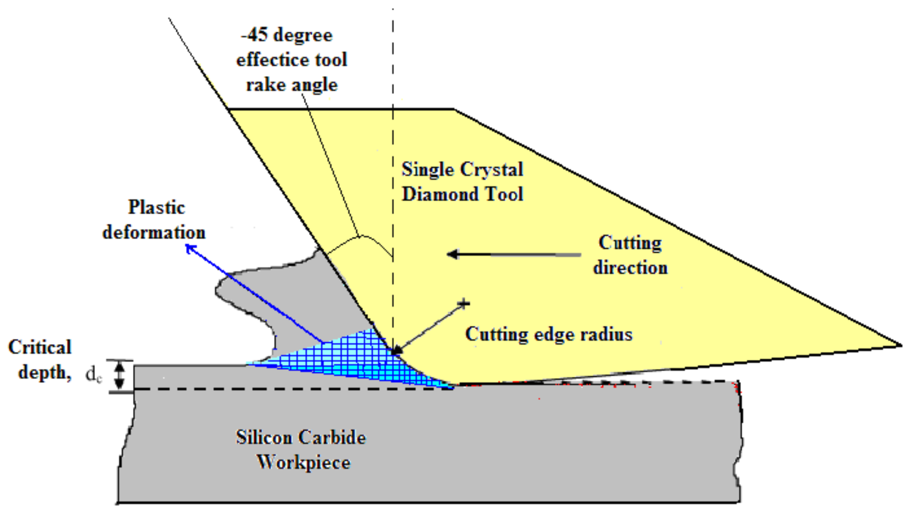

Figure 2.8. A ductile machining model of brittle materials.

Figure 2.8 represents a ductile cutting model showing the high compressive stress and plastically deformed HPPT material behavior in brittle materials. A -45^{o} rake angle tool is demonstrated in the above schematic as a negative rake angle tool yields a higher compressive stresses at the tool-workpiece interface [5, 7].

2.5.2. Ductile to Brittle Transition (DBT) in Brittle Materials

In machining of crystalline materials, crystal size and defects like dislocations and cracks affect mechanical behavior of the material [56]. Indentations in small crystals having no defects, generates dislocations prior to brittle fracture. The DBT concept has been applied to indenting, scratching and machining processes. For indentation, the DBT is the maximum penetration depth, below which, only plastic deformation is observed. In scratching, the DBT is the critical depth of the scratch groove, below which, no brittle fracture occurs in the process. In machining, the DBT is generally associated with the uncut chip thickness, which varies along the nose radius for such a tool (or critical chip thickness), and is a function of feed (crossfeed or feed per rev or per sec) and depth of cut (infeed).

There is a critical depth of cut (DoC) used for identifying the transition point from ductile to brittle behavior during the deformation process, i.e., machining, scratching and indenting [73]. For a 3-D machining configuration (such as turning), typically a critical chip thickness is used to define the transition point for the DBT [25]. For example, usually for machining, a feed or uncut chip thickness of less than 200 nm is used to establish the DBT depth in silicon [74]. Ductile machining is normally achieved when the DoC (or similarly the feed or uncut chip thickness) is less than the critical DoC. Above this threshold, i.e. at larger depths, brittle behavior generally occurs and dominates the process [57].

The Blake and Scattergood ductile regime machining model (as shown in Figure 2.9) was used to predict the required thrust force for a desired depth of cut [24]. In this model it is assumed that the undesirable fracture damage (which extends below the final cut surface) will originate at the critical chip thickness (t_c), and will propagate to a depth, y_c. This assumption is consistent with the energy balance theory between the strain energy and surface energy [61].

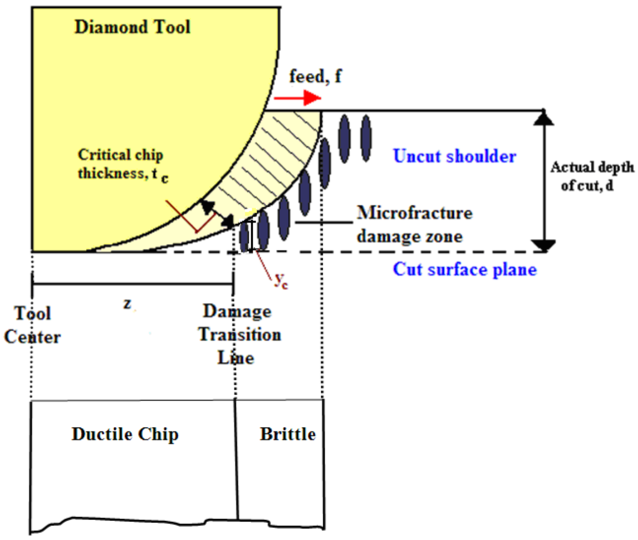

Figure 2.9. Model for ductile regime machining.

The ductile material removal mechanism in nominally brittle materials is still assumed to occur via plastic deformation, and the resultant material removal process does not cause any significant surface or subsurface cracks. A small DoC is favorable because a large DoC would inevitably cause brittle fracture [75]. However, a small DoC results in longer machining times, which may lower the overall productivity of the manufacturing process.

Brittle materials are prone to fracture, which has remained a significant problem in precision machining of such materials [76]. Understanding the interaction between the tool and the work piece is critical to know how to adjust the machining parameters to produce desirable results, such as in ductile regime machining [31]. There are many machining parameters that must be considered in determining the onset of brittle fracture, i.e., the critical DoC, rake angle, cutting edge radius, etc [77]. The shape of the cutting tool, cutting speeds, feed rates and the mechanical properties of the work piece are among the most significant parameters [78]. These parameters, together with the appropriate DoC have to be carefully chosen to ensure a ductile response during the deformation process in order to generate a crack free and smooth surface.

2.6. Lasers in Manufacturing

Laser is an acronym for Light Amplification by Stimulated Emission of Radiation (LASER). Theodore Harold Maiman officially invented the world's first working laser, known as the "ruby laser", at Hughes Research Laboratories in the USA in 1960. His study represented a major breakthrough in the field of applied physics [79]. Ruby crystal is composed of aluminum oxide, where some of the aluminum atoms have been replaced with chromium atoms. Chromium gives the ruby its vibrant red color. In a ruby laser, a ruby crystal is formed into a cylinder. A fully reflecting mirror is placed on one end and a partially reflecting mirror on the other. A high-intensity lamp is spiraled around the ruby cylinder to provide a flash of white light that triggers the laser action. Structure of the world’s first laser (Ruby Laser) is shown in Figures 2.10 and 2.11 respectively.

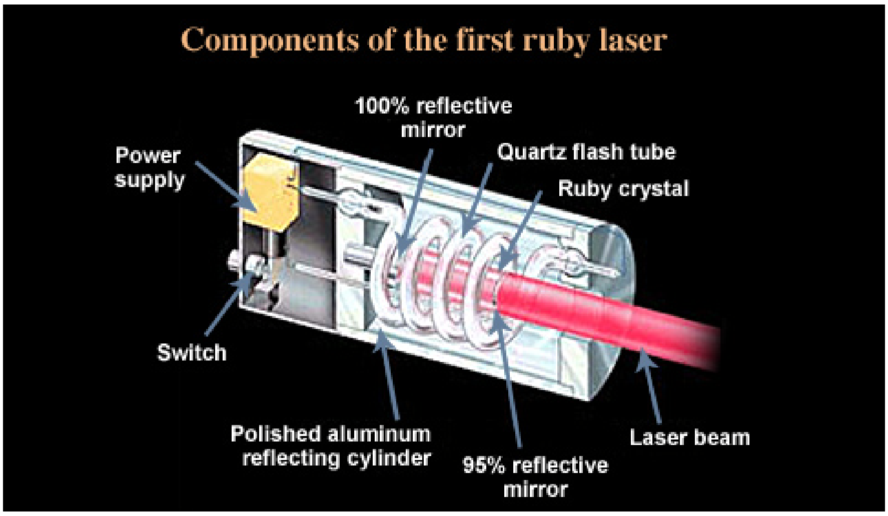

Figure 2.10. Components of the first ruby laser.

(Photo Credits: Lawrence Livermore National Security, LLC, and the U.S. Department of Energy).

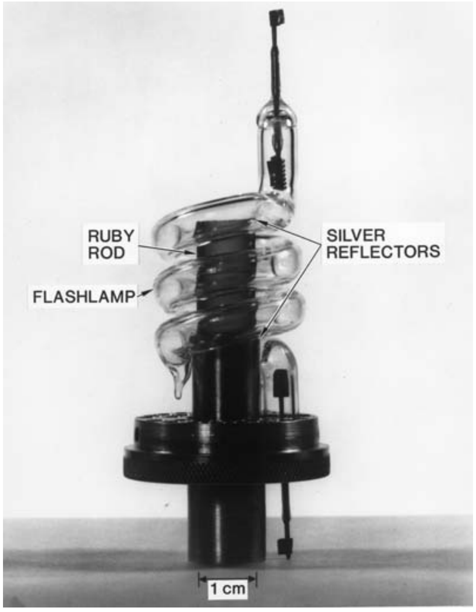

Figure 2.11. Structure of the first ruby laser by Theodore Maiman.
(Image courtesy of HRL Laboratories, LLC).

Lasers are essentially a coherent, convergent, and monochromatic beam of electromagnetic radiation with wavelength ranging from ultraviolet to infrared. Lasers have now found applications in almost every field of engineering, medicine, electronics, etc., where one or more properties of the laser radiation are important [80-83].

Lasers are finding continuously increasing utilization in the manufacturing processes. The applications of lasers have been demonstrated in many casting, forming, joining, and machining processes. Some of these processes are still in the stage of development. Currently, there are several laser-based manufacturing processes which are commonly used. These are;

- laser casting,
- laser forming/shaping,
- laser joining, and
- laser machining processes

which are commonly used for specific applications.

Lasers provide highly concentrated energy through a small diameter beam. The industrial application of lasers has been exclusively focused on machining of metallic materials since the early 1970s [76]. High power lasers (kW), such as CO_2 and Nd:YAG lasers, are used as non-contact cutting tools, locally melting or ablating the work piece with intensive heat energy. The materials are thermally softened, melted or sometimes evaporated (ablated) under the intense laser energy [76]. From the mid-1990s, lasers started being used for machining of non-metallic and hard materials, such as semiconductors and advanced ceramics.

2.6.1. Laser Materials Interactions

Understanding the capabilities and limitations of laser machining requires the knowledge of physical processes occurring during the laser beam interactions with materials. When the electromagnetic radiation is incident on the surface of a material, various phenomena that occur include reflection, refraction, absorption, scattering, and transmission (Figure 2.12).

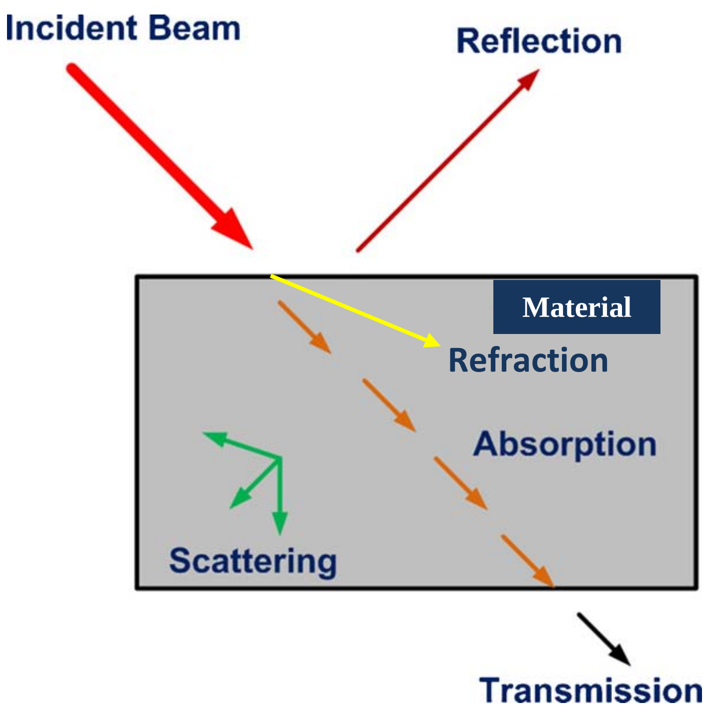

Figure 2.12. Possible interactions of laser light with material.

One of the most desirable and important phenomena in the laser processing of materials and influencing the effects of laser–material interactions is the absorption of the radiation. Absorption of radiation in the materials results in various effects such as heating, melting, vaporization, plasma formation, etc., which forms the basis of several laser materials-processing techniques [80]. The extent of these effects primarily depends on the characteristic of electromagnetic radiation and the thermo-physical properties of the material. The laser parameters include intensity, wavelength, spatial and temporal coherence, angle of incidence, polarization, illumination time, etc., whereas the materials parameters include absorptivity, thermal conductivity, specific heat, density, latent heats, etc. The interaction of laser with material is a complex interdisciplinary subject and requires knowledge from several branches of physics.

The absorption of laser radiation in the material is generally expressed in terms of the Beer-Lambert law [80]:

$$I(z) = I_0 e^{-\mu z} \tag{2.5}$$

where I_0 is the incident intensity, $I(z)$ is the intensity at depth z, and *m(μ)* is the absorption coefficient. Thus, the intensity of the laser radiation gets attenuated inside the material. The length over which the significant attenuation of laser radiation takes place is often referred to as the attenuation length and is given by the reciprocal of the absorption coefficient [84]:

$$L = \frac{1}{\mu}. \tag{2.6}$$

For a strongly absorbing material, the absorption coefficients are in the range of 10^5–10^6 cm^{-1} such that the attenuation lengths are in the range 10^{-5}–10^{-6} cm (0.1-1 µm or 100-1000 nm) [85].

Absorptivity of the material for laser radiation can be defined as the fraction of incident radiation that is absorbed at normal incidence. For opaque materials, the absorptivity (A) can be expressed as [85]:

$$A = 1 - R \tag{2.7}$$

where R is the reflectivity of the material. The reflectivity and the absorptivity of the material can be calculated from the measurements of optical constants or the complex refractive index. The complex refractive index (n_c) is defined as:

$$n_c = n - ik \tag{2.8}$$

where n and k are the refractive index and extinction coefficient, respectively. These parameters are strong functions of wavelength and temperature. The reflectivity at normal incidence is then defined as:

$$R = \frac{(n-1)^2 + k^2}{(n+1)^2 + k^2} \tag{2.9}$$

Since parameters n and k are strong functions of wavelength and temperature, the reflectivity (and hence the absorptivity) of the material is greatly influenced by the wavelength and temperature [85]. Other parameters which influence the absorptivity of the material include angle of incidence of the radiation and surface condition of the material. These concepts have been extensively utilized to improve the coupling of the laser radiation to the reflective material by applying antireflective surface coatings and laser irradiating the material at suitable angle of incidence [80, 86].

Depending on the magnitude of the temperature rise, there are various physical effects in the material that include heating, melting, and vaporization of the material. Furthermore, the ionization of vapor during laser irradiation may lead to generation of plasma. In addition to the thermal effects, the laser–material interactions may be associated with photochemical processes such as photoablation of the material. All of these effects of laser–material interactions are schematically presented in Figure 2.13. All of the effects shown in the figure play important roles during laser materials processing. There exist distinct combinations of laser intensities and interaction times where specific effect of laser–material interaction dominates [87, 88].

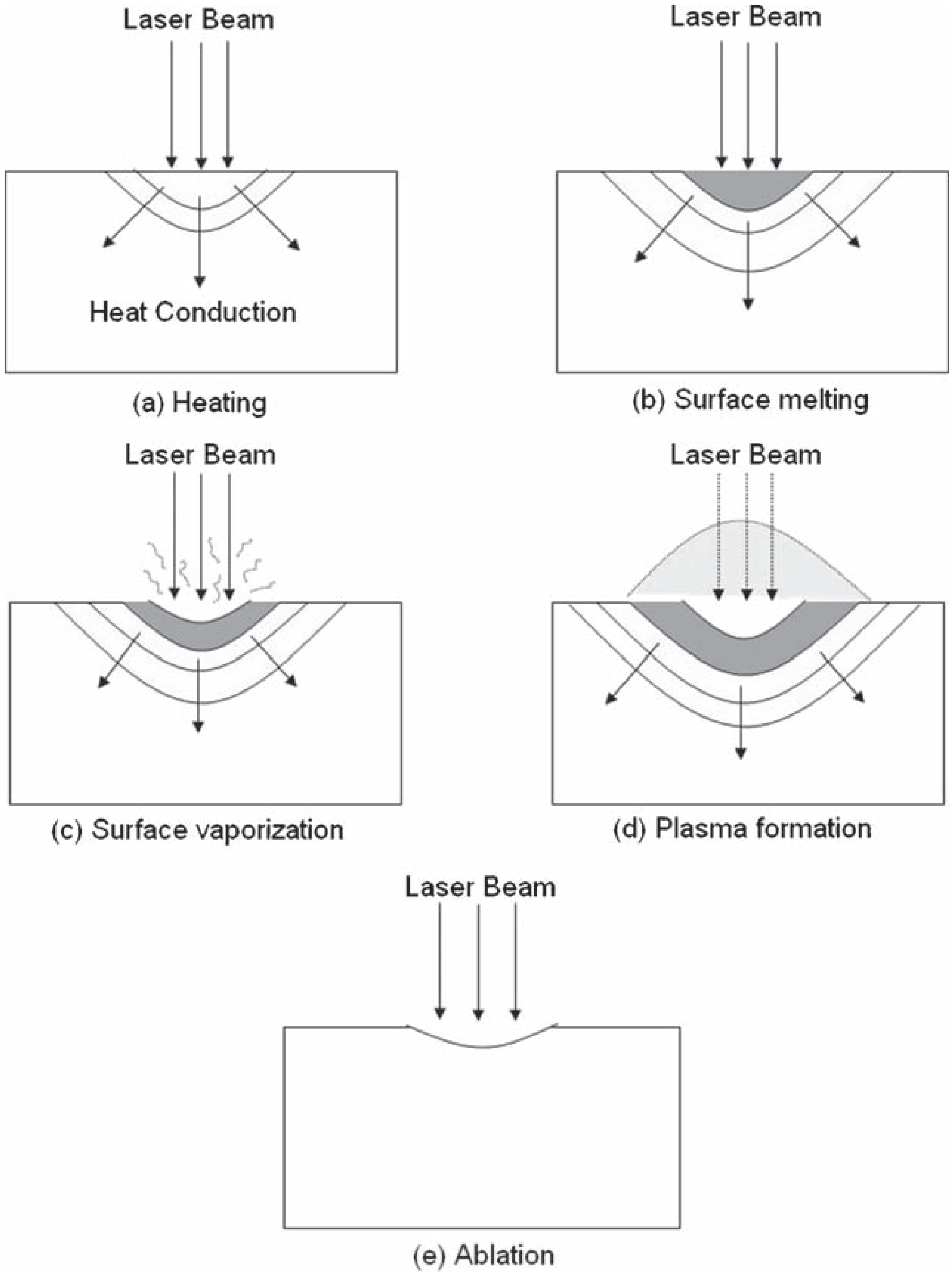

Figure 2.13. Various effects of laser–material interaction:

(a) heating,

(b) surface melting,

(c) surface vaporization,

(d) plasma formation, and

(e) ablation [87, 88].

2.6.2. Laser Machining

Lasers can replace mechanical material removal methods in several engineering applications because of their following salient features [89]:

(i) Non-contact process: Energy transfer from the laser to the work piece material through irradiation eliminates cutting forces, tool wear and machine vibration. Furthermore, the material removal rate is not affected by the maximum tool force, tool chatter or built-up edge formation, but can be controlled by varying the laser processing parameters such as input energy and processing speed.

(ii) Thermal process: The efficiency of laser machining depends on the thermal and, to some extent on the optical properties of the material. This makes hard or brittle materials such as structural ceramics with low thermal diffusivity and conductivity suitable for machining.

(iii) Flexible process: In combination with a multi-axis positioning system or robot, lasers can be used for drilling, cutting, grooving, welding and heat treating on the same machine without any necessity to transport the parts for processing them with specialized machines. In-process monitoring during the laser machining process can allow key parameters to be measured and a high level of reproducibility can be attained [90]. Relative economic comparison of laser machining with other machining processes is made in Table 2.4 [91, 92].

Table 2.4. Various nontraditional machining processes [91, 92].

Machining process	Parameter influencing economy				
	Capital investment	Toolings/ fixtures	Power requirements	Removal efficiency	Tool wear
Conventional machining (CM)	Low	Low	Low	Very low	Low
Ultrasonic machining (USM)	Low	Low	Low	High	Medium
Abrasive jet machining (AJM)	Very low	Low	Low	High	Low
Electrochemical machining (ECM)	Very high	Medium	Medium	Low	Very low
Chemical machining (CHM)	Medium	Low	High	Medium	Very low
Electric discharge machining (EDM)	Medium	High	Low	High	High
Plasma arc machining (PAM)	Very low	Low	Very low	Very low	Very low
Laser beam machining (LBM)	Medium	Low	Very low	Very high	Very low

Different types of lasers are used for machining of structural ceramics with each type of laser having its own wavelength of absorption and machining applications. The different types of lasers can be operated in either the continuous wave, CW or the pulsed mode, PM (nano, pico and femto second lasers). In CW lasers, continuous pumping of the laser emits incessant light, while in a pulsed laser, there is a laser power-off period between two successive pulses [93]. Pulsed lasers are preferred for machining ceramics (laser ablation) as the processing parameters can be more effectively controlled compared to continuous wave mode [94].

By controlling the motion and geometry of the workpiece, and laser beam delivery system, lasers can be used for a variety of one-, two-, and three dimensional machining applications (see Figure 2.14) [89].

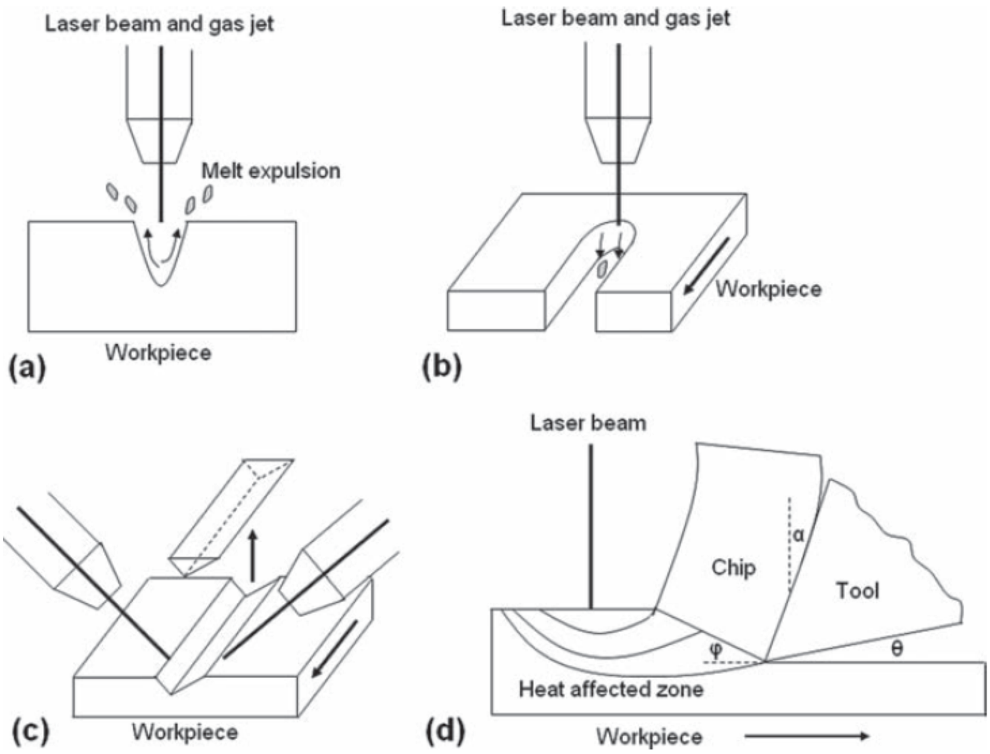

Figure 2.14. Basic laser machining processes:

(a) laser drilling (one-dimensional machining),

(b) laser cutting (two-dimensional machining),

(c) laser milling (three-dimensional machining), and

(d) laser-assisted machining (LAM) [89].

Schematics of the basic laser machining processes are presented in Figure 2.15. The laser beam is considered as a one-dimensional line source with line thickness given by the diameter for circular and the major axis for elliptical beam cross-sections. Laser drilling (one-dimensional) (Figure 2.15 a) can be achieved by keeping the ceramic workpiece and the laser beam stationary. Motion of the laser beam or the ceramic workpiece in only one direction leads to laser cutting (two-dimensional machining) (Figure 2.15 b). Motion of one or more laser beams or the workpiece in more than one direction leads to three-dimensional machining and complex geometries can be machined (Figure 2.15 c) [88].

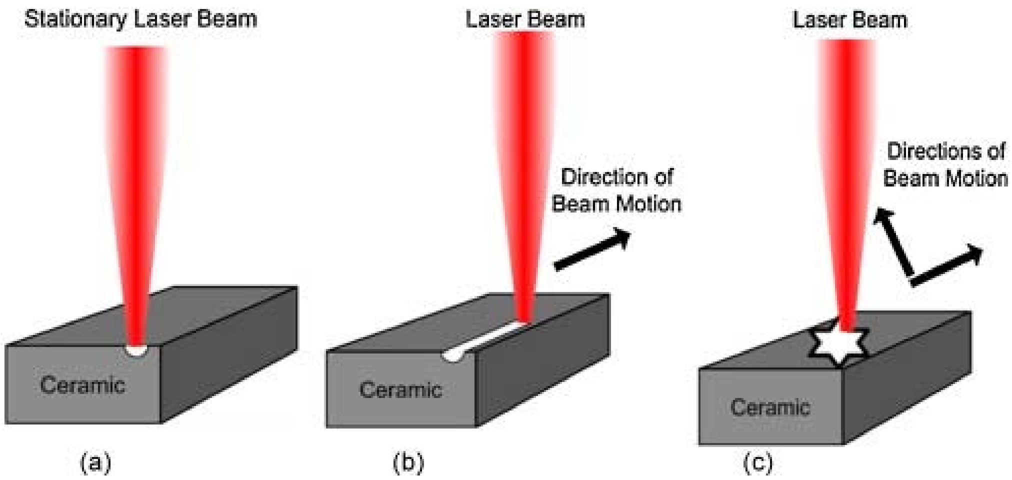

Figure 2.15. Schematic of basic laser machining processes
(a) laser drilling (one-dimensional machining),
(b) laser cutting (two-dimensional machining),
(c) engraving a star by laser beam (three-dimensional machining).

Lasers are now extensively used in the industry for drilling, cutting, and shaping of materials. The laser machining operations are efficient and economical in a number of industrial applications where large production rates are desired.

Laser drilling is particularly useful for high-aspect ratio micro-drilling applications where conventional mechanical drilling is not applicable or less efficient. Laser drilling can be used with a variety of material systems ranging from, metal, polymers, ceramics, to composites. There may be certain limitations on the diameter and the depth of the laser-drilled holes, i.e., aspect ratio. However, with the careful design of the laser drilling systems (such as trepanning and percussion drilling), big and wide holes may be produced. In addition, the laser-drilled holes may be associated with certain undesirable geometric and metallurgical defects (such as taper, recast layer, etc.). Again, careful design of laser parameters (pulse shapes, beam profiles, laser power, etc.) and other process parameters (application of sacrificial coatings, assist gases, nozzle designs, etc.) may minimize or eliminate these laser drilling defects. Thus, lasers can be used for drilling high-aspect ratio holes in a variety of materials. The overall drilling economics and the desired quality levels must be considered before selecting the laser drilling for a given application [88, 89]. A detailed schematic of the laser drilling process is shown in Figure 2.16.

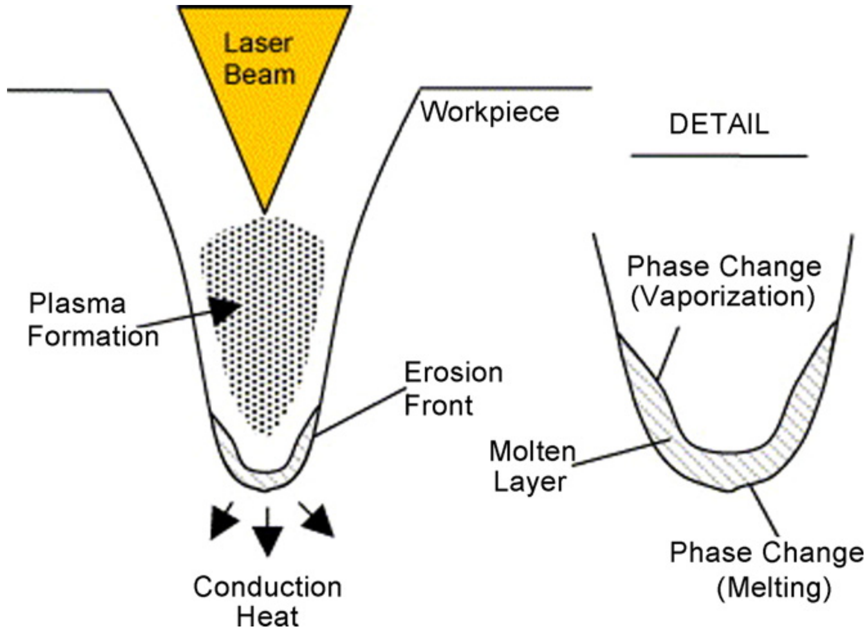

Figure 2.16. Laser drilling process schematic [89].

Laser cutting is an established technology for machining difficult-to-machine materials such as advanced ceramics. Laser cutting can be used in a number of ways to remove the materials (vaporization, melt expulsion, chemical reactions, etc.), thus, these are extending the limits of machining capabilities. Both pulsed and continuous lasers have been used for laser cutting, which offers significant advantages such as cutting of complex geometries, faster processing speeds, cutting of wide range of materials, clean cuts, etc. Laser cutting may also be associated with certain defects such as striations (periodic pattern on the cut edge), dross, heat-affected zones, etc. Hence, selection of the laser cutting process for a given application primarily involves careful consideration of laser cutting capabilities, quality considerations, and overall economics of manufacturing [88, 89].

Ceramics are widely used in a wide range of applications such as structural, automotive, and electronic applications due to their unique combination of properties such as high hardness, high thermal strength, chemical inertness, attractive high temperature abrasion resistance, and low density. Despite these remarkable properties, the actual utilization of advanced ceramics has been quite limited mainly because of high cost of the machining and inability to achieve the dimensional control and workpiece quality required for these applications. The production methods for ceramics like compaction and sintering are still not developed enough to produce dimensional accuracy or surface roughness of the finished part, in addition to the processing defects like material shrinkage and distortion. Conventional machining includes most widely used grinding or diamond machining which are very expensive and time consuming. Machining cost for semiconductors and ceramics by conventional machining accounts for 60–90% of the total cost of the final product [95]. For such applications laser machining offers economical solutions. Lasers are well suited for processing of most of the semiconductor and ceramic materials due to very high absorptivities to laser radiations. Lasers are now extensively used for machining of semiconductor ceramic materials.

2.7. Present State of Knowledge in the Field

Semiconductor and ceramic materials, such as silicon (Si), silicon carbide (SiC) and silicon nitride (Si_3N_4), are traditionally expensive to manufacture in to products due to their inherent material properties, such as their high hardness and strength. These same material properties also provide much of their intrinsic usefulness; i.e. the very properties that make them desirable for mechanical (and to a lesser extent electrical and optical) components also adversely affect their manufacturability. It is quite well documented, and generally understood by researchers working in this field, that the ductile regime machining of these nominally hard and brittle semiconductors and ceramics (at room temperature) is achieved via the formation of (metallic) high pressure phases during mechanical contact and deformation [7, 26, 96-99]. This is particularly true at room temperature conditions. At elevated temperatures, generally above the thermal softening point (typically in the range of 600 to 1000 ^{o}C), other process mechanisms can be thermally activated [100]. For semiconductors, thermal activation of dislocations becomes possible at these elevated temperatures, which may lead to microscopic level plastic deformation [101, 102]. For ceramics, particularly those with binder phases (such as Si_3N_4) thermal softening of the binder phase can lead to micro-macroscopic plastic deformation of the bulk material [22, 103-104]. For the latter case, it is not the individual ceramic grains (Si_3N_4) that plastically deform in a ductile manner, but rather it's the binder material along the grain boundaries that thermally softens and accommodates severe plastic deformation, such as occurs in macro-scale LAM.

2.7.1. Laser Micro Machining (Laser Ablative) of Semiconductor and Ceramic Materials

Laser ablative-machining, as practiced in micro-machining processes, is a complementary technology to this research study. Laser ablative machining relies on heating a small volume of material (micro scale machining) to sufficiently high temperatures to cause the material to vaporize and form plasma, which is then ejected from the surface due to an evaporative process. These processes, which require very high temperatures to process semiconductors and ceramics, can achieve moderate material remover rates with increasing laser size and capacity, but lack precision form accuracy due to the laser beam itself not being a "precise" shape. Micrometer scale features are produced commercially (Laser Light, Noble Inc., Reesonetics, LMS, etc.) with surface finish values under a micrometer obtainable [105]. However, form accuracy and surface roughness in the nanotechnology regime (10-100 nm) are uncommon.

Lasers are powerful tools for micromachining applications. A focused laser beam can easily be concentrated onto a target of a few microns in diameter (or a laser-illuminated mask can be imaged onto the work piece with a high-resolution objective). The laser material interaction in this target area will be controlled by parameters such as wavelength, pulse energy, and pulse duration, which determine peak power density, etc. Certain sets of parameters can cause thermal effects for marking, cutting, drilling, annealing, hardening, etc [106].

Laser micromachining is extensively used for manufacturing of microparts with micron and submicron resolution in a wide range of applications such as biotechnological, microelectronics, telecommunication, MEMS, and medical applications [107]. A wide range of materials such as metals, ceramics, and polymers have been successfully micromachined (see Figure 2.17 and 2.18).

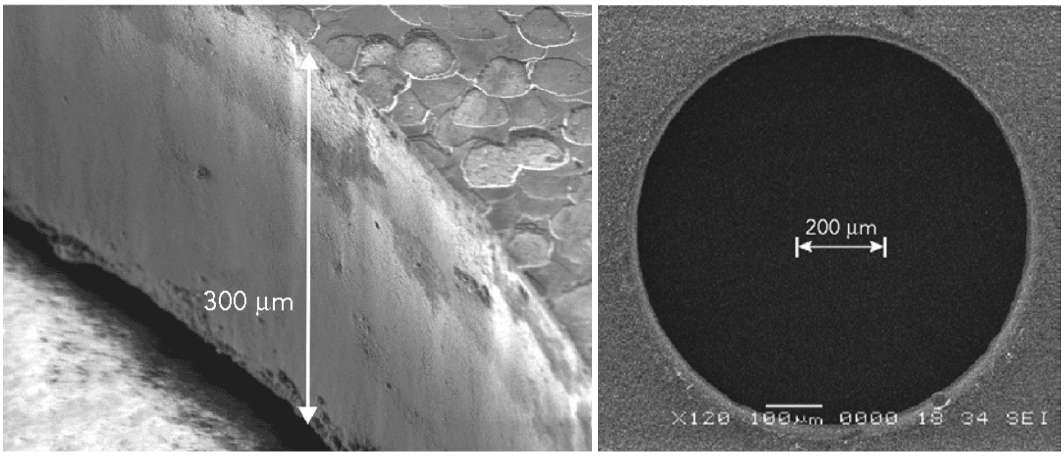

Figure 2.17. Cutting holes in 300 µm thick Si wafer via using a picosecond laser system [106].

SiC as a structural ceramic has been widely machined by lasers for different purposes. Using a pulsed Nd:YAG laser (1064 nm wavelength laser) at an input energy of 6 J, pulse duration of 0.5 ms, and repetition rate of 50 Hz, a through cavity was machined in a 2 mm thick SiC plate in approximately 25 pulses while it took about 125 pulses to machine through the entire thickness of a 3 mm thick plate (Figure 2.18) [108].

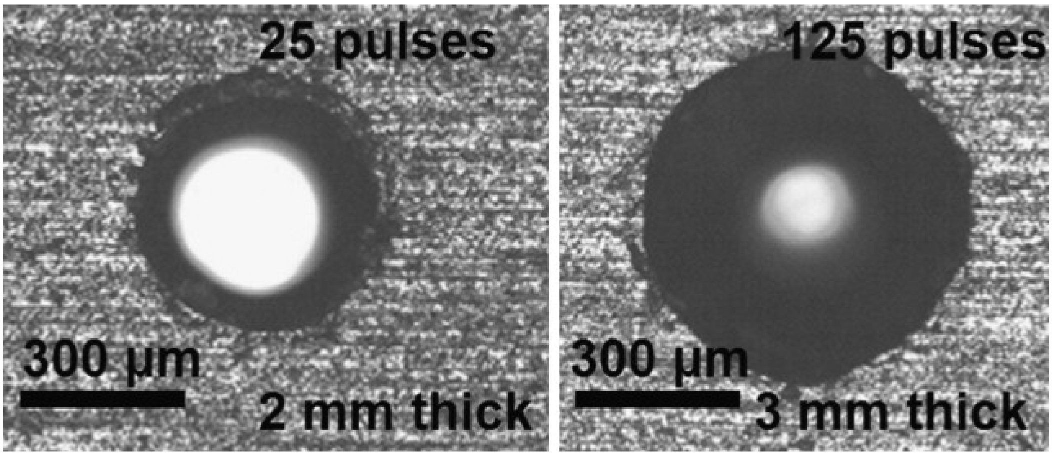

Figure 2.18. Laser micro machining in 2 and 3 mm thick SiC plates [108].

A hole drilled in SiC with associated microstructural features is presented in Figure 2.19, respectively. The drilling in SiC was carried out using a pulsed CO_2 laser (λ = 10.6_m) with a pulse duration of 2 ms, a power of 0.5kW and the lens had a focal length of 31.8 mm [109].

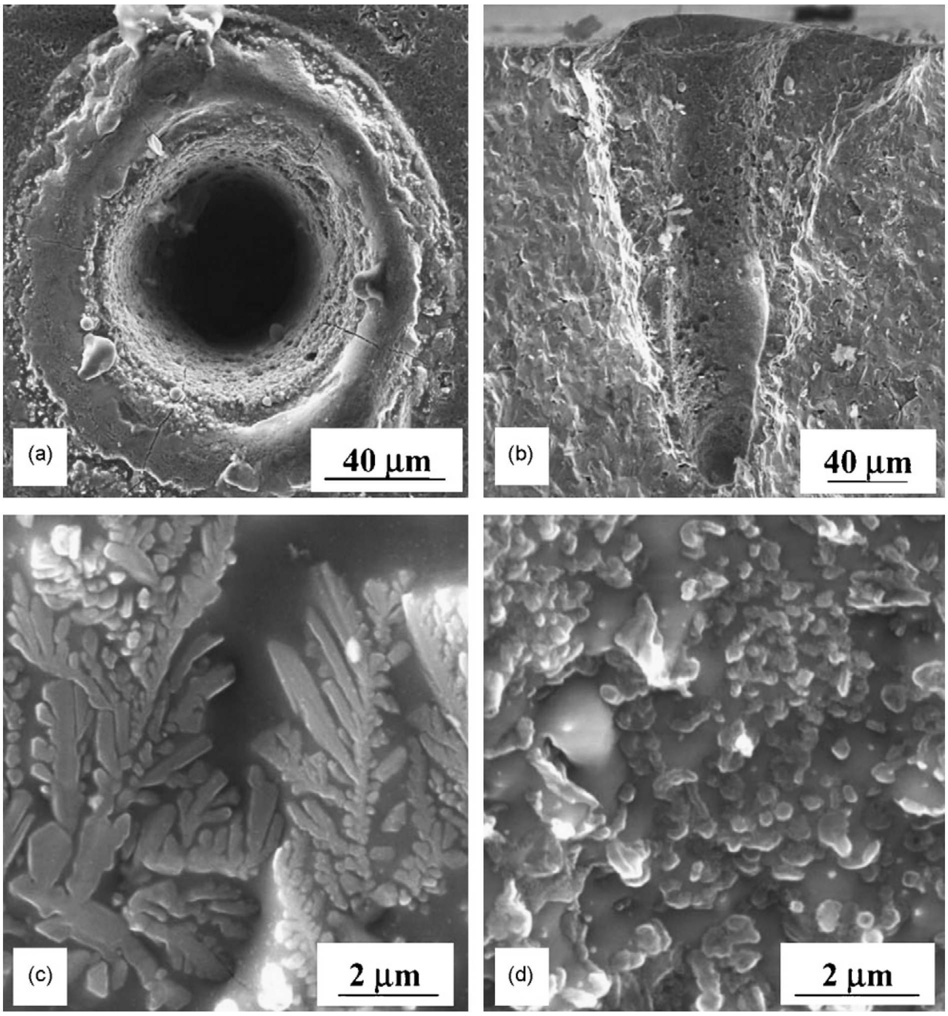

Figure 2.19. Microstructural features of hole obtained in SiC

(a) hole entry

(b) hole section

(c) silicate-like dendrite crystals obtained on debris area

(d) hole inside walls [109].

There is an increasing demand for producing parts with micro and meso scale features in the field of semi-conductors, biomedical devices and optics [110]. In light of this demand, several techniques such as mechanical micromachining (microgrooving, micro-milling), focused ion-beam micromachining, laser micromachining are being used in microfabrication. Laser micromachining is a comparatively new technique and provides improved flexibility in dimensional design of microproducts [87].

However, no detailed studies on the physics behind laser micromachining of structural ceramics have been found in open literature. The common problems associated with conventional micromachining are tool wear and force-induced damage on ceramic components [111]. These problems can be adequately addressed by using thermal softening by a laser heat source during micro-machining. Thus, laser micro-machining of structural ceramics is still a gray area and has immense potential for research and applications [88].

2.7.2. Laser Assisted Machining (LAM) of Semiconductor and Ceramic Materials

The physical phenomena taking place during the laser assisted machining (LAM) of materials is different from laser micro machining. In traditional LAM processes, laser radiation is used as a heating tool to soften the uncut work piece material, i.e. prior to the deformation and removal of the material without melting or sublimation. The type (wavelength) and power of the laser source used for LAM depends on the desired material removal rate and the absorption and penetration depth into the work piece of the laser beam. In LAM methods, the lasers used are CO_2 lasers. In this traditional LAM processes, the work piece surface is first heated with a laser to thermally soften the material and then a cutting tool is used for the material removal [22, 72]. This is shown schematically in Figure 2.20. Due to excessive laser heating involved in this process, the laser power has to be very high (kW) in order to thermally soften the material before the tool moves over the heated area.

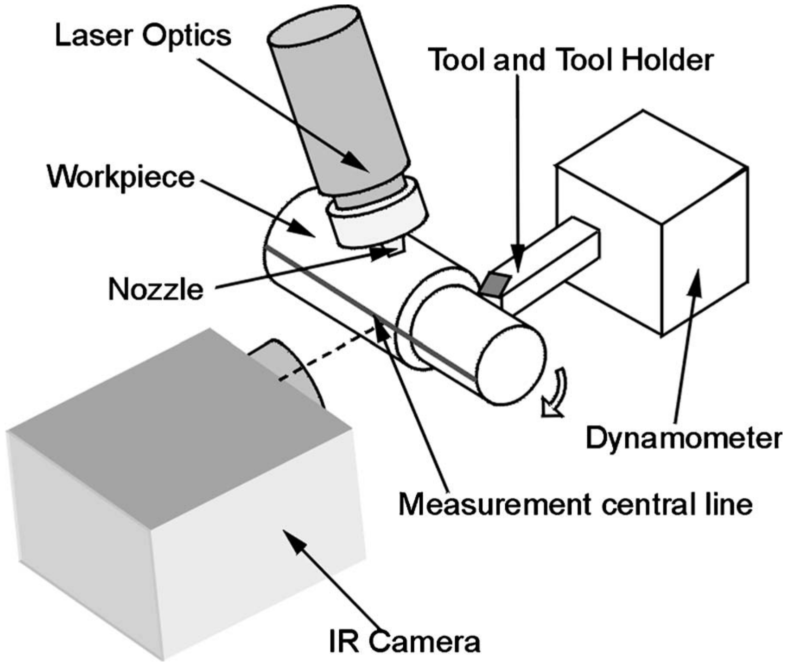

Figure 2.20. Schematic setup for the conventional LAM process [22, 72].

The typical laser assisted machining (LAM) system [22, 72, 112-115] uses an external laser source to preheat the work piece material prior to material removal (often times, Si_3N_4 is the specific material of interest; whereas this study is focused on Si and SiC, but the work is applicable to Si_3N_4 also). In other words, the work piece is heated (actually the binder phase of the ceramic is the active medium) and then the machining takes place on this heated material. Again it is not the individual ceramic grains that plastically deform in a ductile manner, but rather it's the binder material along the grain boundaries that thermally softens and accommodates severe plastic deformation

Fundamental and development work have been progressing for a number of years at Purdue University (see Figure 2.21) and Fraunhofer Institute for machining ceramic materials. Related work is currently in progress at Rutgers, Wisconsin-Madison, and Georgia Tech.

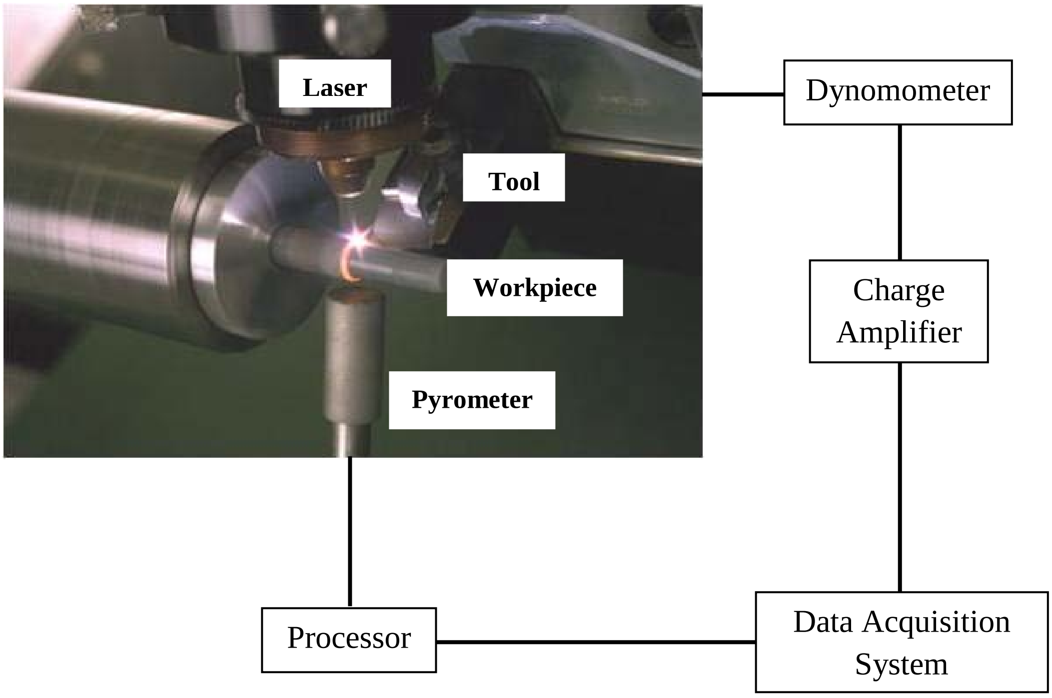

Figure 2.21. Experimental system for Laser Assisted Machining (LAM) of Si_3N_4 at Purdue University [115].

This technique has been successfully used for machining silicon nitride and the corresponding work piece temperature, tool wear and surface integrity have been measured [115-120].

Magnesia-partially-stabilized zirconia (MgPSZ) was machined with a polycrystalline cubic boron nitride (CBN) tool and it was found that the tool life increased with material removal temperatures [121]. LAM effectively reduced the cutting force and improved the surface finish of the finished products made from Al_2O_3 [122]. In LAM, after the laser is used to change the ceramic deformation (again, it's the binder, not the ceramic, being affected) behavior from brittle to ductile, material removal takes place with a conventional cutting tool. Unlike LAM, in laser machining (LM), actual material removal takes place by the laser beam.

The LAM process is mainly used for higher material removal rates that do not require high accuracies or precision surface finishes. The process configuration usually consist of a high power (100s W to kW) laser and a conventional machine tool (such as a CNC lathe or milling machine) using CBN tooling. In this configuration, the laser system is an auxiliary component to the standard CNC machine tool. This process is differentiated from the laser micro machining system described above primarily by the temperature of the work piece. For LAM processes, such as practiced on ceramics, the work piece may be heated to around 1000 ^{o}C. This temperature level, in the case of ceramics, is sufficient to thermally soften the binder phase material (sintering agent), while mostly unaffecting the ceramic grains; only the grain boundaries are "softened".

Conventional machine tools and tooling are employed and therefore the final form accuracy and surface finish are limited by the precision of these components. The dimensional accuracy is also partially limited due to the thermal expansion, primarily of the work piece, as a result of heating a volume of material to these high temperatures. Also, the ultimate surface finish is restricted by the grain size of the material. In the case of ceramic materials, the individual ceramic grains themselves do not deform plastically but rather act as rigid bodies immersed in the softer binder phase.

2.7.3. Micro-Laser Assisted Machining (μ-LAM) of Semiconductor and Ceramic Materials

The infrared (IR) laser beam is coupled from the laser source (diode laser) to a fiber optic cable and ferrule, which is attached to the diamond cutting tool. The diamond cutting tool exerts an extreme pressure (GPa) on the material (semiconductor or ceramic) and generates a high pressure phase (HPP), via the high pressure phase transformation (HPPT). The unique characteristic of this technology is that the work piece material, i.e. the material to be machined or cut, is generally a covalent or ionic material, whereas the HPPT material is metallic. The IR laser prefentially heats the HPPT material, as it is opaque to the IR radiation, whereas the IR beam passes through the diamond tool and the untransformed material nearly unaffected. This novel system of utilizing the transparent properties (of diamond and semiconductors) and the opaqueness of metals to IR radiation provide the direct benefit of heating and thermal softening the HPPT material, while leaving the diamond and untransformed work piece material virtually unaffected. This would be similar to developing a surgical procedure (or radiation method) which could pass through skin or other protective coating and interact with sub surface material, while unaffecting the surrounding material. A schematic cross section of the system operation is shown in Figure 2.22.

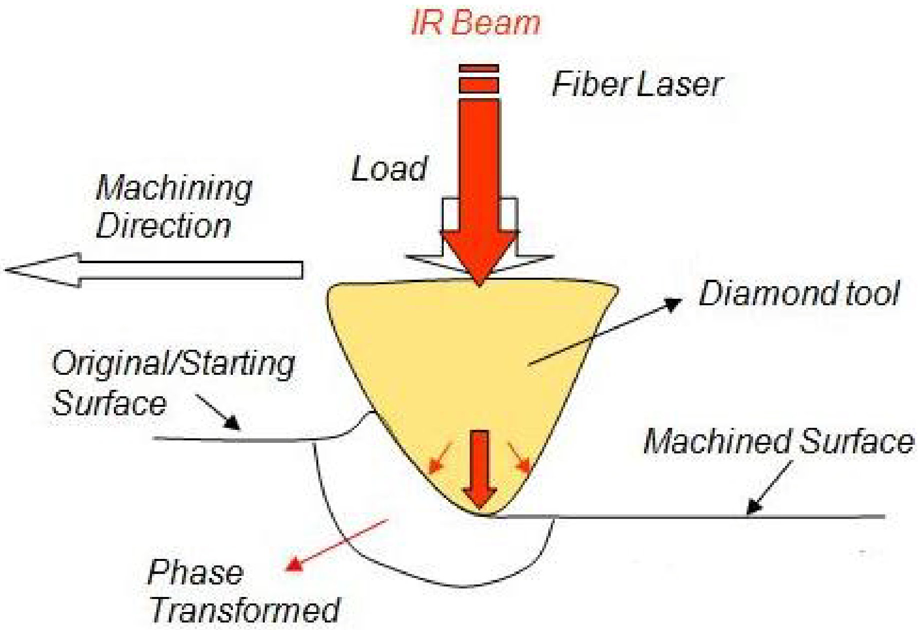

Figure 2.22. A schematic cross section of the μ-LAM system design (for this study).

The key design parameter for the μ-LAM system is that the tool (single crystal diamond) and the work piece materials (semiconductor or ceramic) are transparent to the laser wavelength, and the transformed material is opaque to the laser radiation. The necessity for the transparency of the tool to the laser is obvious based upon the design of the μ-LAM system. Equally important is the transparency of the work piece material to the laser, such that the bulk material does not absorb the laser beam, which would lead to unnecessary heating of the substrate and possibly result in thermal induced sub surface damage. The opaqueness of the transformed material to the laser wavelength provides for the preferential heating and resultant thermal softening.

The μ-LAM system is ideally suited for demanding applications in the field of precision engineering and precision manufacturing due to its compatibility with SPDT. This novel processing method can be applied to ceramics (silicon carbide (SiC) and silicon nitride (Si_3N_4)), which are particularly difficult to process due to their extreme mechanical properties. Semiconductor materials, such as silicon (Si) and germanium (Ge), can also benefit from exploiting this technology. This new processing technique can potentially lead to entirely new products (product realization) for the next generation devices, produced from these difficult to machine materials, in mechanical, microelectronic and optical systems.

2.7.4. Comparison of μ-LAM and LAM

Most, if not all, LAM systems utilize the laser external to the cutting tool, i.e. the laser heating system and cutting tool system are decoupled. This configuration is fundamentally different from the μ-LAM system where the laser and cutting tool are integrated into a single package; i.e. the laser energy is delivered by a fiber laser to and through a diamond cutting tool (as shown in Figure 2.21). This configuration provides a natural integration and alignment of the laser beam and cutting tool, and effectively puts the laser directly where is needed, i.e. at the chip formation zone. Use of an external or decoupled laser-cutting tool system would be problematic as precise alignment of the laser to the zone of HPPT material, which is only micrometers in extend, would be difficult on a machine tool (the material needs to be under extreme pressure, GPa, in order to achieve the HPPT, which is a requisite for the optimal μ-LAM system performance enhancement, and this high pressure only occurs at the contact interface between the diamond tool and the work piece (Si, SiC, etc.)). Diamond is used as the cutting tool material and IR laser sources are incorporated into the μ-LAM system. Diamond is transparent to IR radiation and thus the laser energy is actually “internal” to the cutting tool. The common features between the various laser machining systems are the use of lasers to thermally heat the work piece material and their application to very hard and difficult to machine materials, such as semiconductors and ceramics.

The advantages of the μ-LAM system, when coupled and utilized with a Diamond Turning Machine (DTM) for SPDT, are the high level of precision obtainable as a result of the machine tool and diamond tooling, coupled with the reduced thermal expansion as a result of the smaller volume of heated material (micrometers in extend) and the use of lower power lasers (mW to W). Also, the μ-LAM system is equally applicable to single crystal (semiconductors) and ceramics (as are laser based micro-machining systems), whereas the conventional (macro) LAM (as applied to semiconductors and ceramics) is limited to polycrystalline materials as it relies on heating and thermal softening the grain boundary material (sintering material), whereas the μ-LAM system actually preferentially heats and softens the individual grains (in a polycrystalline material). In summary, for the μ-LAM system, the material is first pressurized (due to cutting tool contact on work piece), a high pressure phase is generated and it is this material that is heated by the laser and thermally softened. In conventionally practiced LAM, the work piece is heated (actually the binder phase of the ceramic is the active medium) and then the machining takes place on this heated material.

2.8. Ductile Behavior of Nominally Hard and Brittle Semiconductor and Ceramic Materials

The μ-LAM research is closely related to work on high pressure phase transformations (HPPT). Most notably Gogotsi [96], Gilman [97, 98], O’Connor and Marsh [123], Pharr [99], Blackley and Scattergood [124], and Zhang [125] have a long and productive history of studying and working on engineering materials that exhibit HPPT. Of particular interest to this general field of study, and to the manufacturing processes associated with these materials, is the metallic nature of these high pressure phases. For it is the metallic characteristics of the high pressure phases of these materials (semiconductors and ceramics) that leads to their ductile response at room temperature and provides differentiated material behavior from their covalently bonded (atmospheric or low pressure phase) counterparts [102]. It is also the metallic nature of the high pressure phases of these materials that creates the opportunity for the μ-LAM system to preferentially heat and soften this material during processing. The μ-LAM system is based upon the knowledge of the existance and the properties of the high pressure phases of semiconductors and ceramics. In addition to experimental work, some theoretical work and numerical successes, for example molecular dynamics and quantum mechanics based calculations, have been demonstrated conditions suitable for achieving HPPT in these materials [126, 127, 128].

2.8.1. Current Research Trends in HPPT and Ductile Regime Machining of Brittle Materials

HPPT and ductile machining of brittle materials have been extensively investigated in the last decades [4, 5, 26, 44, 129]. A deeper understanding of the HPPT phenomenon and its role in ductile machining has been achieved [4]. There are well-established methodologies for conducting research in these fields of studies, such as nanoindentation and ductile-to-brittle (DBT) transition study.

In the study of HPPT, Diamond Anvil Cell (DAC), indenting and scratching tests are routinely conducted to investigate the high pressure behavior for materials of interest [37]. Different experimental parameters, such as tool shape and loading/unloading rate, are used to study their individual effect on the HPPT and the resultant mechanically induced ductile or plastic deformation [130]. Similarly, ductile regime/mode machining research mainly involves investigating the optimum combination of machining parameters, such as feed, depth of cut, cutting speed and tool geometry, to achieve a smooth and damage free surface. Characterizing techniques, such as AFM, micro-Raman, SEM, TEM and X-ray diffraction, are used to probe the surface and subsurface structure to evaluate the properties and characteristics of the resultant material and its surface. Some of these techniques can be incorporated into the material deforming process to make in-situ measurements [131-134]. The knowledge gained via these high-resolution instruments is indispensable to fully characterize and understand the HPPT phenomenon relative to ductile machining conditions.

The HPPT is at the core of the mechanism for achieving ductile regime machining of brittle materials such as semiconductors and ceramics [4, 5, 7, 58, 59]. Many of the scientific and laboratory findings investigating HPPT, such as modeling and simulations, DAC and nanoindentation, can be adapted and used in the study and pursuit of ductile machining [135, 136]. Ductile machining of brittle materials, via the HPPT, is essentially a material deformation and removal process that relies on the properties of the metallic high pressure phase to supply the requisite plastic deformation [74]. Ultimately, the current research interests in the study of HPPT and the resultant ductile machining of semiconductor and ceramic materials are closely coupled with the cost effective production of devices for the manufacturing industry.

Machining brittle materials in a ductile mode is appealing to manufacturers primarily for two reasons:

1) improved surface finish quality and reduced sub-surface damage as a result of plastic deformation rather than brittle fracture,

2) the potential to significantly reduce the machining cost by replacing the multiple grinding and polishing procedures with a single precision machining process.

In the development of processes for ductile regime machining of brittle materials, diamond grinding or diamond turning (most notably single point diamond turning-SPDT) methods are among the most promising operations for cost effective processes. These processes, grinding and SPDT, provide flexible and controllable product form compared to polishing processes, i.e. they are more deterministic. Polishing and lapping, employing loose or fixed abrasives, such as diamond grits, lead to more costly processes, as they tend to be slow and more time consuming. While these processes, polishing and lapping, can achieve high quality surface finishes, form accuracy is often sacrificed in the process. These processes, particular polishing, can be used as a final process after precision machining to achieve the final required surface roughness (to remove any feed marks resulting from the machining process).

A number of scientific publications have appeared within the last five years on the subject of ductile material deformation related to HPPT in semiconductor and ceramic materials [4, 5, 29-31, 54, 58, 59, 64, 74, 96, 137-139]. More researchers are embracing this new machining technique and understanding the relationship between the HPPT and the ductile regime machining of these nominally brittle materials at room temperature.

Since the hardness of SiC is approximately 30% of the hardness of diamond, machining SiC with a diamond tool is an extremely abrasive process. As a result of the abrasive material removal process, there are several limitations in terms of machining parameters that have to be considered. The primary limitation in the process of ductile mode machining is to not exceed the critical depth of cut or the DBT depth of the material. Exceeding the DBT depth during the machining process will result in fracture and thus leaving a poor surface finish. Another important parameter during machining is the feed. In general, lower feed rates result in a better surface finish however; lower feed rates also result in more tool wear due to the longer track length covered by the tool during machining. Tool wear can be crucial when trying to improve the surface finish of a SiC workpiece. Any wear along the cutting edge radius (rake and flank wear) will directly affect the machined surface finish, possibly causing cracks and fracture. A small chipped area or crack in the tool tip could potentially grow during the machining process, eventually causing the tool to fail. Tool failure at times can be observed in the cutting forces during the machining process. In general, low cutting forces are desired to minimize the diamond tool wear. The micro laser assisted machining (μ-LAM) process, which will be discussed in the next chapters, showed positive results in addressing the challenges faced in conventional ductile regime machining of SiC and also Si.

2.9. Background of the μ-LAM Technology

Micro laser assisted machining (μ-LAM) technology addresses roadblocks in major market areas, such as: precision machining of advanced materials and products, productivity, cost and quality control associated with semiconductors and ceramic materials for the mechanical, electrical and optical industries. The μ-LAM device uses a laser as a heating source to thermally soften nominally hard and brittle materials (such as ceramics and semiconductors) allowing for easier fabrication products. The μ-LAM device represents a new advanced manufacturing technology with applications to the many industries, including automotive, aerospace, medical devices, semiconductors and optics. This technology assists manufacturers, small through large organizations, who are developing new materials, processes and products to meet the ever increasing demands (performance, cost and quality) to complete for advanced products and production in the global market in the semiconductor and optical industries in particular, but also the electrical and mechanical markets. The target materials, semiconductors and ceramics (such as silicon-Si, silicon carbide-SiC), and the products, such as microelectronics and optical devices, are generally of high value and relatively high cost components that demand the best in manufacturing practices to produce a quality, cost effective and competitive product. Industries are hindered in their efforts to deliver products timely and cost efficiently using these materials, due to the inherent difficulties associated with their manufacture (the target materials are very hard and extremely brittle and thus not amenable to many traditional fabricating processes). New manufacturing processes are in demand by industries to improve existing products and to achieve capabilities for entirely new products. These potential opportunities were the basis for the origin of the previous work which led to the development of this technology. This technology has the potential to reduce tool wear, reduce machine down time, and enhance product quality, all of which reduce cost and increase the performance of the machining operation. Of potentially greater importance is that the technology has the capability of revolutionizing the production of semiconductor and ceramic components that rely on traditional fabrication methods, to allow for as of yet unrealized products and processes, i.e. current production methods limit the full potential (development) of advanced products made from these engineered materials due to the difficulty and high cost associate with their manufacture.

Based on previous fundamental basic research, primarily in the areas of both materials science and physics that provided the background for this study, it has been demonstrated that:

1. Semiconductors and ceramics undergo high pressure phase transformations, which convert them from covalent or ionic (hard-brittle) structures to metallic (softer-ductile) phases,
2. These high pressure phases occur under mechanical contact conditions that exist during precision machining operations, and
3. These high pressure metallic phases can be preferentially and selectively acted upon by electrical or optical methods to modify their mechanical properties (primarily as a result of heating and thermal softening) to render them easier to plastically deform.

3. OBJECTIVE, SIGNIFICANCE & INTELLECTUAL MERIT OF THE STUDY

3.1. Objective

The research objective of this study is to determine the potential enhancement that µ-LAM provides to the precision machining process for semiconductors and ceramic materials. The fundamental scientific characteristic of µ-LAM is evaluated by implementing an engineered system in conjunction with a Single Point Diamond Turning (SPDT) process. Semiconductors and ceramics are nominally hard, brittle and very difficult to machine by conventional methods. The material's hardness leads to significant tool wear during the machining process, such as SPDT [6, 10-12, 75]. The material's brittleness limits the material removal rate, by restricting the use of aggressive machining parameters such as high feeds and large depths of cut, and thus limits the ultimate productivity of the machining operation. The µ-LAM system extents the capability of the ductile regime machining process by heating and thermally softening these nominally hard and brittle materials, leading to decreased machining forces and ultimately resulting in less tool wear. The research study activity consists of designing, constructing, testing and evaluating a new machining system called µ-LAM. This study embodies three key research issues; predictability, producibility, and productivity. The experimental program, which includes synthesis and machining tests, leads to the identification of process attributes (speed, feed, depth of cut) that influence producibility (shape, dimensional control, and surface roughness). Productivity research is accomplished through the design, fabrication and testing of the µ-LAM system's capabilities. Verification of system capabilities and an evaluation of the potential to augment the machining process include tool wear, precision and repeatability, processing speed, laser power and wavelength, reliability, quality and cost considerations (materials, tooling, energy and environmental impacts).

3.2. Significance

Precision engineering applications of semiconductors and ceramics usually require very smooth surfaces (nanometer level surface roughness) and minimum subsurface damage (limited to micrometers or less in extent). These requirements necessitate the implementation of ductile regime processes (machining/grinding and/or lapping/polishing) and the avoidance of brittle fracture during manufacture. Brittle fracture during processing results in excessively rough surfaces and detrimental sub surface damage that must be removed in subsequent processing steps. These additional processing steps reduce the overall productivity and increase the manufacturing cost associated with machining these nominally brittle materials. This study is concerned with ductile regime machining and not brittle mode machining. Therefore, issues associated with micro cracks on the surface and in the sub surface region are purposefully avoided and are not directly addressed in this study. The potential for increased tool life and reduced surface and sub-surface damage will allow for improved productivity. Longer tool life will result in less frequent tool changes, and less damage means less post processing resulting in higher productivity and lower manufacturing costs.

3.3. Intellectual Merit

High pressure phase transformations (HPPT) of semiconductors and ceramics have been an area of research for about 50 years. Activity in the last 20 years has been directed at understanding the basic materials, physics, and chemistry of the phase transformation process mechanisms. To date, little informed work has been directed at using this accumulated knowledge to advance the manufacturing capability; beyond that which naturally occurs as a consequence of sufficient pressures being generated to form the high pressure phases in processes such as ductile regime machining.

The µ-LAM study uses this existing knowledge base and extends it significantly by intelligently and innovatively manipulating the material in its altered state (high pressure phase), and by taking advantage of the changes that occur in the material properties, such as decreased optical transparency particularly in the IR. These high pressure material phases will be acted upon in-situ during the machining process to effect significant changes to their mechanical properties and processing behavior, as a result of the laser heating and thermal softening. Through selective processing by lasers, preferential heating and thermal softening of the high pressure phases will occur, leading to enhanced ductility and increased ease of machining.

4. EXPERIMENTAL METHODS AND PROCEDURES

4.1. Materials

4.1.1. Single Crystal 4H-SiC Wafer

Polished single crystal wafers are becoming more common in the high power, high temperature electronics device industry. In this research 2 inch in diameter 4H single crystal wafer (from Cree Inc., USA) [140] was used as it provides for an excellent reference surface for determining the DBT and to establish the corresponding critical depth of cut. These wafers are also of high purity containing few defects, which helps in closely predicting the actual brittleness of the material. The physical properties of the material are given below in Table 4.1.

Table 4.1. Physical properties of single crystal 4H-SiC used in the study.

Polytype	Single Crystal 4H
Crystal Structure	Hexagonal
Bandgap	3.26 eV
Thermal Conductivity (n-type; 0.020 ohm-cm)	a~4.2 W/cm • K @ 298 K c~3.7 W/cm • K @ 298 K
Thermal Conductivity (HPSI)	a~4.9 W/cm • K @ 298 K c~3.9 W/cm • K @ 298 K
Lattice Parameters	a=3.073 Å c=10.053 Å
Mohs Hardness	~9

4.1.2. Single Crystal Si Wafer

The silicon wafers used throughout this study are 4 inch in diameter single crystal silicon (100) p type of 1~20 ohm-cm resistivity. The thickness of the wafers is 475-575 μm. One side of the wafer is polished and the other side is a matte finish. The scratches are all performed on the polished side of the single crystal Si wafer. Single crystal Si wafer are provided from UniversityWafer [141].

4.2. Experimental Procedure

4.2.1. μ-LAM Equipment Setup

The μ-LAM equipment system consists of a transparent diamond tip, a fiber-coupled IR diode fiber laser, a set of laser operation and control devices and a UMT tribometer.

4.2.1.1. Diamond Tooling

Diamond, the hardest material known to mankind, is an ideal candidate for tooling due to its ultra-hardness (≈100GPa), high resistance to wear and good thermal conductivity. This extreme hardness of diamond is necessary when attempting to cut an extremely hard and abrasive materials like SiC (H≈26GPa). The outstanding crystalline structure (tetragonal arrangement of the C-C covalent bonds) of diamond makes it possible to fabricate tool tips with very sharp cutting edges (20 to 50 nm). The ability to fabricate single crystal diamond tools with extremely smooth finish (Ra≈ 3nm), makes it ideal for SPDT ceramics to improve surface finish with a high degree of accuracy [142]. Synthetic single crystal diamond (approximately same properties as natural diamond) tools from Chardon Tools Inc. (Ohio, USA) and Adamant Kogyo Co., Ltd. (Japan) were used for the experiments which will be discussed in detail in the later chapters of this thesis. These synthetic diamonds are usually grown at high temperature and pressure from carbon feedstock.

4.2.1.2. UMT Tribometer

The equipment used to carry out all of the scratching/machining experiments was the Micro-Tribometer (UMT) from the Center for Tribology Research Inc. (CETR, California). This equipment was developed to perform comprehensive micro-mechanical tests of coatings and materials at the micro scale [143]. This system facilitates the cutting speeds as low as 1μm/sec at nanometric cutting depths. The tribometer is a load controlled device where the required thrust force (F_z) is programmed by the user to obtain the desired DoC (based on the tool geometry and work piece material properties). The equipment includes a dual-axis load cell that is capable of continuously monitoring and recording the thrust forces (F_z) and cutting forces, F_x, (obtained as an output parameter from the cutting experiment). The UMT micro-tribometer system used in the experiments is shown in Figure 4.1.

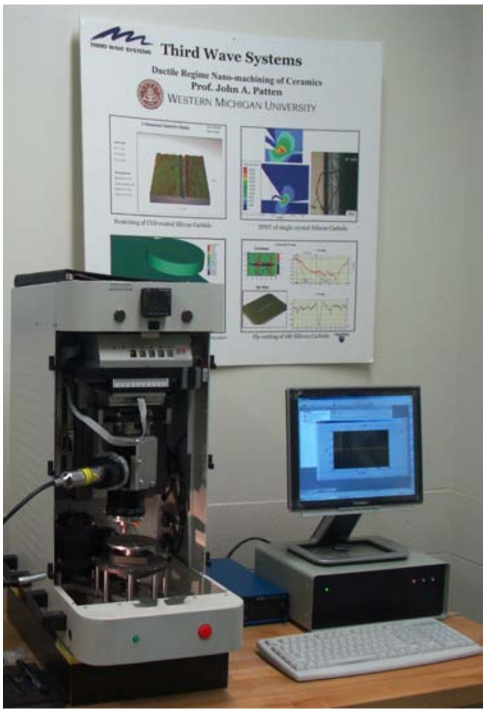

Figure 4.1. UMT micro-tribometer from the Center for Tribology Research Inc. (CETR).

4.2.1.3. Laser Heating System

The laser heating system (Figure 4.2) consists of a transparent diamond tip, a fiber-coupled IR diode laser (1480 nm laser Diode Module, Manufactured by Furukawa., see Figure 4.2 b) and a set of laser operation and control devices (LDC-3744B Laser Diode Controller, LDM-4980 Series Laser Diode Mount, ILX Light Wave Inc., see Figure 4.2 a-b). The higher power IR laser diode (400 mW) heating system is designed to heat the high pressure metallic silicon when the diamond tip is scratching on the silicon surface. The power analysis of this heating system is necessary to serve as a reference for future improvement on the design and for the eventual design of a micro laser assisted machining (μ-LAM) system.

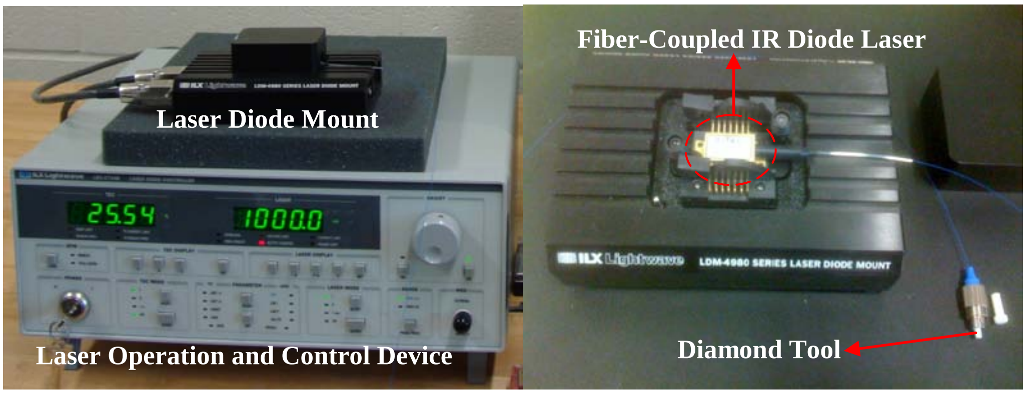

(a) **(b)**

Figure 4.2. The laser heating system used in the experiments.

4.3. Characterization Techniques

4.3.1. Atomic Force Microscopy (AFM)

The laser heating effect is verified by atomic force microscopy (AFM) measurements of the laser heated scratch grooves. The machined surfaces were analyzed by using a Pico 2100 AFM with imaging software.

4.3.2. White Light Interferometry (WYKO)

Optical profiling is a non-contact, two- and three-dimensional method for rapid measurement of step heights, roughness and surface topography, from nanometer-scale roughness through millimeter-scale steps. Measurements take just a few seconds, with vertical resolution to 0.1 nm. Optical profilers can measure a wide range of samples such as, films, MEMS, semiconductor wafers, biomedical and optical materials, etc.

Light from a source passes through a beam splitter, with part travelling to the sample and part to a smooth reference surface. The reflected beams recombine to form a pattern of interference "fringe" – light and dark bands connecting points of equal height. The optical system translates vertically, and a series of interference patterns is captured (see Figure 4.3). These "interferograms" are analyzed to determine the surface height at each pixel. The surface height data can be analyzed in many ways.

White light interferometric optical profiler from Veeco (WYKO) was used in this study. Two-dimensional and three-dimensional cutting surface profiles (with and without laser) were investigated using a white light interferometer. The laser heating effect is also verified by WYKO white light interferometry measurements of the laser heated scratch grooves.

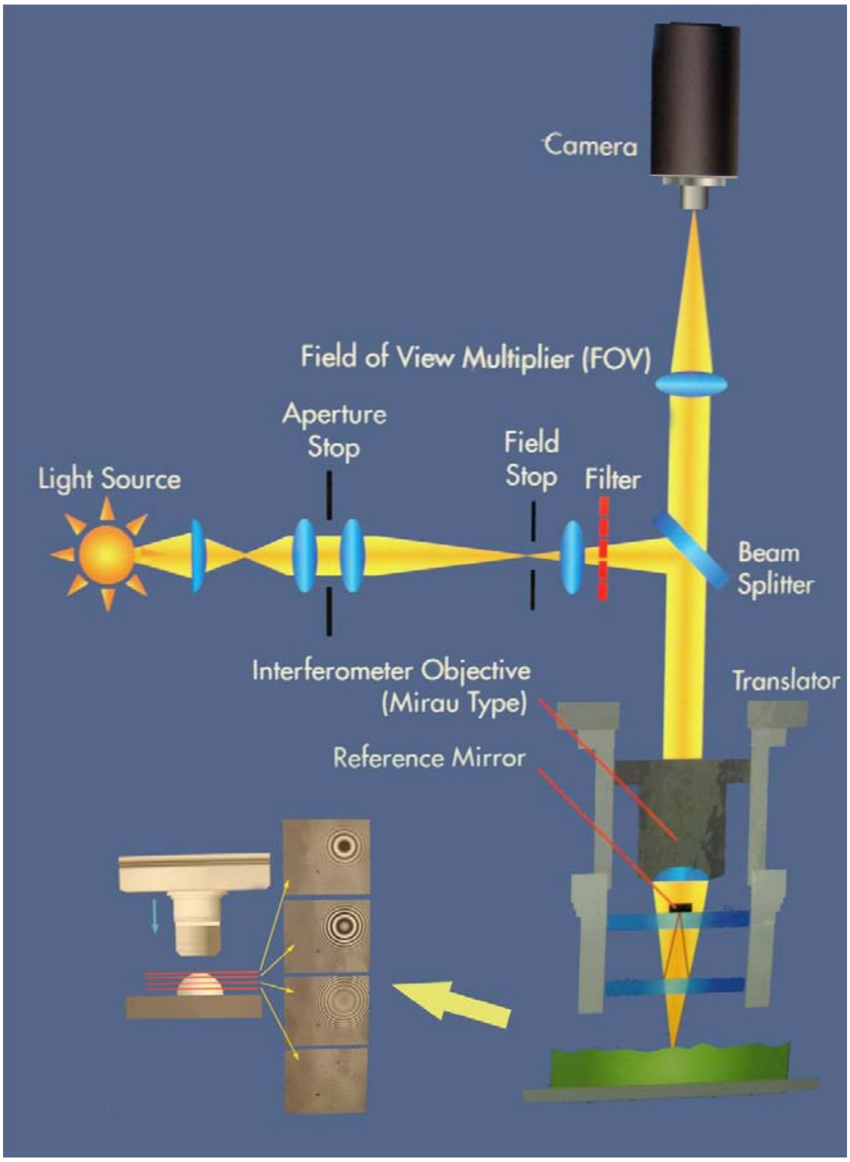

Figure 4.3. Schematic view of a white light interferometer.

4.3.3. Micro-Raman Spectroscopy

Micro-Raman spectroscopy examinations of the material within the scratch impressions were carried out to identify any possible phase transformations that may have occurred during the scratching and laser heating processes. The machined (with and without laser) single crystal wafers were examined using the Renishaw inVia Reflex Micro-Raman Spectrograph (Figure 4.4) at Argonne National Laboratory (ANL) - Center for Nanoscale Materials (CNM).

Figure 4.4. Renishaw inVia Reflex Micro-Raman Spectrograph used in the experiments.

A 514.5 nm ArION laser (green laser) with a max delivered power of 19mW and a 442 nm HeCd laser (blue laser) with a max delivered power of 40mW were used for micro-Raman spectroscopic measurements of the laser heated and non-laser heated scratches on the workpiece. The point analysis was conducted with the spot size of 1μm (×100 objective lens). A 100X objective lens with a numerical aperture (NA) of 0.95 was used so that the focused laser spot size was 1μm. The spot size was easily to be pointed to any locations within the machined groove to investigate and identify any possible phase transformations that may have occurred during the machining with and without laser heating processes.

4.3.4. Scanning Electron Microscopy (SEM)

An ISI-DS 130 scanning electron microscope (SEM) with upper-stage STEM capability and a macro stage that can work with specimens up to 6 inches in diameter, and equipped with a backscatter detector and a KEVEX elemental analysis and mapping system was used to image and analyze the machined surfaces and chips after μ-LAM process.

5. POWER CHARACTERIZATION OF THE μ-LAM LASER HEATING SYSTEM

5.1. Introduction

The laser heating system consists of a transparent diamond tip, a fiber-coupled IR diode laser (1480nm laser Diode Module, Manufactured by Furukawa) and a set of laser operation and control devices (LDC-3744B Laser Diode Controller, LDM-4980 Series Laser Diode Mount, ILX Light Wave Inc.). The IR laser diode (400 mW) heating system is designed to heat the high pressure metallic phase when the diamond tip is scratching/machining on the Si or SiC surface. The power analysis of the heating system is necessary to serve as a reference for future improvement on the design, and for the eventual design of a micro laser assisted machining (μ-LAM) system.

In this chapter the assembly of the diamond heating system is introduced first, followed by a laser power distribution analysis using both experimental measurements (IR CCD Camera, Spiricon SP-1550M). Thermal images of the diamond tip and the adhesive around the tip taken by an IR thermal camera (Phoenix) are analyzed to determine the laser heating effect on the diamond tip and the epoxy. Finally, based on the analysis and results, the available laser energy, which can be used to heat the high pressure metallic phase, is calculated. Some suggestions for the improvements of the power and conversion efficiency (laser to thermal energy) of the laser heating system are presented.

5.2. Diamond Tip Attachment

A 5μm radius single crystal diamond tip is attached to the facet of a laser Zirconia ferrule using UV-cured epoxy (Figure 5.1 and 5.2). The diamond tip was partially embedded in the epoxy for the laser heating experiments. Lesser epoxy was applied to bond the diamond for the laser heating experiments, which resulted in exposing more length of the diamond tip, as shown in Figure 5.1. This is to prevent the lR laser from overheating the epoxy, which could subsequently lead to lessening the strength of the bond between the diamond tip and the ferrule. The assembly procedure results in a thin layer of epoxy (estimated thickness 50nm) between the flat end of the diamond tip and the ferrule surface, which cannot be seen from outside. The laser beam coming out of the laser fiber end will pass through this layer of epoxy before it enters the diamond (see Figure 5.1). Therefore, the optical transparency and thermal properties of the epoxy directly affect the efficiency of the power output of the system.

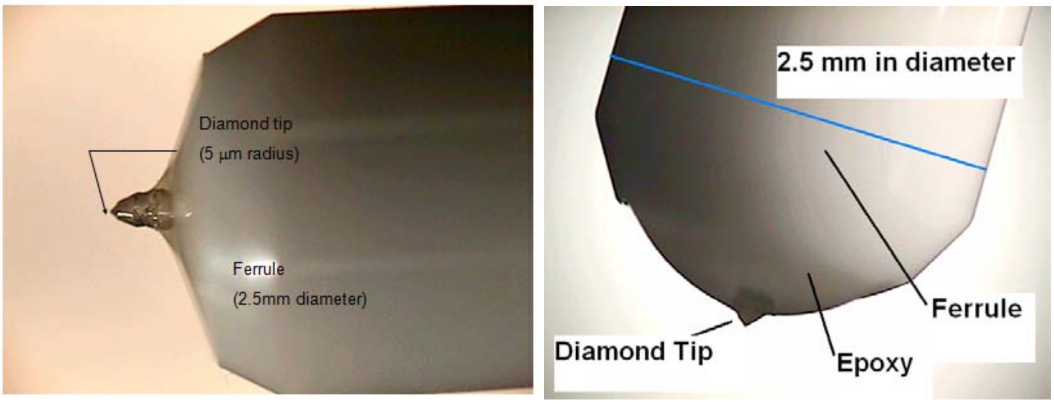

Figure 5.1. Diamond tip attachment for IR laser heating: 5 μm radius diamond tip attached on the end of the ferrule using epoxy.

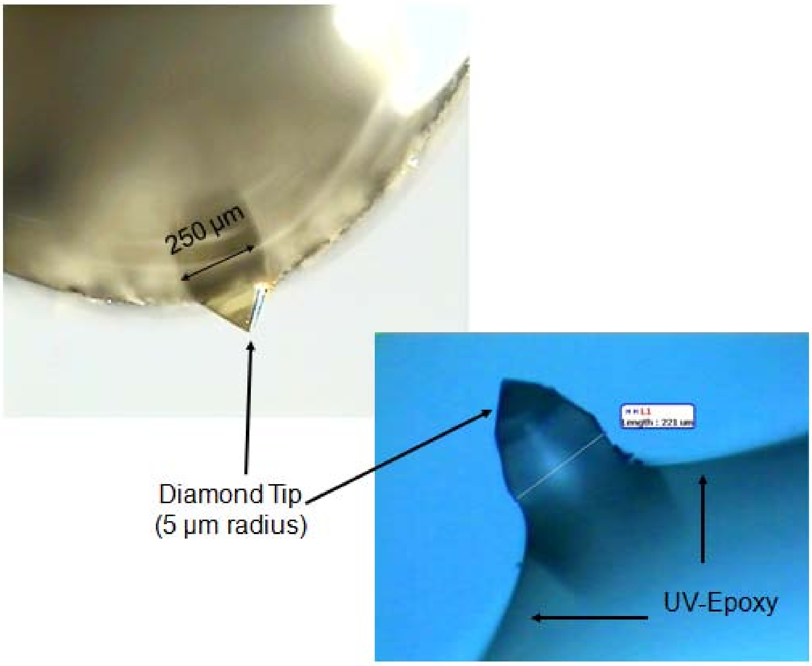

Figure 5.2. Diamond tip attachment for IR laser heating: close up on diamond tip embedded in the solidified epoxy.

5.3. The Laser Wavelength

The wavelength of the laser is chosen based on the transparency band of diamond, work piece, and the opaqueness band for metallic materials. The availability and the power of the laser are included in the selection consideration as well. Diamond is transparent in almost the entire range of the electro-magnetic spectrum. The most important weighing factor for the selection of the laser wavelength is the difference between the transparency of the high pressure metallic and covalent phase of the work piece, which is the essential concept of the eventual heating test. For example covalent silicon, like diamond, is transparent to IR radiation. The potential laser candidates are among the most commonly used communication (diode) fiber lasers available. A 400mW with a wavelength of 1480nm diode laser with a coupled-fiber is used for the experiments.

5.4. The µ-LAM Tooling Setup

The IR laser beam is guided from the diode laser through a 10 µm fiber optic cable to the zirconia ferrule, which is attached to the diamond tool (see Figure 5.3). A simple µ-LAM system configuration used in the experiments is shown schematically in Figure 5.4.

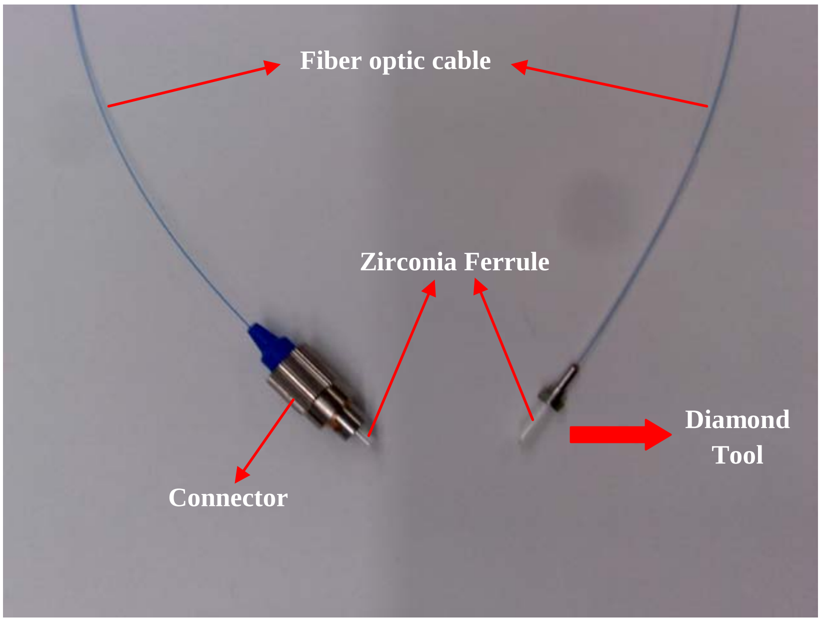

Figure 5.3. Fiber coupled diamond tool seen with the connector.

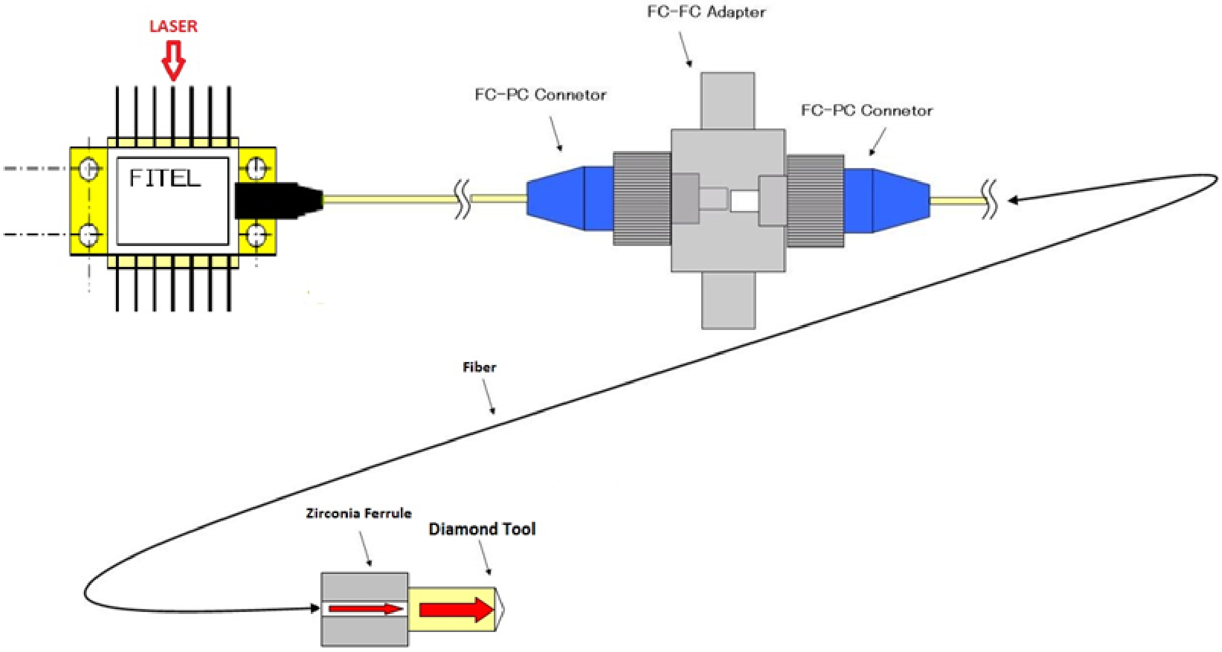

Figure 5.4. The schematic μ-LAM system configuration for the 5 μm radius diamond tool setup.

5.5. Laser Power Characterization

The total laser power coming out of the diamond tip is measured and the results indicate significant output laser power loss. This current chapter is focused on obtaining the energy intensity at the center of the beam as well as determining the sources of the laser power attenuation. The latter provides useful information on how to improve the diamond tip attachment technique, and thus result in a more efficient laser heating system.

5.5.1. Total Laser Power Calibration

Total laser power is measured using a high resolution (1 mW resolution) laser power meter with digital display (Model #3802 Sensor Interface Module (SIM) and #3831 Thermal Sensor, New Focus Inc.). The diamond tip is placed orthogonal to the sensor window (19 mm diameter) at the center of the sensor window. The measurement setup is covered by black plastic, which shields the room lights that may interfere with the power measurements.

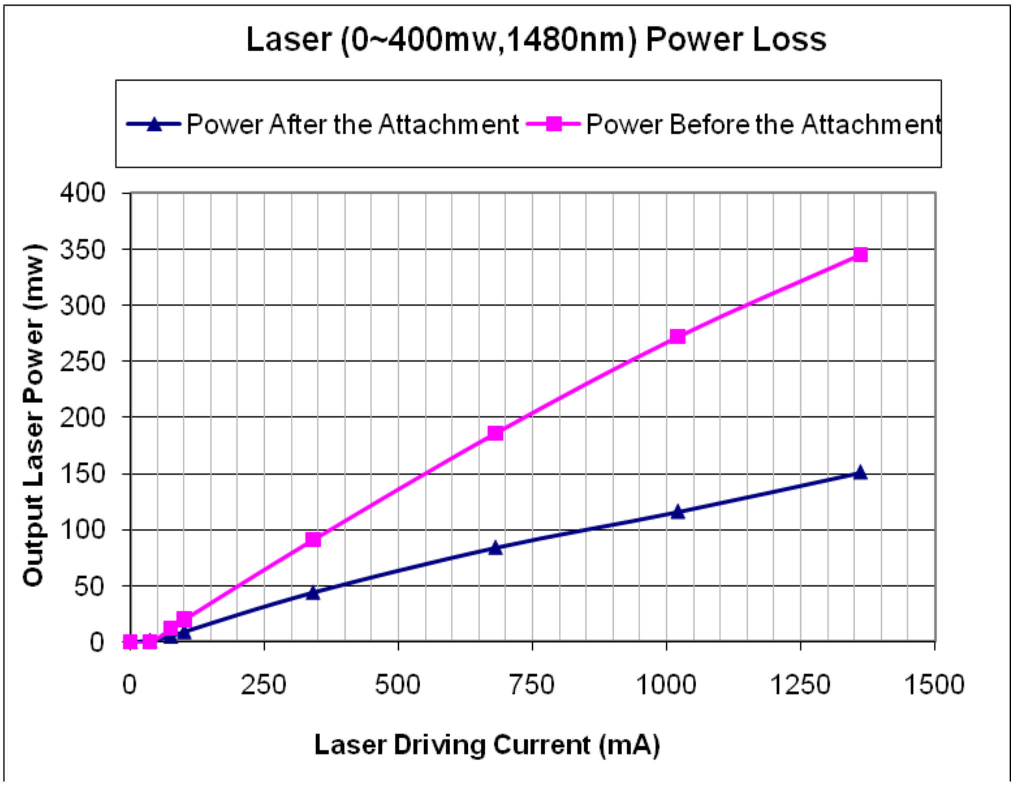

Figure 5.5. Laser output power measurements with and without the diamond tip attached.

Figure 5.5 shows the output laser power measurement result. The maximum laser power decreases from its original 350 mW to approximately 150 mW (at maximum laser diving current of 1400 mA). Approximately 60% of the laser power is lost after attaching the diamond tip to the ferrule. This leads to the question of where the lost laser power goes, i.e. what accounts for this power loss. The remaining or transmitted laser power (max. 150 mW) is available to heat/soften the high pressure phase of the material. The next few sections address the laser power loss associated with the diamond tip and the epoxy used for the assembly.

The potential reasons that could cause the observed laser power loss are scattering and refraction by the diamond and the epoxy. Some absorption by the epoxy cannot be completely ruled out, because it is 86% transparent to IR radiation at 1480 nm wavelength.

5.5.2. Laser Beam Profile

An IR CCD camera (Spiricon SP-1550M) with beam analyzer software (Spiricon LBA-PC series) is used to qualitatively observe the laser beam profile coming out of the diamond tip. The laser beam profile before attaching the diamond tip is also taken for comparison purpose. The IR camera is capable of viewing IR emitting devices and IR lasers only in the spectral range of 1460 nm to 1625 nm, and the laser used is at 1480 nm wavelength.

The laser emits a nearly ideal symmetric shape beam (10 μm diameter) with a Gaussian distribution, as shown in Figure 5.6 a and b. After attaching the diamond tip, the beam is slightly distorted but the power remains nearly Gaussian distribution (as shown in Figure 5.7 a). When the camera is set to image the laser beam slightly out of focus, as sown in Figure 5.7 b, scattering effect is being observed, indicating that the diamond tip is scattering the laser beam.

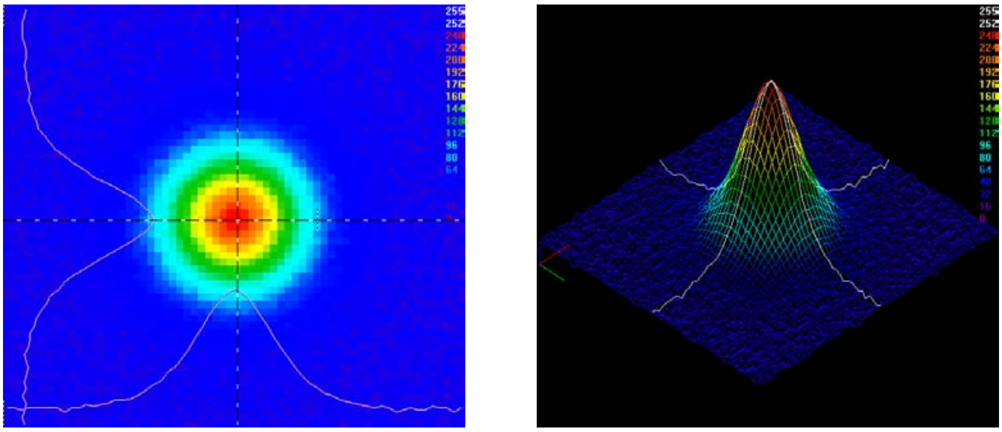

(a) **(b)**

Figure 5.6. Laser beam profile before the attachment of the diamond tip (the laser driving current is 214 mA, which corresponds to approximately 60 mW)

(a) 2-D beam profile,

(b) 3-D beam profile.

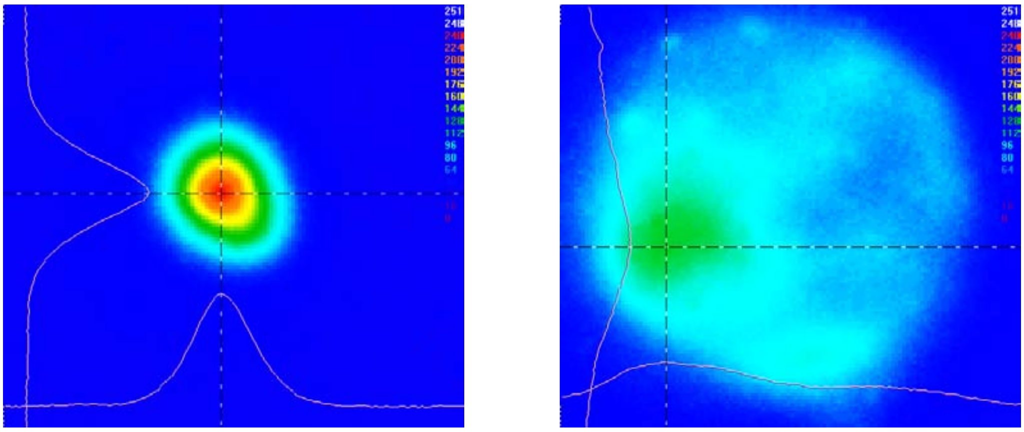

(a) **(b)**

Figure 5.7. Laser beam profile after attachment of the diamond tip.

(a) 1480nm IR laser beam profile on focus,

(b) out of focus (the laser driving current is 580mA in both cases, which corresponds to approximately 75 mW).

Although the laser beam emerging out of the diamond tip is nearly a Gaussian distribution, there is some scattering that occurs when the beam goes through the epoxy and the diamond tip, as evidence by the out of focus image (refer to Figure 5.7 b). One cause of the scattering is presumed to be due to the interface between the Zirconia ferrule and the diamond tip, which includes the thin layer of the epoxy between the back (flat) of the diamond tip and the ferrule. Another potential source of scattering may be the imperfect cylindrical geometric shape of the diamond tip (Figure 5.8 a & b).

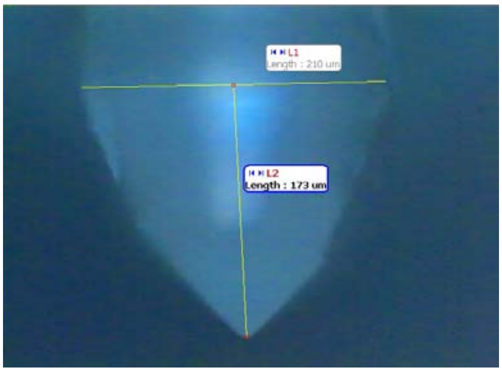

(a) **(b)**

Figure 5.8. (a) off cylinder shape

(b) irregular geometry of the tip end.

Further tests confirm that there is a small but not insignificant amount of IR radiation coming from the side of the tip in addition to the forward scattering (as shown in Figure 5.9 a & b). The IR radiation emerging from the side of the diamond tip is considerably less than the amount of radiation emerging in the forward direction (as shown in Figure 5.10 a & b). Also, a bump in Figure 5.10 b at the joint location, to the left of the major peak, where the diamond tip and the ferrule are bonded indicates some radiation emerging from that interface. It is estimated, after comparing the relative intensity of the laser beams shown in Figure 5.10 (a) and (b), that 40 to 60% of the total laser radiation is scattered out the side of the diamond tip, if the profile is assumed constant around the circumference, i.e. for 360°. This result is consistent with the previous total power measurement obtained from the power meter, where there is nearly a 60% loss compared to the initial laser power (350mW to 150 mW as shown in Figure 5.5).

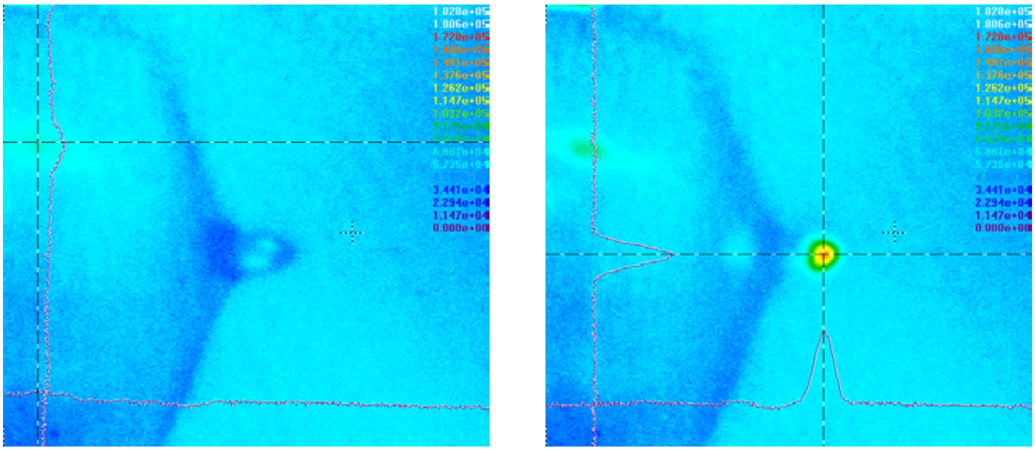

(a) **(b)**

Figure 5.9. (a) Diamond tip side view with the laser turned off,

(b) Diamond tip side view with the laser running at 214 mA (room light is on in both cases).

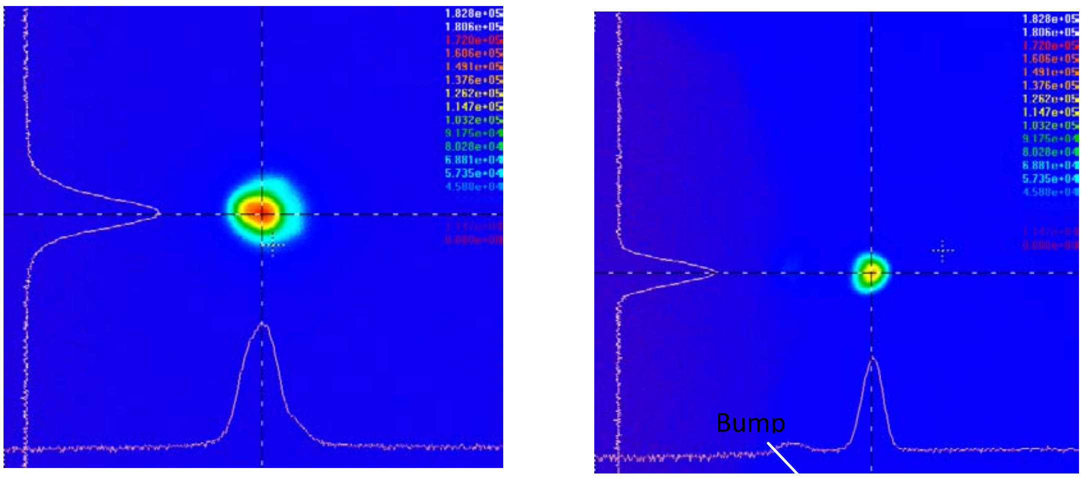

(a) **(b)**

Figure 5.10. (a) diamond tip front view image with laser running at 214mA

(b) diamond tip side view image with the laser running at 214 mA (room light is off in both cases).

5.6. IR Thermal Camera Images of The Diamond Tip

A Phoenix^{TM} camera system with Real-Time Imaging Electronics (RTIE) is used to take thermal images of the diamond tip to determine if the diamond and/or the epoxy absorbs the IR laser radiation. The camera head is configured with a large format (640x512 pixels) sensor in the MWIR (middle wavelength infrared, 2.0-6.0 μm) wavelengths.

Diamond used in this experiment is transparent to the IR wavelength (1480 nm). Diamond has excellent thermal conductivity, which means that diamond will conduct the heat away readily. In principle, there should be a minimal increase in the diamond temperature, due to heating by the IR laser, or due to thermal conduction from the heated material. The UV-epoxy is 86% transparent at 1480 nm wavelength. But because of the thin film of UV-epoxy between the fiber and the diamond tip, it cannot be ruled out the possibility that some heat absorption and/or scattering taking place at the interface.

The thermal images of the diamond tip are taken at different laser power levels (see Figure 5.11). The photon intensity distribution, viewed from the emitting direction of the laser, is evenly spread out. The side view of the diamond tip has different heat distribution. The photon intensity at the tip end increases quicker than other parts of the tip and the tip end remains the highest of the entire diamond tip at any laser power level. As the laser power increases, the detected photon intensity within the body of epoxy also increases gradually from inside to outward. The part of epoxy that is closely around the diamond tip emits more photon than the rest of the epoxy. Also, there is a hot stripe appear near the joint interface between the diamond tip and the ferrule, which is about the same location as where the bump appears in the IR CCD camera image (see Figure 5.10 b).

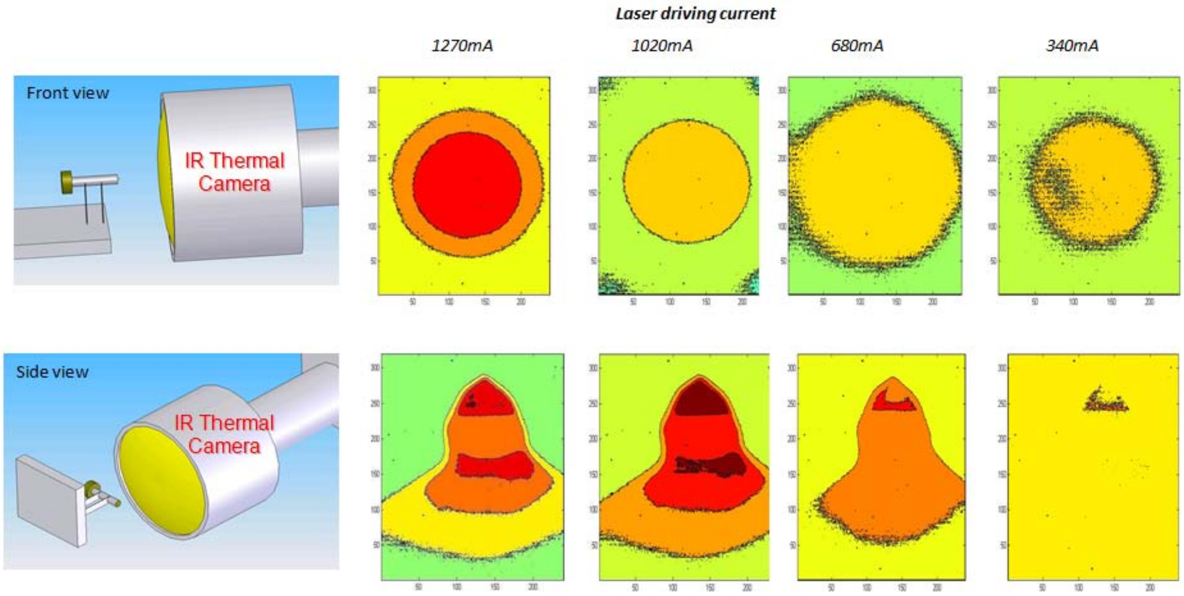

Figure 5.11. IR thermal images of the diamond tip with the laser running at different laser driving currents.

Upon turning the laser off, the IR images of the tip show an immediate change of intensity, i.e. the IR images return to the intensity that existed before the laser is turned on, which indicates that there is not much temperature rise. This further suggests that the IR camera may also be detecting the laser beam itself, as the radiation signal disappears as soon as the laser power is switched off. If the diamond tip is heated by the IR laser, it would be expected that the IR thermal image persists for some finite time after the IR laser is turned off. The apparent increase in temperature is mainly due to or from the laser's IR radiation, i.e. the IR thermal camera is also sensitive to the IR laser wavelength. It is believed that the diamond tip itself is not being heated up significantly, noting that the very end of the diamond tip is not emitting any appreciable IR radiation from the side.

The wavelength spectrum of the 1480 nm laser (1435nm - 1515nm) is close to the lower limit of the camera's detecting range (2 µm). It is assumed that the 2 µm lower limit is not a sharp cutoff, so that some potential for overlap exists, i.e. the IR camera may detect the IR laser. A possible solution to verify if the detected photon energy is from the laser radiation or the heated diamond and epoxy thermal radiation if the camera is detecting the IR beam itself is to put a filter in the measurement loop to cut off smaller wavelengths, for instance below 3µm, this would separate more distinctly the camera's sensitivity range from the IR laser wavelength.

5.7. Conclusion

In conclusion, from the laser beam profile measurements IR radiation emitted out the side of the diamond tip is largely responsible for the approximately 60% loss of the laser power, based upon the available laser energy compared to the laser power emitted from the end of the diamond tip in the forward direction. The thermal images of the diamond tip with laser running at different laser power levels showed that the IR thermal camera can detect the laser radiation. Although the attachment of the diamond tip causes significant laser power loss, the emitted laser beam from the diamond tip end remains Gaussian distributed across its 10 μm diameter. A normal distribution provides reasonable estimation of the laser beam intensity distribution (see Figure 5.12). For instance, 68% the laser power is concentrated within the central 3.3 μm (+/1 std. dev.) diameter portion of the laser beam on the center circle of the laser beam. Usually in the scratching test, the width of the contact is about 2 μm. From Figure 5.12, it is estimated that 42% of the total laser power, which is 63 mW, is within a 2 μm diameter center area.

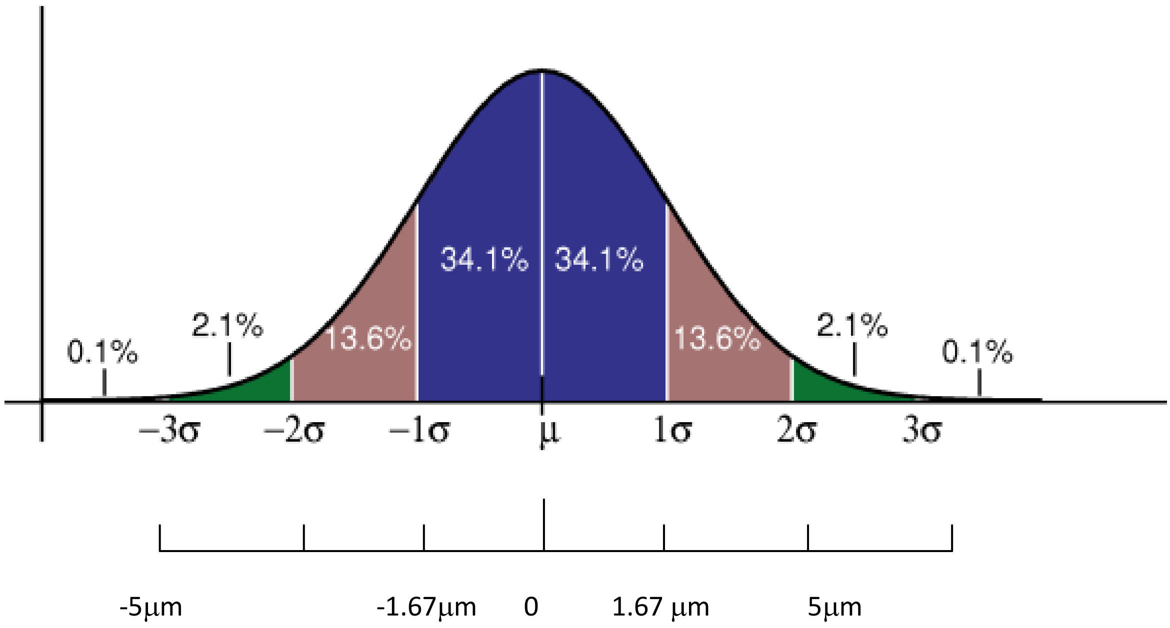

Figure 5.12. Gaussian distribution of the laser beam intensity.

The observed laser power loss is significant due to the diamond tip attachment. This is an area where opportunities exist to improve upon the design for future IR laser assisted heating systems. The direct contact between the epoxy and the laser fiber facet is generally not recommended, due to the potential danger for the laser radiation to overheat the fiber facet.

6. DETERMINATION OF THE LASER ABSORPTION FOR Si and SiC

6.1. Introduction

The optical properties (esp. % absorption) of Si and SiC (3C, 4H and 6H polytypes) at normal conditions (1atm, and ambient temperature) for the IR range is already known by the literature. But it is not possible to identify appropriate citations of the optical properties of the Si and 3C, 4H and 6H poly-types of SiC in the IR range at higher pressures.

The absorption% for three distinct wavelengths namely 500 nm, 1000 nm and 1500 nm at various thickness of the workpiece sample was calculated for Silicon (Si-I), high pressure phase silicon (Si-II) and for 3C, 4H and 6H Silicon Carbide (SiC).

The values for the wavelength were calculated using the following equation (where h represents Plank's constant and c is the speed of light):

$$\lambda = hc / E(eV) \tag{6.1}$$

We can define a complex index of refraction:

$$\tilde{\mathbf{N}} = \mathrm{n} + \mathrm{ik} \tag{6.2}$$

Here, n is the refractive index indicating the phase velocity as $\frac{v}{c}$, while κ is called the extinction coefficient, which indicates the amount of absorption loss when the electromagnetic wave propagates through the material. Both n and κ are dependent on the frequency (wavelength).

The effect that n varies with frequency is known as dispersion. In regions of the spectrum where the material does not absorb, the real part of the refractive index tends to increase with frequency. Near absorption peaks, the curve of the refractive index is a complex form given by the Kramers–Kronig relations, and can decrease with frequency.

Since the response of materials to alternating fields is characterized by a complex permittivity, it is natural to separate its real and imaginary parts, which is done by convention in the following way:

$$\widetilde{\epsilon(\omega)} = \varepsilon_1(\omega) + i\varepsilon_2(\omega) \tag{6.3}$$

$$\epsilon_1(\omega) = n^2 - k^2 \tag{6.4}$$

$$\epsilon_2(\omega) = 2nk \tag{6.5}$$

For normal incidence, the normal reflectance is then obtained:

$$R = \frac{(1-n)^2 + k^2}{(1+n)^2 + k^2} \tag{6.6}$$

and if $k < 10^{-6}$, then

$$R = \frac{1-n^2}{1+n^2} \tag{6.7}$$

For absorption coefficient values greater than zero, the percentage of total light reflected can be determined using equation:

$$R \approx R_1 + (1 - R_1)R_1 e^{-\alpha 2z} - (1 - R_1)R_1^2 e^{-\alpha 2z} + (1 - R_1)R_1^3 e^{-\alpha 4z} - (1 - R_1)R_1^4 e^{-\alpha 4z} + \cdots \quad (6.8)$$

Each term in the infinite series is associated with the successive reflections as the light bounces between the surfaces of the silicon wafer. Similarly, the percent transmission can be determined using equation:

$$T \approx (1 - R_1)e^{-\alpha z} - (1 - R_1)R_1 e^{-\alpha z} + (1 - R_1)R_1^2 e^{-\alpha 3z} - (1 - R_1)R_1^3 e^{-\alpha 3z} + \cdots \quad (6.9)$$

where the percent absorbed light is given by equation:

$$A \approx 1 - (R + T) \quad (6.10)$$

When the absorption coefficient equals zero, equation can be simplified to the following equation:

$$R \approx 2R_1 / (R_1 + 1) \quad (6.11)$$

$$\frac{I_r}{I_o} + \frac{I_t}{I_o} + \frac{I_a}{I_o} = 1 \text{ or } R + T + A = 1 \quad (6.12)$$

$$\frac{I_a}{I_o} = 1 - \left(\frac{I_r}{I_o} + \frac{I_t}{I_o}\right) \quad (6.13)$$

$$\frac{I_t}{I_o} = T = (1-R)^2 e^{-\alpha z} \tag{6.14}$$

Nomenclature

n	Index of refraction
k	Extinction coefficient
ε_1	Real part of dielectric permittivity
ε_2	Imaginary part of dielectric permittivity
α	Absorption coefficient
β	Transmission coefficient
I_o	Intensity of incident ray
I_r	Intensity of reflected ray
I_t	Intensity of transmitted ray
I_a	Intensity of absorbed ray
z	Thickness of the slab
R	Percent reflectivity
T	Percent transmissivity
A	Percent absorptivity

The following section shows the results obtained from various references and calculated for absorption% of laser for Si-I, Si-II (High Pressure Phase of Si which is metallic) and 3C, 4H and 6H SiC at varying depth of the workpiece.

6.2. Results

6.2.1. Calculations for Silicon (Si-I) at Normal Pressure

Table 6.1. Optical properties of Si-I at normal pressure and varying wavelenghts [144, 145].

Wavelength (nm) ➔	**500**	**1000**	**1500**
n	4.293	3.592	3.4806
k	0.0728	$3.91x10^{-4}$	$2x10^{-7}$
$\boldsymbol{\varepsilon_1}$	18.42455	12.90246	12.1145
$\boldsymbol{\varepsilon_2}$	0.62506	0.00282	$6.96x10^{-7}$
α (m^{-1})	$1.82957x10^{6}$	$4.9784x10^{3}$	0.83858
β	$5.3947x10^{7}$	$2.23607x10^{7}$	$1.456x10^{7}$
R	0.3871	0.3163	0.4698

Table 6.2. Calculated R%, T% and A% of laser for Si-I at varying depth/thickness of the workpiece material.

Wavelength (nm)	Thickness (µm)	R (%)	T (%)	A (%)
500	20	38.71	0.00	61.29
	50	38.71	0.00	61.29
	80	38.71	0.00	61.29
	110	38.71	0.00	61.29
	200	38.71	0.00	61.29
	260	38.71	0.00	61.29
1000	20	31.63	42.32	26.05
	50	31.63	36.45	31.93
	80	31.63	31.39	36.98
	110	31.63	27.04	41.34
	200	31.63	17.27	51.10
	260	31.63	12.81	55.56
1500	20	46.98	52.54	0.48
	50	46.98	52.54	0.48
	80	46.98	52.53	0.49
	110	46.98	52.53	0.49
	200	46.98	52.53	0.49
	260	46.98	52.53	0.49

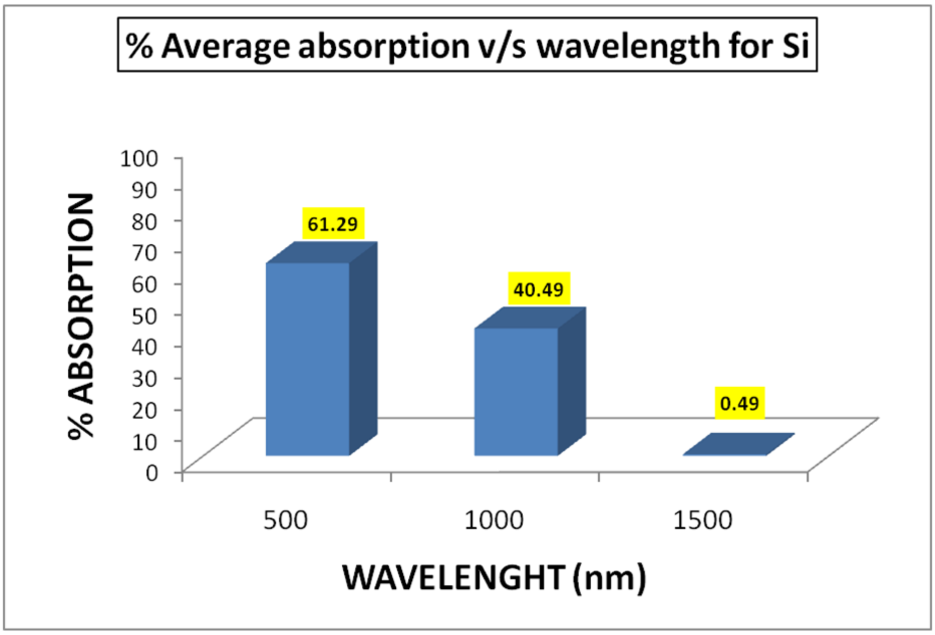

Figure 6.1. Average absorption% versus wavelength for Si-I at normal pressure at a constant depth/thickness of the workpiece material.

6.2.2. Calculations for Silicon II (Si-II) at High Pressure (13.2 GPa)

Table 6.3. Optical properties of Si-I at high pressure (13.2 GPa) and varying wavelenghts [146].

Wavelength (nm) ➔	**500**	**1000**	**1500**
n	5.67	15.326	37.97116
k	3.52734	0.71771	14
ε_1	19.70677	234.37117	1441.682
ε_2	40	22	15
α (m^{-1})	8.8658×10^7	9.629×10^7	1.59×10^8
β	7.124×10^7	9.01416×10^6	1.6537×10^6
R	0.49	0.77	0.90

Table 6.4. Calculated R%, T% and A% of laser for Si-II at varying depth/thickness of the workpiece material.

Wavelength (nm)	**Thickness (μm)**	**R (%)**	**T (%)**	**A (%)**
500	20	49.00	0.00	51.00
	50	49.00	0.00	51.00
	80	49.00	0.00	51.00
	110	49.00	0.00	51.00
	200	49.00	0.00	51.00
	260	49.00	0.00	51.00
1000	20	77.00	0.00	23.00
	50	77.00	0.00	23.00
	80	77.00	0.00	23.00
	110	77.00	0.00	23.00
	200	77.00	0.00	23.00
	260	77.00	0.00	23.00
1500	20	90.00	0.00	10.00
	50	90.00	0.00	10.00
	80	90.00	0.00	10.00
	110	90.00	0.00	10.00
	200	90.00	0.00	10.00
	260	90.00	0.00	10.00

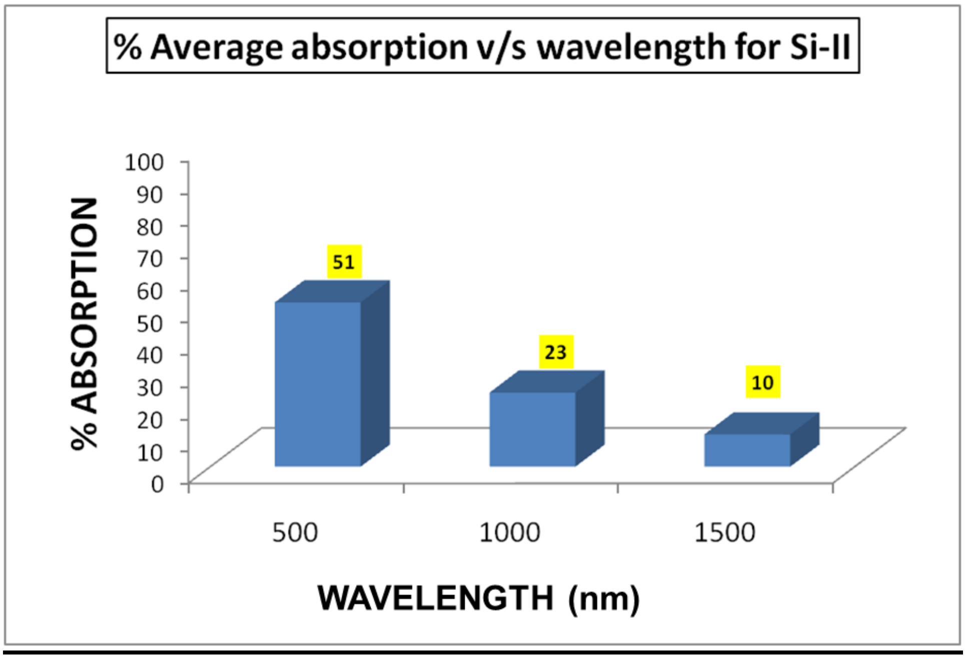

Figure 6.2. Average absorption% versus wavelength for Si-II high pressure (13.2 GPa) at a constant depth/thickness of the workpiece material.

6.2.3. Calculations for Silicon Carbide (3C-SiC) at Normal Pressure

Table 6.5. Optical properties of 3C-SiC at normal pressure and varying wavelenghts [147].

Wavelength (nm) →	**500**	**1000**	**1500**
n	1.18322	1.08973	1.04283
k	2.21852	2.35149	2.39732
ε_1	5	5.125	5.25
ε_2	0.4	0.1875	0.0875
α (m^{-1})	8.75E+05	2.08E+05	6.54E+04
β	1.150E+07	5.68E+06	3.74E+06
R	0.0070	0.0018	0.0004

Table 6.6. Calculated R%, T% and A% of laser for 3C-SiC at varying depth/thickness of the workpiece material.

Wavelength (nm)	Thickness (µm)	R (%)	T (%)	A (%)
500	20	0.70	0.00	99.30
	50	0.70	0.00	99.30
	80	0.70	0.00	99.30
	110	0.70	0.00	99.30
	200	0.70	0.00	99.30
	260	0.70	0.00	99.30
1000	20	0.18	1.57	98.25
	50	0.18	0.00	99.81
	80	0.18	0.00	99.82
	110	0.18	0.00	99.82
	200	0.18	0.00	99.82
	260	0.18	0.00	99.82
1500	20	0.04	27.02	72.94
	50	0.04	3.80	96.16
	80	0.04	0.53	99.42
	110	0.04	0.08	99.88
	200	0.04	0.00	99.96
	260	0.04	0.00	99.96

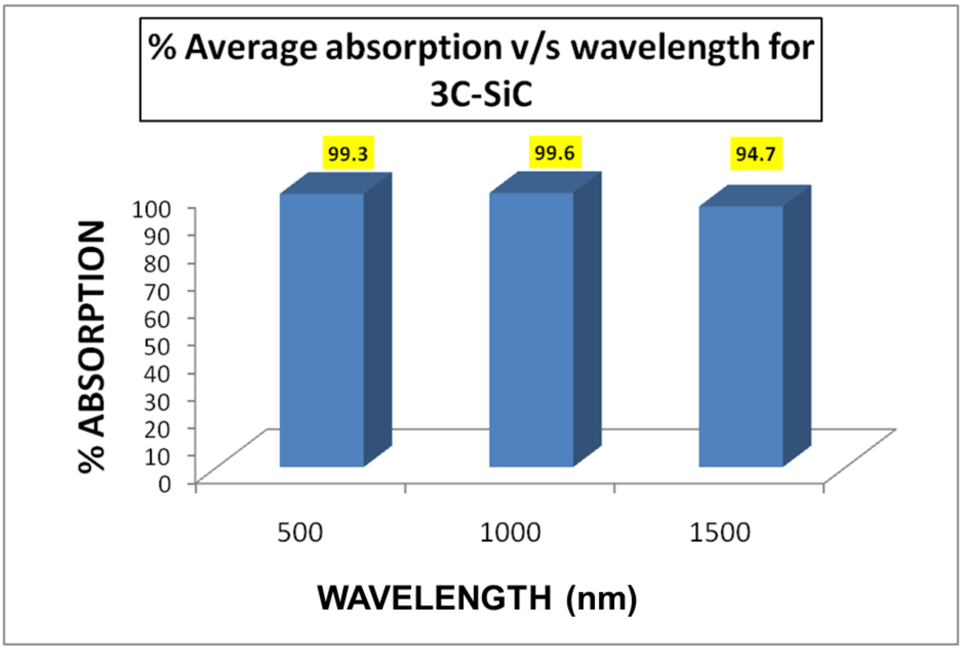

Figure 6.3. Average absorption% versus wavelength for 3C-SiC at normal pressure at a constant depth/thickness of the workpiece material.

6.2.4. Calculations for Silicon Carbide (4H-SiC) at Normal Pressure

Table 6.7. Optical properties of 4H-SiC at normal pressure and varying wavelenghts [148].

Wavelength (nm) ➔	**500**	**1000**	**1500**
n	2.867054	2.767671	2.740438
k	6.53981×10^{-5}	3.01698×10^{-5}	3.04696×10^{-6}
ε_1	7.22	6.66	6.51
ε_2	0.000375	0.000167	0.0000167
α (m^{-1})	1753.77	406.59	19.3874
β	3.377×10^{7}	1.62×10^{7}	1.51×10^{7}
R	0.2331	0.2201	0.2165

Table 6.8. Calculated R%, T% and A% of laser for 4H-SiC at varying depth/thickness of the workpiece material.

Wavelength (nm)	**Thickness (μm)**	**R (%)**	**T (%)**	**A (%)**
500	20	23.31	56.79	19.90
	50	23.31	53.88	22.81
	80	23.31	51.11	25.58
	110	23.31	48.49	28.20
	200	23.31	41.41	35.28
	260	23.31	37.28	39.41
1000	20	22.01	60.33	17.66
	50	22.01	59.60	18.39
	80	22.01	58.87	19.11
	110	22.01	58.16	19.83
	200	22.01	56.07	21.92
	260	22.01	54.72	23.27
1500	20	21.65	61.36	16.99
	50	21.65	61.33	17.02
	80	21.65	61.29	17.06
	110	21.65	61.26	17.09
	200	21.65	61.15	17.20
	260	21.65	61.08	17.27

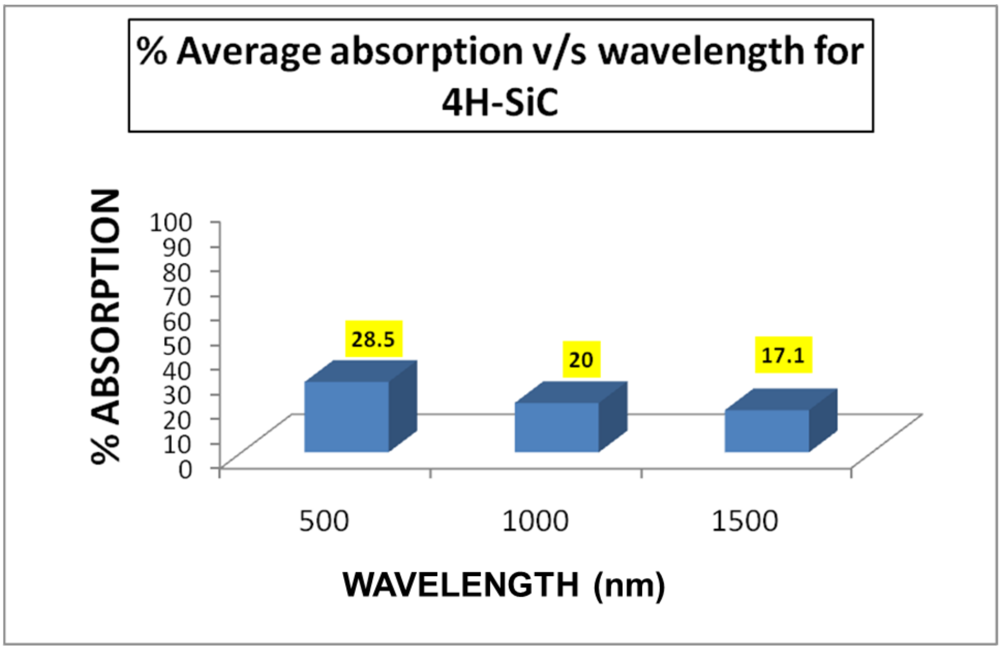

Figure 6.4. Average absorption% versus wavelength for 4H-SiC at normal pressure at a constant depth/thickness of the workpiece material.

6.2.5. Calculations for Silicon Carbide (6H-SiC) at Normal Pressure

Table 6.9. Optical properties of 6H-SiC at normal pressure and varying wavelenghts [149].

Wavelength (nm) ➔	**500**	**1000**	**1500**
n	2.322	2.1374	2.098
k	1.9749×10^{-6}	9.0997×10^{-3}	0.142
ε_1	5.392	4.568	4.4014
ε_2	9.1714×10^{-6}	0.03889	0.0595
α (m^{-1})	49.62	1.144×10^{5}	1.1879×10^{5}
β	2.9179×10^{7}	1.3416×10^{7}	8.787×10^{6}
R	0.1584	0.1314	0.1259

Table 6.10. Calculated R%, T% and A% of laser for 6H-SiC at varying depth/thickness of the workpiece material.

Wavelength (nm)	Thickness (µm)	R (%)	T (%)	A (%)
500	20	15.84	70.77	13.40
	50	15.84	70.66	13.50
	80	15.84	70.56	13.61
	110	15.84	70.45	13.71
	200	15.84	70.14	14.03
	260	15.84	69.93	14.24
1000	20	13.14	7.66	79.20
	50	13.14	0.25	86.61
	80	13.14	0.01	86.85
	110	13.14	0.00	86.86
	200	13.14	0.00	86.86
	260	13.14	0.00	86.86
1500	20	12.59	7.10	80.31
	50	12.59	0.20	87.21
	80	12.59	0.01	87.40
	110	12.59	0.00	87.41
	200	12.59	0.00	87.41
	260	12.59	0.00	87.41

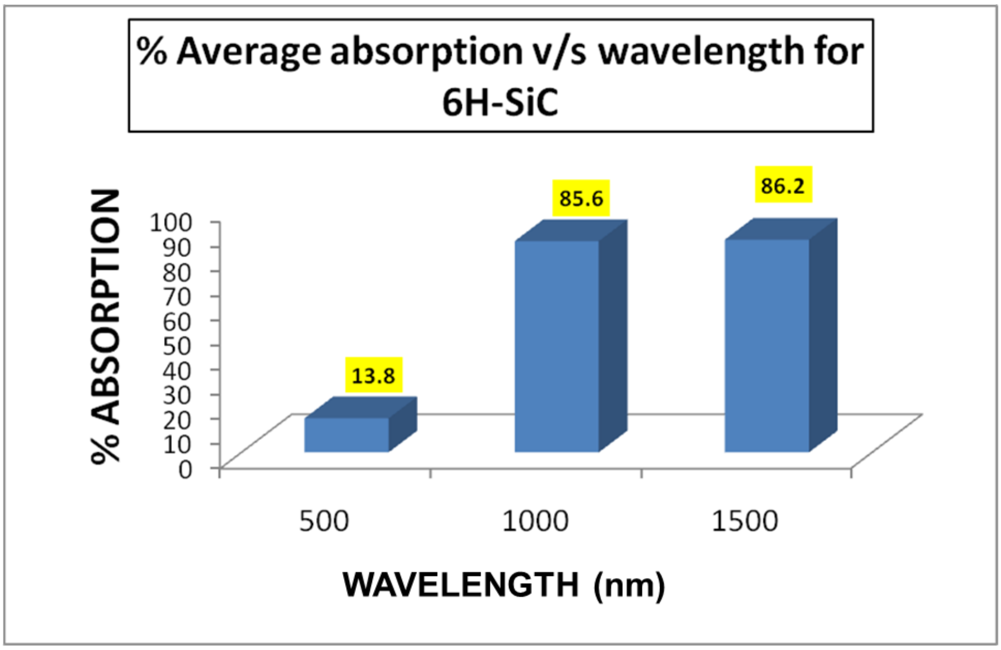

Figure 6.5. Average absorption% versus wavelength for 6H-SiC at normal pressure at a constant depth/thickness of the workpiece material.

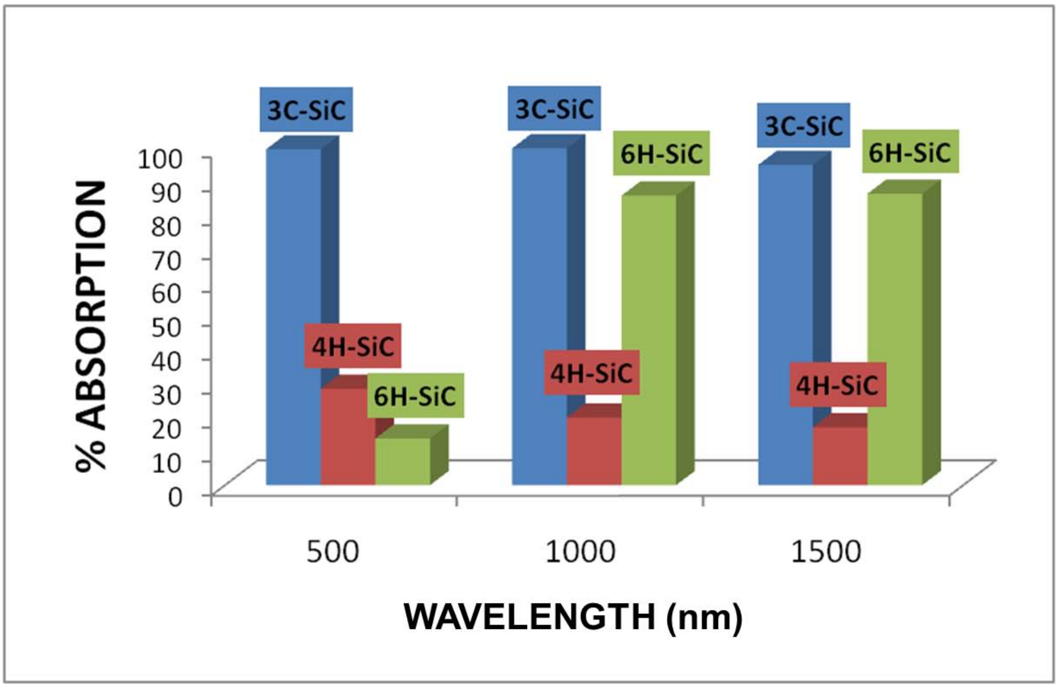

Figure 6.6. Comparing the results of average absorption% versus wavelength for SiC (3C, 4H and 6H) at normal pressure at a constant depth/thickness of the workpiece material.

6.3. Conclusion

- The average absorption% for 1500 nm laser wavelength for Si-II is much higher when compared to Si-I.
  - Si-I has the highest average absorption% at 500 nm wavelength (61%).
  - Si-II has the highest average absorption% at 500 nm wavelength (51%).
  - By applying pressure (13.2 GPa) the average absorption% of Si at 500 nm wavelength drops by 10%.
  - At 1500 nm wavelength, absorption of Si-I is almost zero.

- The average absorption% for 3C-SiC remains high above 95% with throughout the wavelength range from 500 nm to 1500 nm.

- The average absorption% for 4H-SiC decreases slightly with increasing the wavelength from 500 nm to 1500 nm and is generally much lower than the other polytypes (<40%).

- In case of 6H-SiC the absorption% largely depends on wavelength and increases from 14% to 86% on increasing wavelength from 500 nm to 1000 nm. After that it is ~80-90% up to 1500 nm wavelength.

- 3C-SiC has the highest average absorption% (≥95%) at all wavelengths (500, 1000 and 1500 nm) comparing w/ 4H-SiC and 6H-SiC.

High pressure and temperature tests were conducted at US Deparment of Energy (DoE), Argonne National Laboratory (ANL), Advanced Photon Source (APS) to determine the phase transition conditions and parameters of 4H, 6H and 3C SiC. The phase change in these SiC materials was seen over a pressure range of 66 - 88 GPa and at 1500 - 1600 K. It is believed (from preliminary results) that all three polytypes appear to form a dense cubic phase (3C) at these conditions. The data from these experiments is still being analyzed to determine the characteristics of the newly formed high pressure phase, such as optical absorption over the wide range of wavelengths (UV through IR).

The optical properties of SiC (3C, 4H and 6H poly-types) at the high pressure and ambient temperature will be determined by using Diamond-Anvil-Cell (DAC) technique and micro optical system at ANL. The idea of extending this research at Argonne National Laboratory (ANL) is to investigate the optical absorption, transmission and reflection under high pressure on 3C-SiC (β-SiC), 4H-SiC, and 6H-SiC, by using the Diamond-Anvil-Cell (DAC) technique in combination with a micro-optical system for the IR range. The diffraction experiments were done on the interested polytypes of SiC at various pressure and temperatures to get the optimized combination of the P&T and by incorporating laser heating source the optimum wavelength range will be determined as well.

7. THE EFFECT OF THE LASER HEATING AND PRESSURE ON SiC

7.1. Introduction

This chapter discusses the results from scratch tests on a single crystal 4H-SiC wafer with and without laser heating. Since the wafer is a single crystal, the crystal orientation and scratch directions are provided. The main objective of this study is to analyze the cutting forces in the machining process and the material's ductile response during the µ-LAM process. The calculations in this chapter include formulization of the mechanical work, specific energy, absorbed heat by substrate, and estimated hardness of the heated and thermally softened material.

The objective of the study is to determine the effect of temperature and pressure during the µ-LAM of the single crystal 4H-SiC semiconductors using scratch tests. The scratch tests include the examination of the effect of temperature in thermal softening of the high pressure phases formed under the diamond tip. The tests also evaluate the difference with and without irradiation of the laser beam at a constant loading and cutting speed. The laser heating effect is verified by atomic force microscopy (AFM) and white light interferometry measurements of the laser heated scratch grooves.

Scratch tests were chosen to be the principle method in this study. Scratch testing is a better candidate for evaluating machining than indenting because the scratching parameters are more applicable to the machining process, such as depth of cut, width of cut and cutting speed parameters.

7.2. Experimental Procedure

A typical µ-LAM experimental system setup is shown in Figure 7.1 A Universal micro-Tribometer (UMT) from the Center for Tribology Research Inc. (CETR) is used in all the experiments reported in this study. This equipment was developed to perform comprehensive micro-mechanical tests of coatings and materials at the micro scale. This system facilitates the cutting speeds as low as 1µm/sec at nanometric cutting depths. The tribometer is a load controlled device where the required thrust force (F_z) is programmed by the user to obtain the desired depth of cut (DoC); based on the tool geometry and the work piece material properties. The equipment includes a dual-axis load cell that is capable of continuously monitoring and recording the thrust and cutting forces, $F_{x;}$ the latter obtained as an output parameter from the cutting experiment.

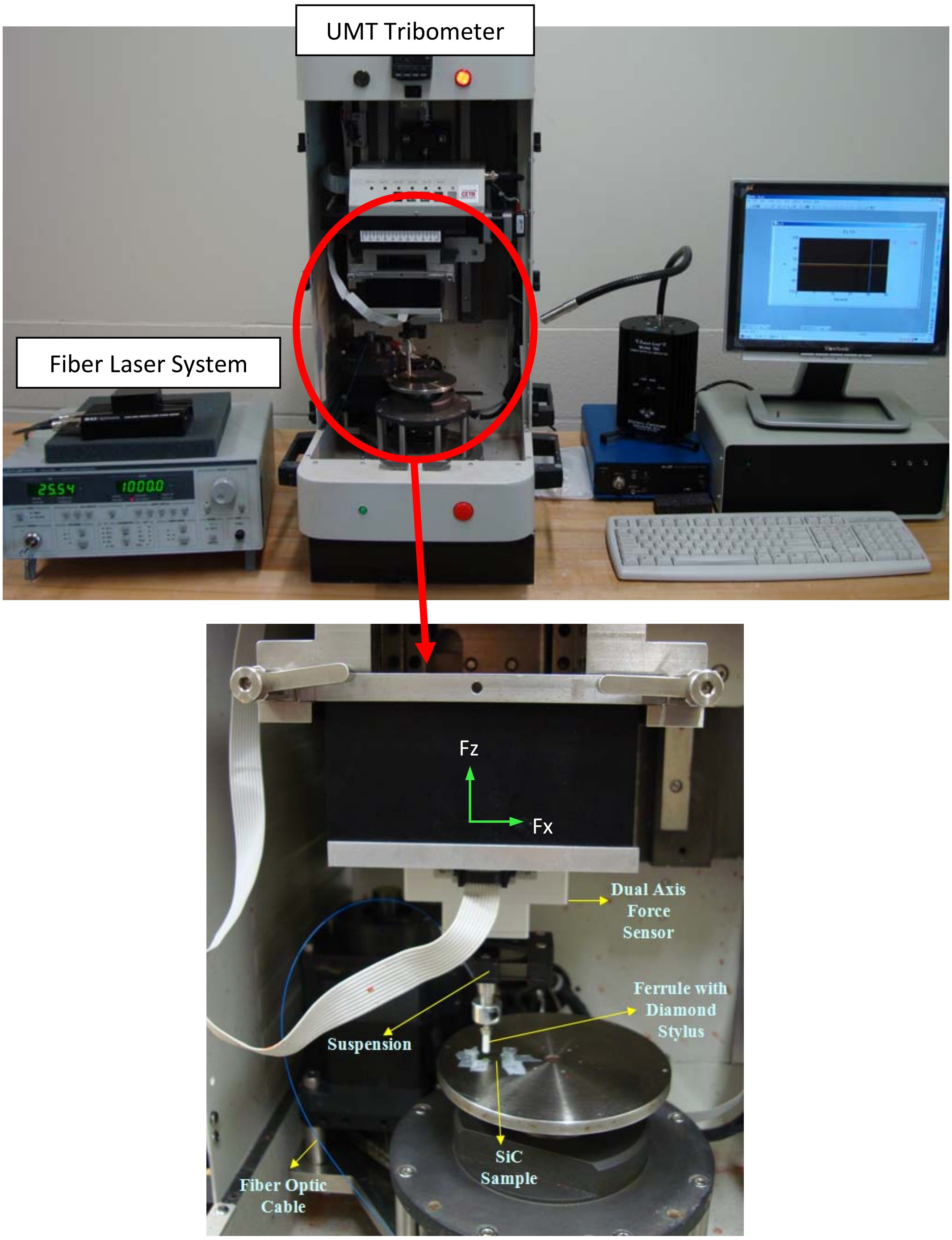

Figure 7.1. µ-LAM system setup on the UMT.

The IR diode laser used in this investigation is a Furukawa IR fiber laser which has a 1480 nm wavelength and a 400mW maximum laser power with a Gaussian profile and beam diameter of 10 µm. The IR laser beam is guided from the diode laser through a 10 µm fiber optic cable to the Zirconia ferrule, which is attached to the diamond stylus. The simple µ-LAM configuration used in the experiments is shown schematically in Figure 7.2.

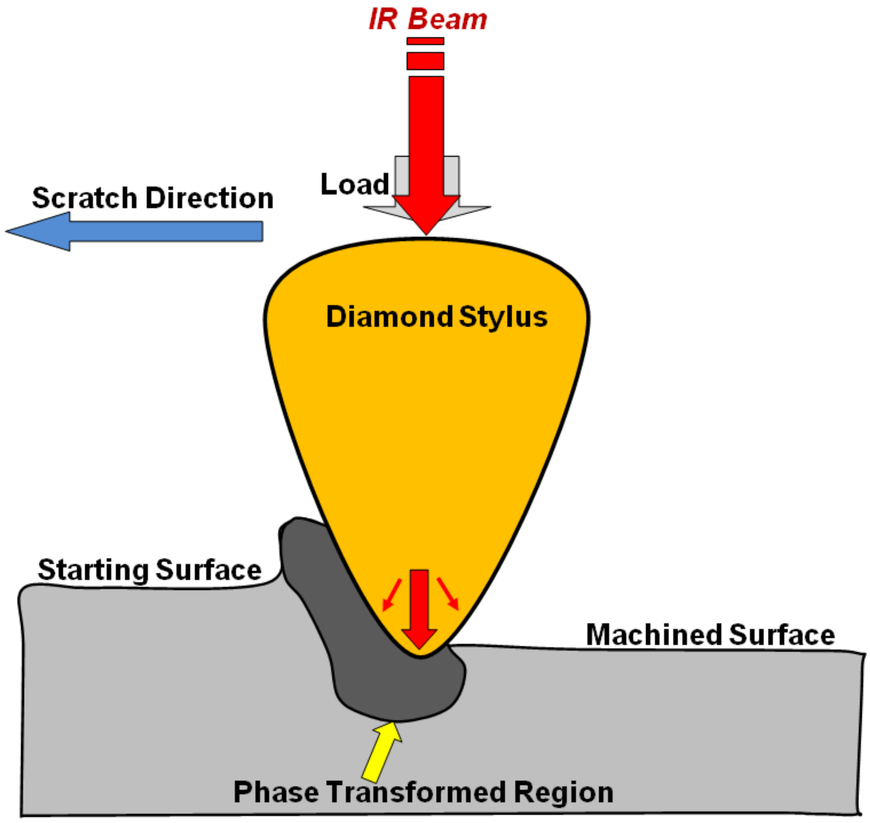

Figure 7.2. A schematic cross-section of the µ-LAM process.

In this setup, the IR laser beam passes through the optically transparent diamond tip (tool) and impinges on the 4H-SiC workpiece material. The µ-LAM system is configured in such a way that the laser beam passes through a 90° conical single crystal diamond tip with 5µm radius spherical end and impinges on the work piece material at the tool work piece interface (contact), as shown in Figure 7.3 (and also shown previously in Chapter 5).

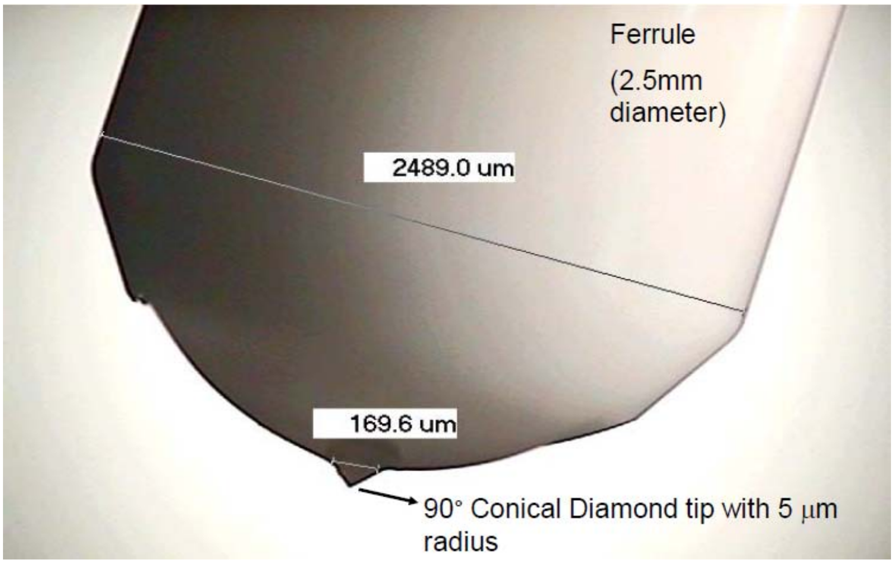

Figure 7.3. 90°conical single crystal diamond tip with 5 μm radius spherical end attached on the end of the ferrule using epoxy.

Single crystal 4H-SiC wafers (provided by Cree Inc., USA) were used in all of the scratch tests. All cuts were performed on the {1010} plane along the <1010> direction.

Scratch tests are chosen to be the principle method used in this study. Scratch testing is a better candidate for evaluating machining compared to indenting because the scratching parameters such as depth of cut, width of cut and cutting speed are more applicable to the machining process. The scratch dimensions and profile mainly depend on the tool geometry and the applied force. However, the depth and width of the scratch and its profile may vary due to absorption of the laser beam energy in the surface region of the substrate. In order to understand the effect of the laser beam on the scratch dimensions, these tests were carried out with and without laser heating during machining.

In this experiment, three scratches were performed with and without laser heating. While one scratch was made with laser heating, the rest of them were carried out without laser heating. The loads used for the scratch tests were 2.5 g (~25 mN), and 7.0 g (~70 mN), with a constant cutting speed of 1 μm/sec. Results obtained from these tests are compared to previously obtained results with a constant cutting speed of 305 μm/sec [150]. Table 7.1 summarizes all the experimental conditions along with the previously reported conditions.

The scratch profile as well as dimensions (width and depth) were examined using a Wyko optical profiler and an Atomic Force Microscope (AFM).

Table 7.1. Scratch parameters.

Scratch No.	Load g (mN)	Machining Condition	Cutting Speed (μm/sec)	Laser Power (mW)
*1**	*2.5 (25)*	*No laser*	*305**	*0*
*2**	*2.5 (25)*	*w/ laser*	*305**	*350***
3	2.5 (25)	No laser	1	0
4	2.5 (25)	w/ laser	1	350**
5	7.0 (70)	No Laser	1	0

**Experiments performed previously [150].*
***350mW is the laser power, approximately 150mW is actually delivered to the work piece material, the balance of the laser power is lost due to scattering and reflections.*

7.3. Results and Discussions

The scratch profiles along with the groove width and depth were measured using an AFM. Figures 7.4 and 7.5 are the AFM profiles that clearly indicate the depth and width of the scratch grooves without and with laser heating at 25 mN applied load using the same cutting speed of 1 μm/sec. These clearly depict laser heating effect of the scratches made on 4H-SiC. The results of all of the scratch tests are presented in the Table 7.2, including the experiments at higher speed of 305μm/sec conducted previously. Figure 7.6 shows the profile of the scratch made with the laser as observed in a Wyko optical profiler. Wyko optical profiler and AFM measurements were found to be in agreement with each other for a given sample.

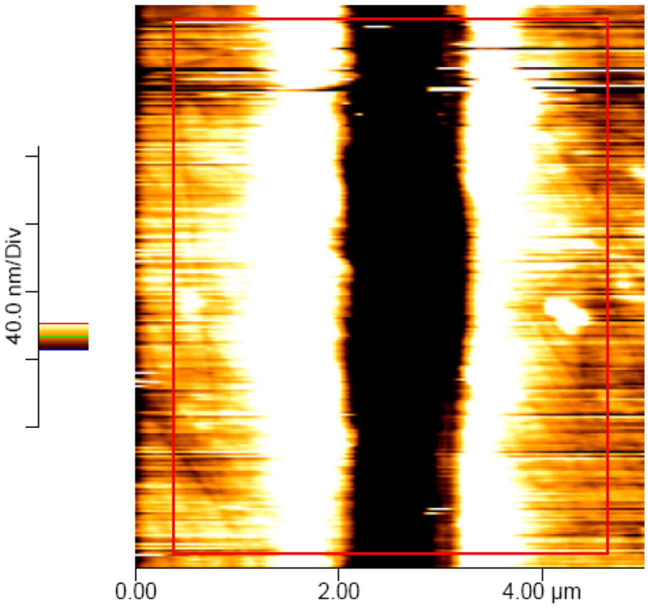

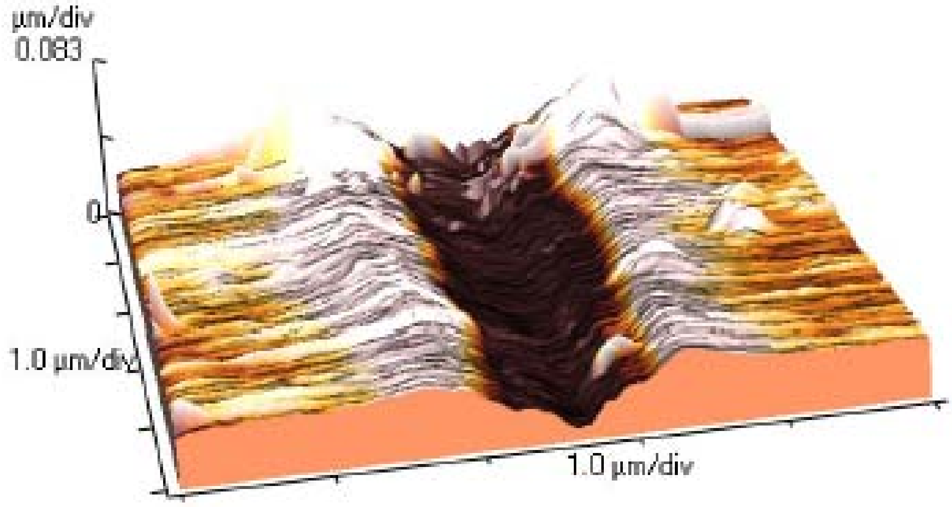

Figure 7.4. AFM image of the scratch#3; no laser heating, 25mN load, 1µm/sec cutting speed.

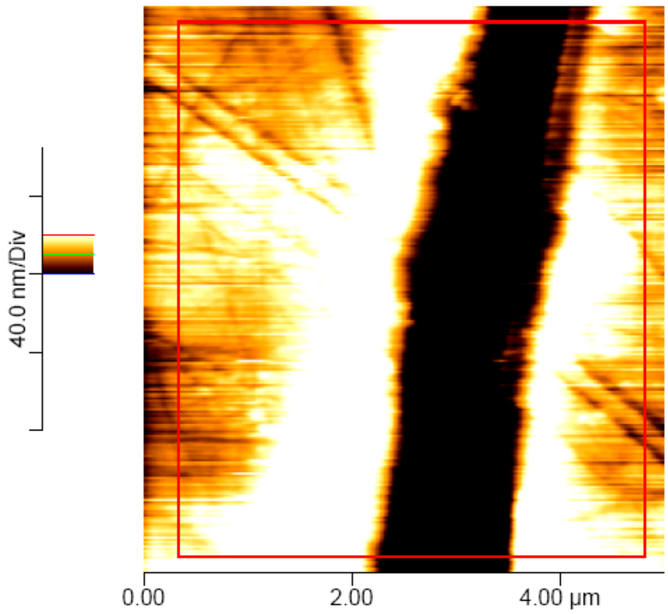

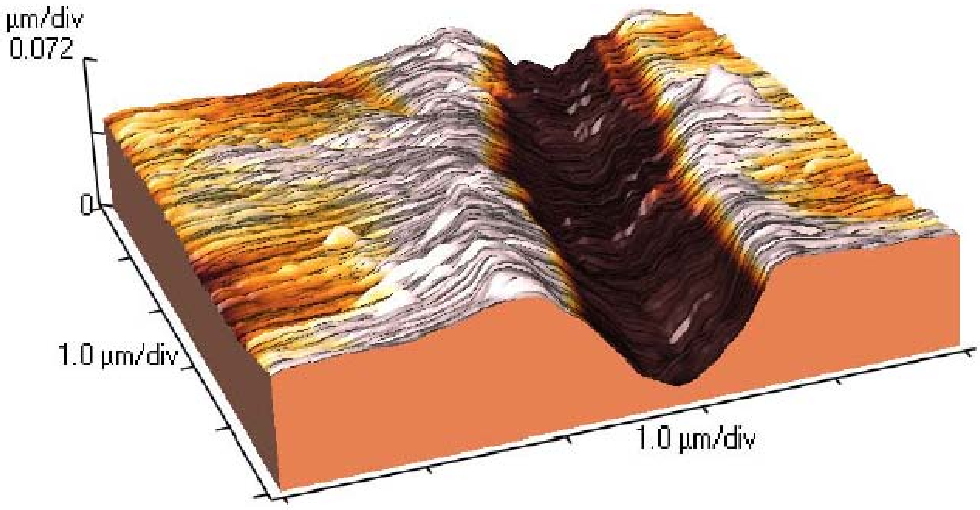

Figure 7.5. AFM image of the scratch#4; w/ laser heating, 25mN load, 1µm/sec cutting speed.

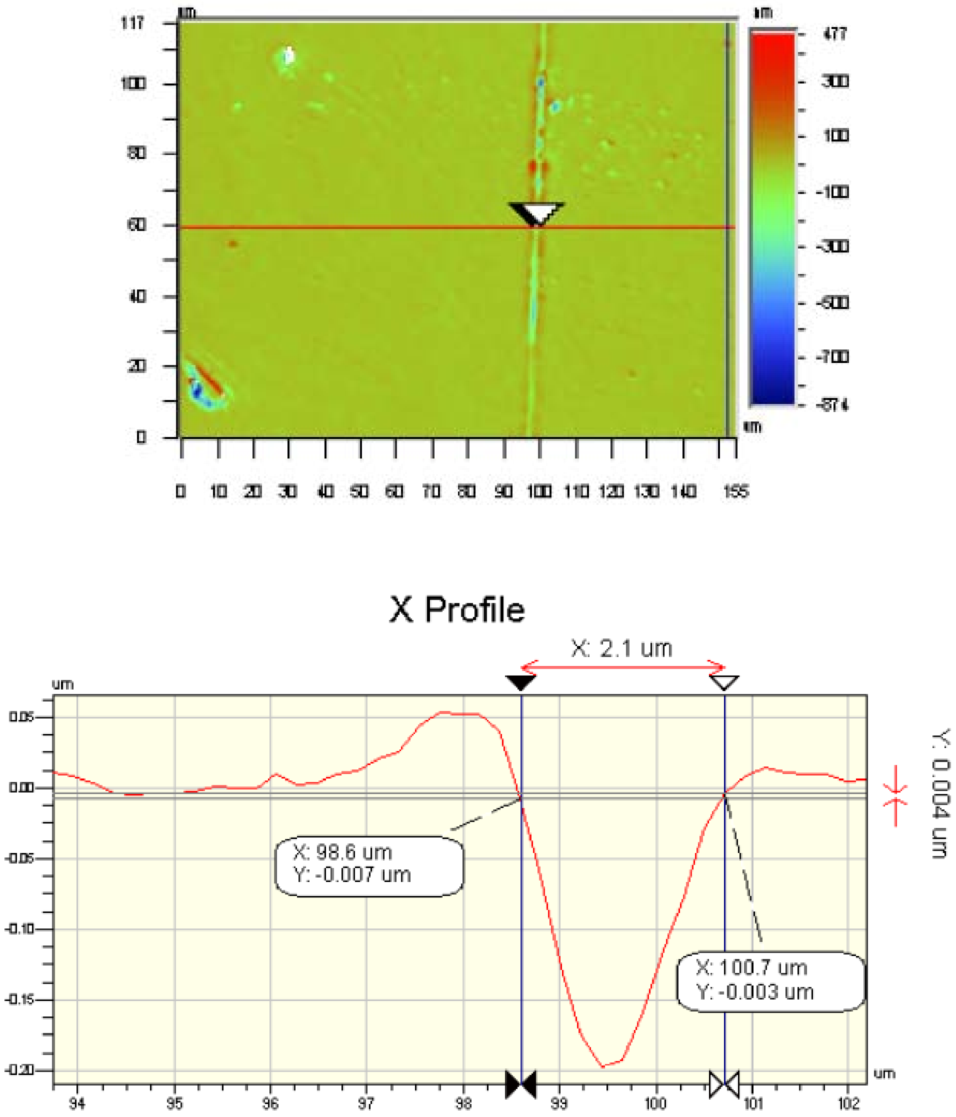

Figure 7.6. Wyko optical interferometer profile of the scratch#4 w/ laser at 1 µm/sec cutting speed.

Table 7.2. Average groove depths measured on AFM.

Scratch#	Load g (mN)	Machining Condition	Cutting Speed (µm/sec)	Average Groove Depth (nm)
*1**	*2.5 (25)*	*No Laser*	*305**	*41*
*2**	*2.5 (25)*	*w/ laser*	*305**	*46*
3	2.5 (25)	No Laser	1	54
4	2.5 (25)	w/ laser	1	90
5	7.0 (70)	No Laser	1	95

**Experiments performed previously [150].*

Apart from the major difference in the cutting speeds, 305µm/sec (experiments performed previously) and low speed 1µm/sec (at WMU), in the two sets of data presented in Table 7.2, there may be minor differences in the test equipment (profilometer and tribometer respectively) used, operator variability, and other test conditions in which the scratches were performed.

The applied load (thrust force, F_z) was kept constant (25mN) throughout the entire experiment enabling the evaluation of heating effects on the material. The high pressure phase, due to the HPPT, of the 4H-SiC occurs within the contact interface as a result of externally applied pressure (>25GPa), is the common phenomenon in all of the scratches made on the 4H-SiC specimen. As the result of heating by the laser beam, the temperature of the surface material adjacent to the diamond stylus rises to achieve the desired thermal softening.

The depth of cut is a crucial parameter and if it exceeds the critical depth (ductile to brittle transition depth), this will shift the ductile regime machining to an unfavorable brittle condition, which is avoided in this study. Hence, care was taken to ensure that there is no brittle mode material deformation during the chosen conditions. As can be seen from the Wyko and AFM images, deformation in all cases was in the ductile mode with no evidence of brittle fracture.

In the previous set of scratches performed at 305µm/sec, the difference in the depth of cut for w/ and w/o laser heating was measureable but not significant, indicating some but not much laser heating and thermal softening. In the current set of scratches with 1µm/sec cutting speed, the depth of cut significantly increased with laser heating, nearly doubled, from 54 (w/o laser heating) to 90nm (with laser heating), see Figure 7.7. This indicates significant laser heating and resultant thermal softening. This result shows that temperature plays a significant role in enhancing the ductile regime machining of 4H-SiC specimen at the cutting speed used in this experiment.

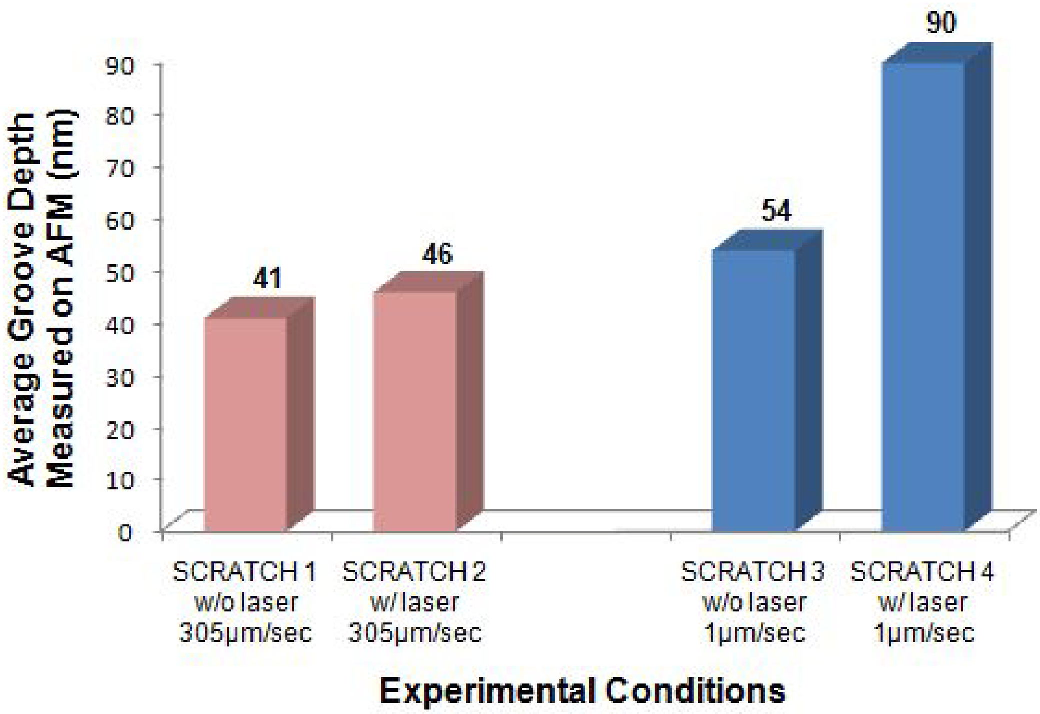

Figure 7.7. Average groove depth measured with AFM in (nm) with two different speeds and w/ and w/o laser.

7.3.1. Force Analysis

The applied normal loads (thrust forces, F_z) were selected to be 25 and 70 mN in the cutting experiments to evaluate the effect of heating on the workpiece. The depth of cut (DoC) and the width (w) of the scratches along with the thrust force (F_z) and cutting force (F_x) of the scratches are summarized in Table 7.3. The depth and width of the scratches were obtained from the AFM and Wyko profiler measurements.

Table 7.3. Scratch test results on 4H-SiC with a cutting speed of 1 μm/sec.

Scratch #	Machining Condition	Thrust Force F_z (mN)	Cutting Force F_x (mN)	Depth of Cut (DoC) (nm)	Width of Scratch (nm)
3	No Laser	25	7.5	54	1.16
4	With Laser	25	8	90	1.25
5	No Laser	70	27.3	95	1.7

In conventional scratch test experiments, the general trend is that the cutting force (F_x) increases as the depth of cut (DoC) is increased. This trend is clearly seen in Table 7.3 where the F_x for all scratches (with and without laser heating) increases as the DoC is increased. This is due to the logical fact that a larger force is needed to mechanically displace and remove more material from a deeper cut. From Table 7.3, it can be also seen that the scratch with laser heating yielded a much lower F_x compared to the other non laser heated scratch at a greater depth. Comparing the 90 nm scratch depth with laser heating and the 95 nm scratch depth without laser heating, it can be seen that the scratch performed without laser heating resulted in more than three times the cutting force compared to the laser heated scratch, for approximately the same depth (DoC). Also, the scratch performed with laser heating produced a deeper groove at about the same amount of cutting force compared to a much smaller depth for the non laser heated scratch test, i.e., comparing the scratches with depths of 54 nm (without laser heating) and 90 nm (with laser heating).

7.3.2. The Formulization of Specific Energy, Relative Hardness, Mechanical Energy and Heat of Scratches

The cross-sectional area of the scratch (A) is approximated as the triangular area as

$$A = \left(\frac{1}{2}\right) w.d \qquad (7.1)$$

where w is the width of scratch, and d is the depth of cut, see Figure 7.8.

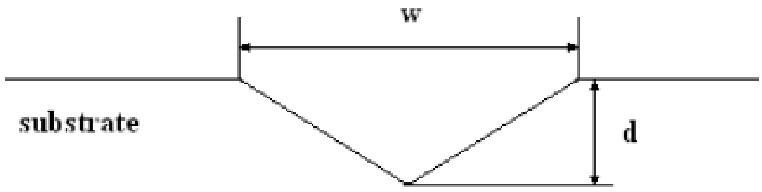

Figure 7.8. Schematic sketch of cross-sectional view of a scratch on the 4H-SiC wafer with the width of cut “w”, and depth of cut “d”.

7.3.2.1. Specific Energy

The Specific Energy is calculated based on cutting force (F_x), and cross-sectional area (A_c) as;

$$E_{spc} = \frac{F_x}{A_c} \tag{7.2}$$

The results of cross-sectional area (mm^2) and specific energy (J/mm^3) calculations for the scratches with and without laser at a constant cutting speed (1 µm/sec) are tabulated in Table 7.4 The area (crescent) calculations are provided in the Appendix. The specific energies of the scratches are plotted versus the depth of cut in Figure 7.9 by calculated crescent area, respectively.

Table 7.4. Specific Energies of the scratches on 4H-SiC (with and without laser), based on the crescent area.

Scratch #	Machining Condition	Thrust Force F_z (mN)	Cutting Force F_x (mN)	Depth of Cut (DoC) (nm)	Calculated Width of Scratch (nm)	Crescent Area, A_c (calculated) (mm^2)	Specific Energy (E_{spc}) (J/mm^3)
3	No Laser	25	7.5	54	1.47	5.28232E-08	142
4	With Laser	25	8	90	1.89	1.13534E-07	70
5	No Laser	70	27.3	95	1.94	1.23107E-07	222

At a constant cutting speed (1 µm/sec) and a constant load (thrust force of 25 mN), specific energy of the scratch with laser heating is calculated to be 70 J/mm^3, almost half the specific energy of the scratch without laser heating at the same conditions.

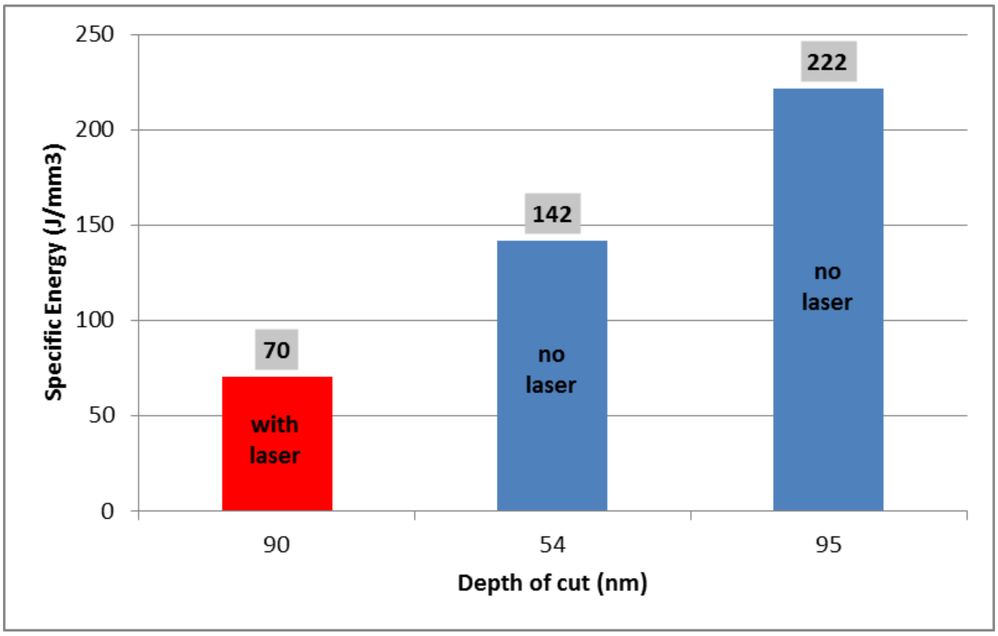

Figure 7.9. Plot of the specific energies of the scratches (with and without laser heating) versus depth of cut.

7.3.2.2. Calculations of Relative Hardness of the Scratches

When calculating the hardness of the scratches (scratch hardness), only one half of the area under the diamond tool "A_d", has been used, Figure 7.10; because of the relief surface of the stylus tool at the trailing edge.

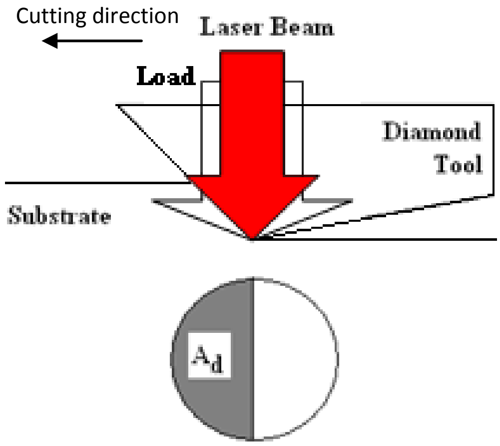

Figure 7.10. The schematic sketch of the indentation on the 4H-SiC, and the indentation area A_d.

The indent area is given by;

$$A_d = \frac{\pi}{2}\left(\frac{w}{2}\right)^2 \quad (7.3)$$

where "w" is the width of scratch, hence the hardness of the scratch "H" in (GPa) is,

$$H = \frac{F_n}{A_d} \quad (7.4)$$

where F_n is the thrust force (F_z). The resulting hardness of the scratches is tabulated in the Table 7.5 and plotted in Figure 7.11.

Table 7.5. Relative Hardness values of the scratches #3 and #4 (with and without laser heating).

Scratch #	**Machining Condition**	**Scratch Area, A_d (μm^2)**	**Thrust Force F_z (mN)**	**Hardness H (GPa)**
3	No Laser	1.69	25	30
4	With Laser	2.81	25	18

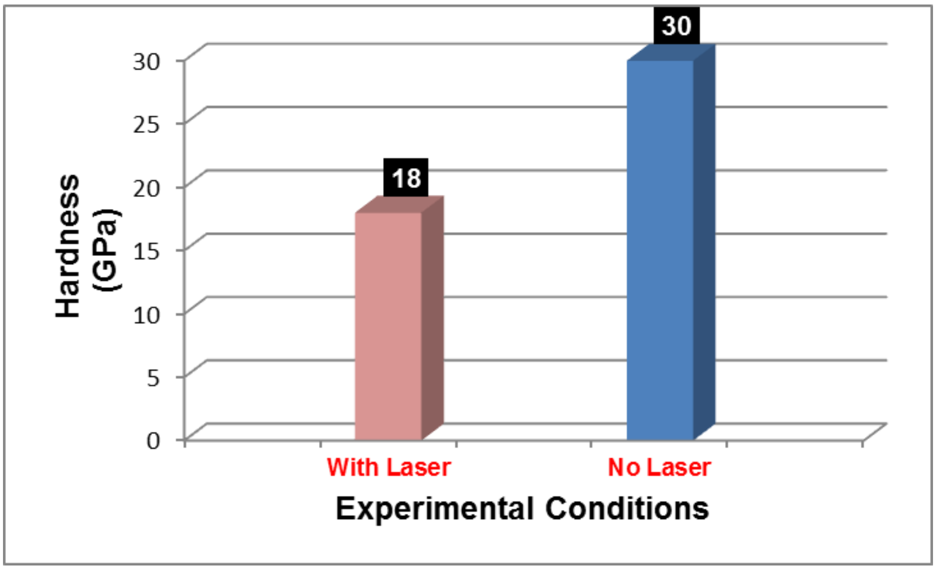

Figure 7.11. Plot of resulting relative calculated hardness of the scratches.

Hardness can be estimated using the measured groove depth and corresponding load. For the case of scratching at a 25 mN load, 1 µm/sec scratching speed and 1000 mA laser driving current which is approx. 350 mW, the calculated hardness is 18 GPa, which corresponds to a temperature of around 700-800 °C [151].

Based upon the scratch (groove) depth and load, the relative hardness of 4H-SiC with laser heating is estimated to be 18 GPa and the relative hardness of the scratch with no laser heating is calculated to be 30 GPa [151]. Estimating the temperature achieved for the laser heated 4H-SiC, based upon published hardness-temperature data [151] suggests a temperature increase of 700-800°C in the scratch #4. At the laser power (350 mW) used in these experiments, (150 mW actually delivered to the work piece surface), significant laser heating is achieved at the low speed, while minimal heating occurred at the higher speed. Thus decreasing the cutting speed increases the thermal softening compared to that observed at higher cutting speed.

7.3.2.3. Mechanical Energy and Heat

Mechanical energy defined as product of the cutting speed and the cutting force (F_x) as

$$E_{mech} = v_c . F_x \quad (7.5)$$

The calculation results of mechanical energy and heat generated by laser beam are summarized in the Table 7.6.

Table 7.6. Scratch test data (with and without laser), mechanical energy and heat calculation.

Scratch #	**Machining Condition**	**Cutting Speed v_c (µm/sec)**	**Cutting Force F_x (mN)**	**Depth of Cut (DoC) (nm)**	**Heat by Laser (nW)**	**Mechanical Energy E_{mech} (nW)**
3	No Laser	1	7.5	54	0	27
4	With Laser	1	8	90	0.16	8

The heat generated in µ-LAM process is more focused and efficient than other LAM machining processes [152]. Scratching crescent area (A_c) has to be computed in order to calculate the laser heating in the 4H-SiC. The width of scratch is calculated based on the radius of cutting tool tip *R*, and depth of cut, (see Appendix), as 1.89 µm.

The scratch (without laser heating) at room temperature takes the mechanical energy of 27nW. The laser heating source generates temperatures of approximately 700°C (based upon the relative hardness calculations and published hardness-temperature data, [151]) at the surface of the workpiece, which results in 0.16 nW heat in the scratching process. Based upon this softening effect of the workpiece material, the mechanical energy of the 90 nm deep cut with laser heating, drops to 8 nW (see Table 7.7). Calculations suggest that by further increasing the temperature of the 4H-SiC to near its melting point, the amount of required mechanical energy reduces to zero and the required heat increases to about 0.82 nW, see Figure 7.12 (see Appendix for the calculations).

Table 7.7. Mechanical Energy and Heat of the 90 nm scratch.

Temperature (^oC)	Mechanical Work (nW)	Heat (nW)
25	27	0
700	8	0.16
3200*	0	0.82

* Melting point.

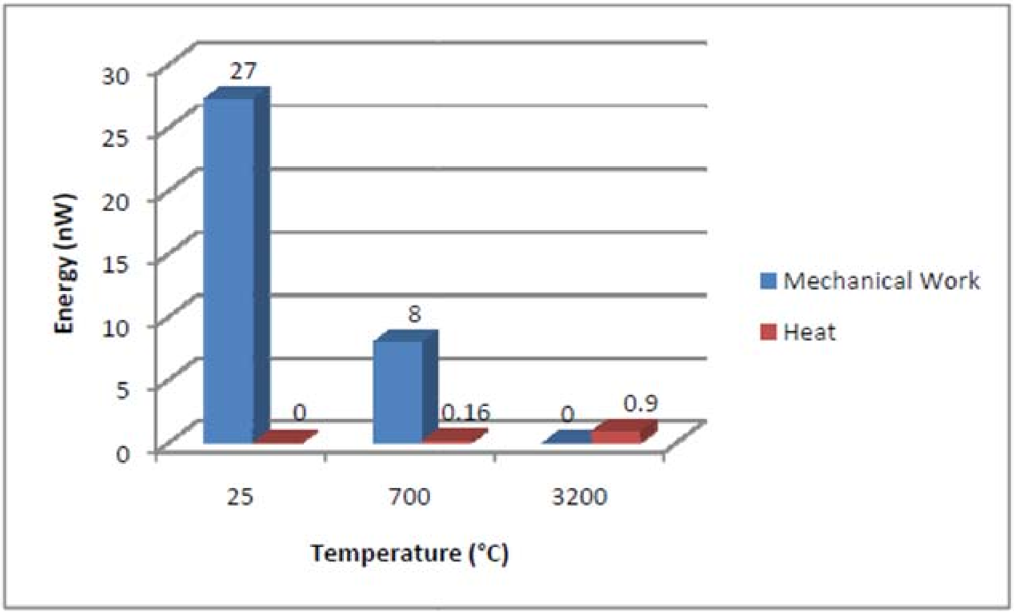

Figure 7.12. Plot of Mechanical Energy and Heat vs. Temperature.

7.4. Conclusion

Laser heating was successfully demonstrated as evidenced by the significant increase in groove depth, i.e., reduced relative calculated hardness, indicative of enhanced thermal softening. AFM and optical profiler measurements of the micro-laser assisted scratch grooves show deeper and wider grooves compared to scratches made without the laser heating assisted methods; which indicates favorable thermal softening effects. Different scratching speeds were tried and the resultant thermal softening effect was found only when the speeds are lower than a certain value, which suggests the following:

1) the total heating time has to exceed a minimum threshold or,

2) the laser power needs to be sufficient enough to provide the requisite heating effect, i.e. the requisite laser energy is a function of time (speed) and power available.

Notably, the results of the scratch tests at a cutting speed of 1µm/sec showed that the depth of cut significantly increased with laser heating, nearly doubled, from 54 (w/o laser heating) to 90nm (with laser heating). By using the laser heating, the amount of mechanical energy required is reduced. The scratch tests performed on 4H-SiC with the laser heating showed that there is almost a 50% reduction in relative calculated hardness values of work piece material (30 GPa to 18 GPa), resulting in a significant reduction in cutting forces (27.3 mN to 8 mN for nearly equivalent depths) and mechanical energy (27 nW to 8 nW). Lesser tool wear is predicted due to the enhanced thermal softening of the material and lower cutting forces during the material removal process.

8. DUCTILE MODE MICRO-LASER ASSISTED MACHINING OF SiC

8.1. Introduction

The objective of the current study is to determine the effect of laser heating (in the μ-LAM process) on the DBT of single crystal 4H-Silicon Carbide (4H-SiC) using scratch testing. The scratch tests were carried out to examine the effect of laser heating and thermal softening of the high pressure phases formed under the diamond tip. Scratch tests were chosen to be the principle material deformation method in this study. Scratch testing is a better candidate for evaluating machining than indenting because the mechanics during scratching are more applicable to the machining process such as single point diamond turning (SPDT). And the scratching parameters are more applicable to the machining process, such as depth of cut, width of cut and cutting parameters, such as cutting force.

There were two studies done from these scratch experiments: studying the laser heating effect on the DBT of the material and evaluating the thermal softening and relative hardness as a result of irradiation and absorption of the laser beam at a constant cutting speed of 1µm/sec. The effect of laser heating was studied by verifying the depths of cuts and evaluating the nature of the scratches (i.e. ductile, DBT or brittle) for diamond tool scratch tests carried out on single crystal 4H-SiC with increasing loads (thrust force, F_z). The load range was selected such that the scratches show both ductile and brittle response (with a DBT region within the scratch). Cutting forces (F_x) and two-dimensional cutting surface profiles were investigated using a white light interferometer.

Finally, laser heating was successful in enhancing the ductile response and decreasing the brittleness of the material resulting in a greater ductile to brittle transition depth. In addition to experimental analysis, numerical simulations were also carried out to study the material behavior of SiC and determine the effect of temperature on the hardness of SiC. The results reported a decrease in cutting forces, thrust forces and pressures at elevated temperature. The FEM software

AdvantEdge, developed by Thirdwave Systems Inc., has been used in these studies [160].

8.2. Experimental Procedure

The scratch tests were performed on a Universal Micro-Tribometer (UMT) which is produced by the Center for Tribology Research Inc. (CETR). This equipment was developed to perform comprehensive micro-mechanical tests of coatings and materials at the micro scale. This system facilitates cutting speeds as low as 1μm/sec at nanometric cutting depths. The tribometer is a load controlled device where the required thrust force (F_z) is programmed by the user to obtain the desired DoC (based on the tool geometry and work piece material properties). The equipment includes a dual-axis load cell that is capable of continuously monitoring and recording the thrust forces (F_z) and cutting forces, F_x, (obtained as an output parameter from the cutting experiment).

A typical scratch test setup along with the μ-LAM system was shown previously in Figure 7.1. All scratch tests were performed on a single crystal 4H-SiC wafer, which was provided from Cree Inc., USA [140]. All cuts were performed on the {1010} plane along the <1010> direction. The primary flat of the SiC wafer is the {1010} plane with the flat face parallel to the <1120> direction. The primary flat is oriented such that the chord is parallel with a specified low index crystal plane.

A 90^o conical single crystal diamond stylus (with a spherical end tip radius of 5μm) was used as the scratch tool. The details of the diamond tip attachment are depicted previously in Chapter 5. An infrared (IR) diode fiber laser (λ=1480nm and P_{max}=400mW) with a Gaussian profile and a beam diameter of ~10μm was used in this study. The laser beam is guided through a 10μm fiber optic cable to the ferrule, which is attached to the diamond stylus. The μ-LAM system is configured in such a way that the laser beam passes through the diamond tip and impinges on the work piece material at the tool work piece interface.

In this study, two conditions of scratches were performed: with and without laser heating.

The scratches were carried out at low cutting speeds (1 µm/sec) in order to maximize the thermal softening of the material during the laser heating. Scratch lengths of 500 µm were produced on the SiC wafer specimen. The loads were increased linearly with time from 2 mN to 70 mN along the scratch. This particular load range was chosen as it would exhibit a ductile, DBT and brittle region. The scratch test parameters are summarized in Table 8.1.

Table 8.1. Parameters for the DBT tests on SiC.

Scratch #	Load Range (mN)	Machining Condition	Cutting Speed (µm/sec)	Laser Power (mW)
1	2-70	no laser	1	0
2	2-70	with laser	1	350*

**350mW is the laser power, approximately 150mW is actually delivered to the work piece material, the balance of the laser power is lost due to scattering and reflections.*

8.3. Results and Discussions

Figure 8.1 and Figure 8.2 shows two scratches, without (scratch 1) and with laser heating (scratch 2). The load range (2-70 mN) performed on these scratches was ideal for this study as it had both the ductile and brittle regime along the same scratch. The DBT is identified somewhere between the ductile and brittle regime of the scratch using optical microscopy, white light interferometry and force analysis (from variations in cutting forces). The onset of brittle fracture for both scratch conditions can be observed from the micrograph. It is seen in Figure 8.1 that the scratch performed without laser heating exhibits brittle fracture along the cut before, i.e., at a shallower depth, than the scratch performed with laser heating. In other words, from the image, it is evident that fracture occurs earlier (at a less load) for the scratch performed with no laser heating. The point of initial fracture can also be correlated to the force data where instability is first observed. The scratches with laser heating are also deeper at the same load or at the same position (x direction) along the scratch.

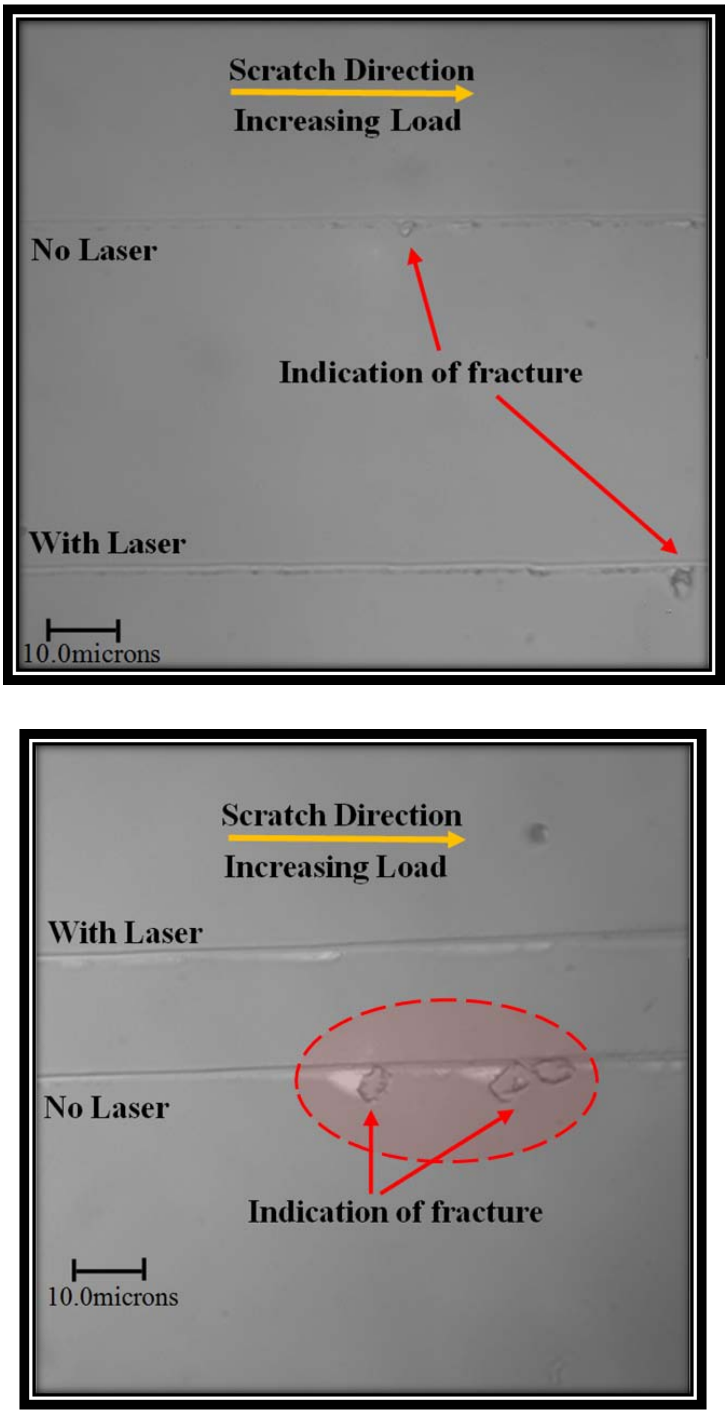

Figure 8.1. Micrographs showing brittle fracture of SiC along the scratch.

The micrographs seen in Figure 8.2 shows both scratch conditions (with and without laser heating) in the brittle region. Although both scratches are with the same load range, the extent of brittle fracture is much more severe for the scratch performed with no laser heating. And again the scratches with laser heating are much deeper at the same load, i.e., the same x position along the respective scratches.

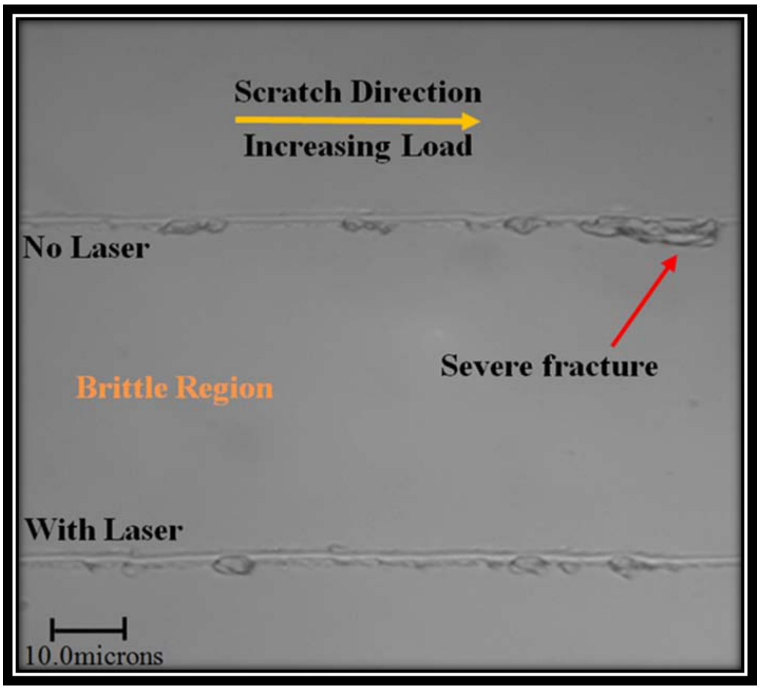

Figure 8.2. Micrograph showing scratches into brittle region at higher loads.

In this study, there were two different analyses done based on the results obtained from the scratch tests. The first analysis compares the depth and cutting forces (F_x) for a constant thrust force (F_z) for both cutting conditions (with and without laser heating) to determine the effect of laser heating and thermal softening on the material. For this analysis, scratches analyzed for both conditions were in the ductile regime. The results summarized in Table 8.2 show that for the same amount of applied thrust force (F_z = 30 mN), the scratch performed with laser heating yielded a greater depth of cut (145 nm vs. 95 nm). It is also evident that cutting forces were equal for both these conditions for an equal applied thrust force (although the scratch performed with laser heating was significantly deeper).

A scratch without laser heating at higher loads resulted in a depth of 145 nm will most definitely result in higher cutting forces due to the (higher) hardness of the unheated material.

The subsequent analysis investigated the effects of laser heating on the DBT of the material. To determine this, two-dimensional scratch/groove profiles obtained using a white light interferometric profilometer were analyzed. Figure 8.3 shows the cross-section of the two scratches taken at an equal thrust force of approximately 35 mN. It can be seen that the scratch performed with laser heating (left) exhibits a perfectly ductile behavior whereas the scratch without laser heating (right) indicates slight fracture (brittle behavior) of the material. The DBT depth identified for the scratch without laser heating just before the point of fracture is approximately 105 nm. The brittle behavior is identified by the imperfect pattern of the groove edge which is a representation of the stylus imprint on the material. It is important to note from Figure 8.3, that the scratch performed without laser heating is (apparently) deeper (210 nm vs. 113 nm) as it is difficult to control the depth when the material removal mechanism is brittle (i.e. difficult to control the depth due to fracture of the material). The clear and defined edges that depict the stylus imprint are a good indication of ductile response of the material (as seen in the scratch performed with laser heating).

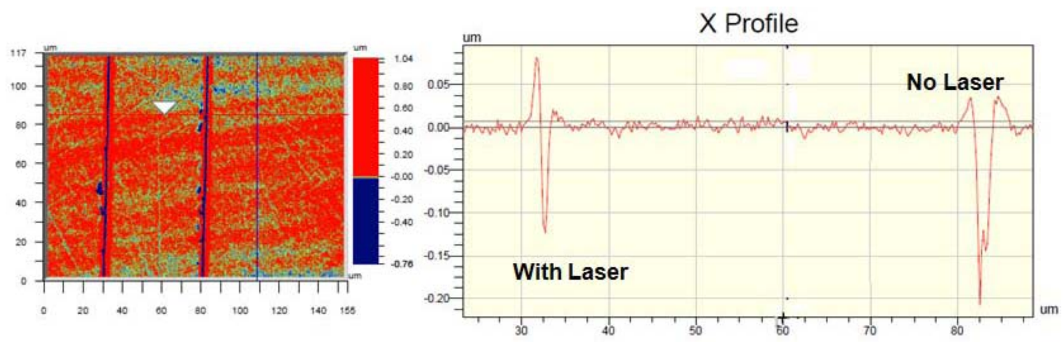

Figure 8.3. Cross-section of SiC scratches (with and without laser heating) obtained from a white light interferometric profilometer showing the onset of brittle behavior for the cut with no laser.

Figure 8.4 shows the cross-section of the same scratches at a different point taken at an equal thrust force of approximately 40 mN. The DBT depth identified for the scratch performed with laser heating just before the point of fracture is approximately 240 nm. At this load, the scratch performed with no laser heating shows signs of severe fracture. In comparison, the DBT depth of the scratch performed without laser heating was approximately 105 nm greater (less that half as deep) than the DBT depth of the scratch performed without laser heating.

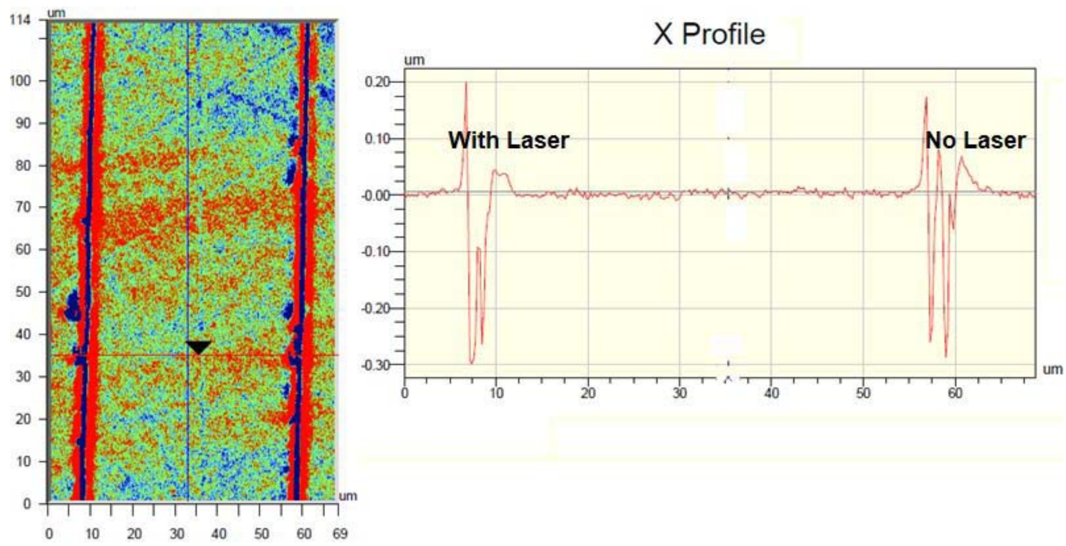

Figure 8.4. Cross-section of SiC scratches (with and without laser heating) obtained from a white light interferometric profilometer showing the onset of brittle behavior for the cut with laser heating.

From Table 8.2, it is seen that the cut performed with laser heating yields a slightly higher cutting force at the DBT. This is due to the higher thrust force (40mN vs. 35mN) and larger depth of cut (240nm vs. 105nm). The effect of laser heating on the DBT depth in SiC is also seen from Figure 8.5.

Table 8.2. SiC scratch test results.

Machining Condition	Thrust Force, F_z (mN)	Cutting Force, F_x (mN)	Depth of Cut (nm)	Scratch Nature
No Laser	30	10	95	Ductile
With Laser	30	10	145	Ductile
No Laser	35	12*	***105****	DBT
With Laser	40	14*	***240****	DBT

**Measurement taken just before the DBT occurs.*

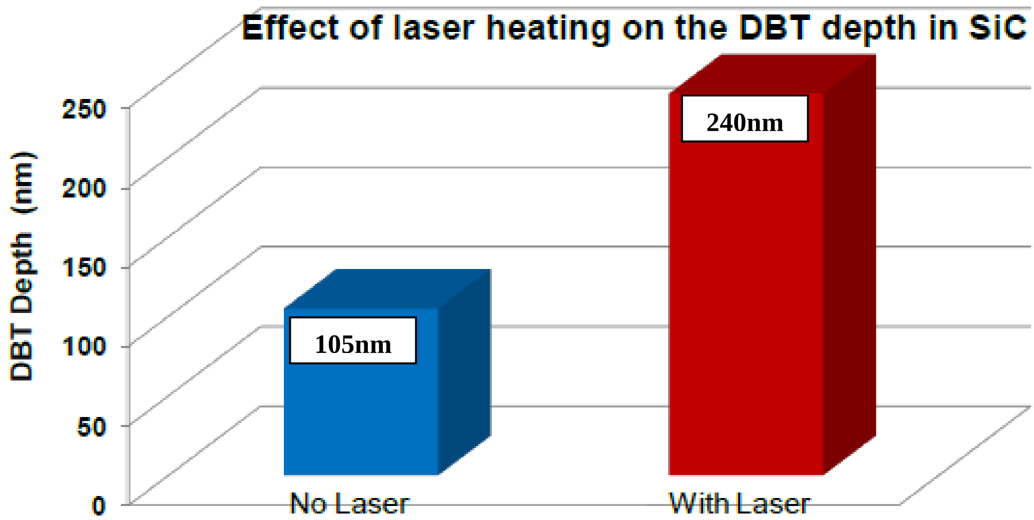

Figure 8.5. The effect of laser heating on the DBT depth in SiC.

Analyzing the force data after the scratch experiments helps in correlating the onset of brittle fracture along the scratches. Brittle mode material removal is usually seen in the force data (especially the cutting forces as they are more sensitive to brittle fracture) and can be identified by its unstable behavior (higher standard deviation/higher peak-valleys in the force plots). Figure 8.6 represents the force data plot obtained from both scratching conditions (with and without laser heating) showing cutting force (F_x) and thrust force (F_z) data for both SiC scratches. It can be seen from the Figure 8.6 that the onset of brittle fracture is identified on the scratch performed with no laser heating. Monitoring the cutting forces (F_x) during the material removal process is also an effective in-situ method to detect the onset of brittle regime machining (onset of fracture occurance).

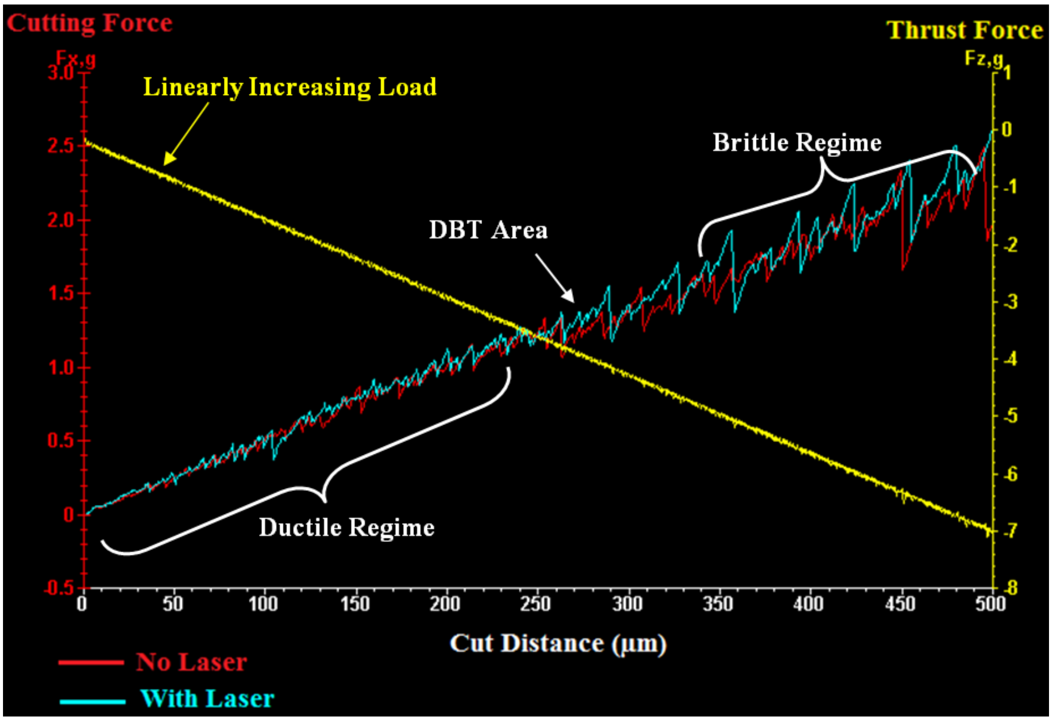

Figure 8.6. Graph showing force data (cutting forces and thrust forces) for both scratch conditions.

8.4. Simulating the Effects of Thermal Softening on Ductile Mode Machining of SiC

In the simulation model, to reflect the ductile behavior in ceramics promoted by the HPPT, a pressure sensitive Drucker-Prager constitutive model is used [153]. A realistic thermal softening curve was developed based on various references to study the thermal softening behavior of SiC [154-158], as shown in Figure 8.7.

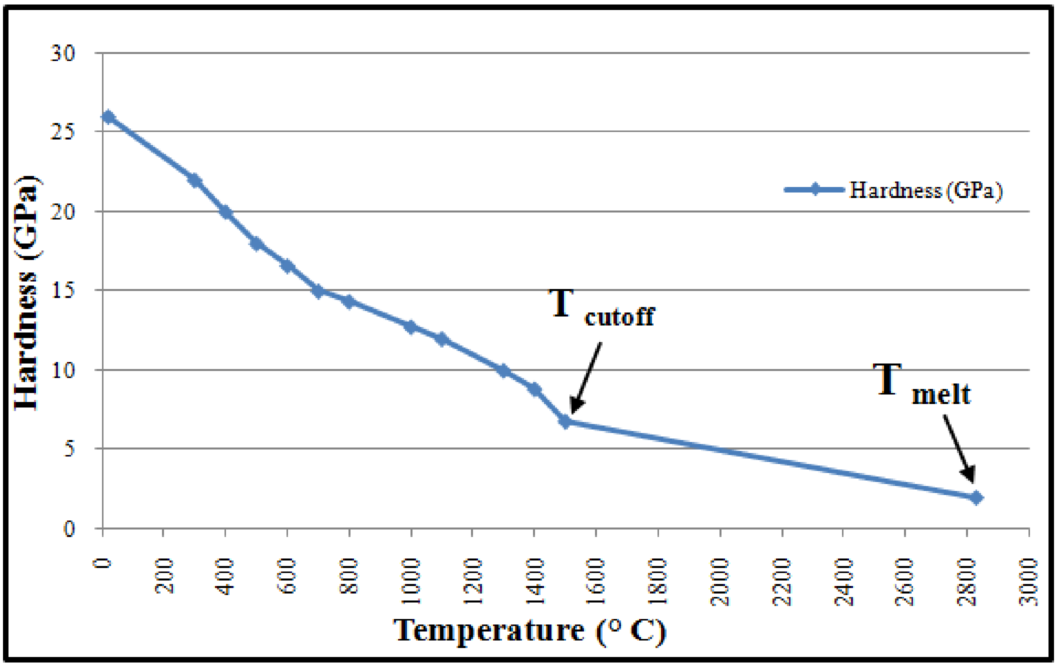

Figure 8.7. Thermal softening (Hardness vs. Temperature) curve based on references.

**The temperature values T_{cutoff} and T_{melt} are estimated based on different values from various references [140, 154-159].*

Figure 8.7. shows the variation of hardness with temperature, which was plotted based on the data points obtained from literature. The curve shows two important points with respect to the temperature, the thermal cutoff point and melting point, which were identified at 1500°C and 2830°C respectively. The curve was obtained through applying a third order polynomial fit up to thermal softening temperature. It may be noted that no data is available (in the literature) for the high pressure phase beyond the thermal cutoff point (1500° C). A boundary condition was defined on the workpiece top surface to mimic the actual heating effect during the μ-LAM process [160]. The change in cutting and thrust forces, and cutting pressures were studied.

8.4.1. Results and Discussions

The simulation results include the cutting and thrust forces that are used for comparison to evaluate the various machining conditions (primarily the workpiece temperature and the resultant thermal softening effect). The feed is 500 nm and cutting edge radius on tool is 100 nm [160]. The simulations were carried out at various temperatures: 20° C, 700° C, 1500° C, 2200° C, and 2700° C, where 1500º C is the thermal cutoff temperature as shown in Figure 8.7. Beyond the thermal cutoff temperature, there is a linear decrease in the material strength until it reaches the melting point (2830° C).

The results at different temperatures are tabulated in Table 8.3. The simulations are run until the forces reach the steady state value, which does not necessarily cover the entire length of cut. The length of cut is selected such that the steady state is achieved before the tool runs through the entire length of workpiece.

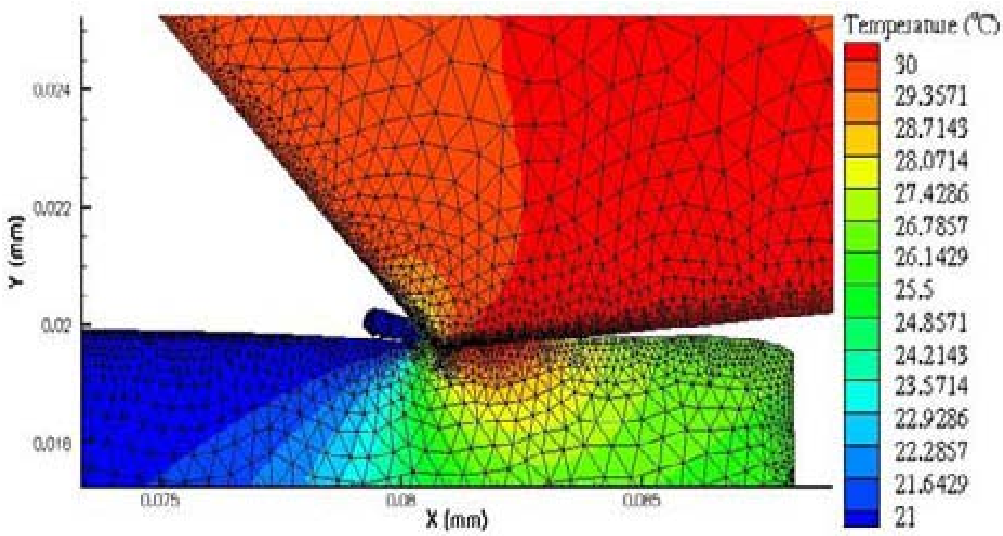

Figure 8.8. SiC micro-laser assisted machining simulation screenshot at 20° C.

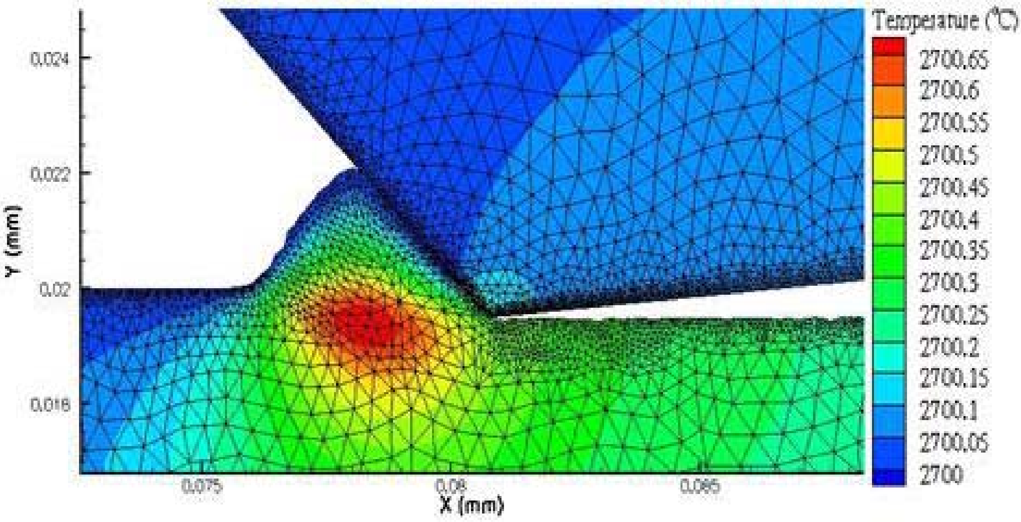

Figure 8.9. SiC micro-laser assisted machining simulation screenshot at 2700° C.

Note that the temperature scale is different in Figures 8.8 and 8.9. At 20° C, there is a significant chip formation and also the cutting pressure is high, as SiC retains it's hardness at room temperature (Figure 8.8). At 2700° C, the hardness of the material is negligible and the material is simply ploughed by the tool (Figure 8.9).

Table 8.3. Summary of the simulation results for the machining of SiC.

Boundary Condition	Temp. (° C)	Fx (mN)	Fz (mN)	Pressure (GPa)
Workpiece top surface	20	470	1040	47
	700	450	950	45
	1500	390	570	39
	2200	200	260	20
	2700	30	40	3

Table 8.3 clearly shows that the cutting and thrust forces (F_x and F_z respectively), and pressures are decreasing with an increase in temperature. This confirms the ability of the machining simulation software to model the thermal softening behavior due to laser heating, which reduces the hardness of the material.

8.5. Conclusion

Micro-laser assisted scratch tests were successful in demonstrating the enhanced thermal softening of the material resulting in a greater ductile to brittle transition depth, i.e., decreased brittleness. Laser heating was successfully demonstrated as evidenced by the significant increase in the ductile response of single crystal 4H-Silicon Carbide in the {1010} plane along the <1010> direction. Laser assisted (heating, thermal softening and reduced brittleness) material removal resulted in a greater depths of cuts at less applied thrust forces, smaller cutting forces and a larger critical DoC.

Force analysis (thrust and cutting), optical microscopy and white light interferometric profilometry served as useful analyses methods to detect the enhanced ductile response and reduced brittle fracture as a result of preferential material heating (of the high pressure phase transformed material). Results obtained from this study are promising to further implement micro-laser assisted machining (μ-LAM) in operations such as single point diamond turning. Lower cutting forces obtained from the μ-LAM process are favorable to minimize tool wear while machining abrasive ceramics/semiconductors such as Quartz, Silicon and Silicon Carbide.

The results from this study also will benefit the manufacture of brittle materials as laser heating is proven to decrease the brittle response in ceramics and semiconductors, which can result in high productivity rates (i.e. higher material removal rate). A similar analysis to study the effects on laser heating on other semiconductors/ceramics (i.e. Spinel, AlTiC, AlON and Sapphire) will be researched in the future.

For the simulation study, the boundary condition chosen successfully simulated the laser heating effect. The thermal softening effect begins above room temperature (20° C) as the hardness of the material decreases with an increase in temperature. Furthermore, the simulation results can be used to study behavior of the high pressure phase beyond the thermal cut-off point.

9. DUCTILE MODE MICRO-LASER ASSISTED MACHINING OF Si

9.1. Introduction

Among the various pressure-induced phase transformations in silicon (Si), the transformation from the diamond crystal structure to the metallic β-tin crystal structure at ~12 GPa is emphasized throughout this part of the study. This particular HPPT occurs during mechanical loading and can be achieved experimentally at relatively low forces (mN), provided that the contact area is very small (μm^2).

It has been established that silicon undergoes a Si-I to Si-II (covalent diamond cubic to metallic (β-tin)) phase transformation under a pressure of around 12GPa, i.e. this is a pressure approximately equal to the hardness of silicon [161]. This high pressure Si-II metallic phase is presumed to result in a reduced transmission of radiation at IR wavelengths, i.e. one of the characteristic properties of a metal is its opaqueness to IR radiation. By properly choosing a laser source, at a proper wavelength that is transparent to covalent silicon, the transformed metallic Si, having optical properties similar to a metal, is expected to block and partially absorb the laser energy. Thus the potential exists for possibly heating the high pressure metallic phase of Si, without affecting the bulk covalent Si. This preferential heating and resultant thermal softening will assist with plastic deformation and material removal in a ductile manner, such as in a scratching or machining process. HPPT (Si-II) is responsible to achieve the ductile response (even without laser heating).

The objective of the current study is to determine the effect of laser heating on the DBT of single crystal Silicon (Si) using scratch testing. Scratch tests were chosen to be the principle material removal method in this study. Scratch testing is a better candidate for evaluating machining than indenting because the scratching parameters are more applicable to the machining process, such as depth of cut, width of cut, cutting speed parameters, and cutting force.

In this study, two different diamond tools were used in the experiments. The scratch tests were carried out to examine the effect of temperature in thermal softening of the high pressure phases formed under the diamond tip. These scratch tests were also used to evaluate the difference between conditions "with" and "without" irradiation of the laser beam at a constant loading (constant thrust force, F_z) and constant cutting speed of 1µm/sec. The effects of laser heating were studied by verifying the depths of cuts for scratch tests carried out on single crystal Si with increasing loads (thrust force, F_z) to make sure the scratch shows both ductile and brittle response (with a DBT region within the scratch). The load range was selected such that the scratches show both ductile and brittle response (with a DBT region within the scratch). Cutting forces (F_x), two-dimensional and also three-dimensional cutting profiles (using a white light interferometer) were investigated. A laser micro-Raman spectrometer (Renishaw inVia Reflex Micro-Raman Spectrograph) was used to characterize the material structural changes. Scanning electron microscope (SEM) was also used to investigate the morphology of the chips formed from Si machining. SEM studies have shown the ductile chip formation.

Laser heating was successful in enhancing the ductile response (achieving thermal softening and concominant reduced cutting forces) and decreasing the brittleness of the material resulting in a greater ductile to brittle transition depth.

9.2. Experimental Procedure

The scratch tests were performed on a Universal Micro-Tribometer (UMT) which is produced by the Center for Tribology Research Inc. (CETR). This equipment was developed to perform comprehensive micro-mechanical tests of coatings and materials at the micro scale. This system facilitates the cutting speeds as low as 1µm/sec at nanometric cutting depths. The tribometer is a load controlled device where the required thrust force (F_z) is programmed by the user to obtain the desired DoC (based on the tool geometry and work piece material properties). The equipment includes a dual-axis load cell that is capable of continuously monitoring and recording the thrust forces (F_z) and cutting forces, F_x, (obtained as an output parameter from the cutting experiment).

A typical scratch test setup along with the μ-LAM system was shown in previous chapters. All scratch tests were performed on a single Si wafer which is provided from UniversityWafer [141]. For the DBT scratch tests on Si, all cuts were performed on the {100} plane along the <110> direction.

An infrared (IR) diode fiber laser (λ=1480nm and P_{max}=400mW) with a Gaussian profile with a beam diameter of ~10μm was used in this study. The laser beam is guided through a 10μm fiber optic cable to the ferrule, which is attached to the diamond stylus. The μ-LAM system is configured in such a way that the laser beam passes through the diamond tool and impinges on the work piece material at the tool work piece interface (contact).

In this study, two conditions of scratches were performed: with and without laser heating.

9.2.1. Experiments with 5μm Tip Radius Diamond Stylus Tool

In this part of the study, a 90° conical single crystal diamond tool (with a spherical end tip radius of 5μm) was used which is shown in previous chapters. The details of the diamond tip attachment are depicted previously in Chapter 5. The laser emerges from the diamond tip's spherical end. The μ-LAM system setup for the 5μm tip radius diamond tool was shown in previosly.

Scratch tests were performed with and without laser heating The scratches were carried out at low cutting speeds (1 μm/sec) in order to maximize the thermal softening of the material during the laser heating. Scratch lengths of 500 μm were produced on the Si wafer. The loads were increased linearly with time from 20 mN to 70 mN along the 500 μm scratch length. This particular load range was chosen as it would exhibit a ductile, DBT and brittle region. The scratch test parameters are summarized in Table 9.1.

Table 9.1. Parameters used for the DBT tests on Si with 5µm tip radius diamond tool setup.

Scratch #	Load Range (mN)	Machining Condition	Cutting Speed (µm/sec)	Laser Power (mW)
1	20-70	no laser	1	0
2	20-70	with laser	1	350*

**350mW is the laser power, approximately 150mW is actually delivered to the work piece material, the balance of the laser power is lost due to scattering and reflections.*

After scratch tests, micro-Raman spectroscopy examinations of the material within the scratch impressions along with the machining chips are carried out to identify any possible phase transformations that may have occurred during the machining with and without laser heating. The laser micro-Raman spectrometer, explained in detail in Chapter 2, was used to acquire Raman spectra to characterize the crystal structure of the deformed material at the bottom of the groove.

9.2.2. Experiments with 1.4mm Nose Radius Diamond Cutting Tool

9.2.2.1. Tool Geometry

In this experiment, a single crystal diamond tool with a 1.4mm nose radius, -45 degree rake angle and 5 degree clearance angle was used. Illustration of the diamond cutting tool provided from Adamant Kogyo Co., Ltd. (Japan) is shown in Figure 9.1 below. The lens fiber was adjusted to locate the laser beam spot in front of diamond cutting edge.

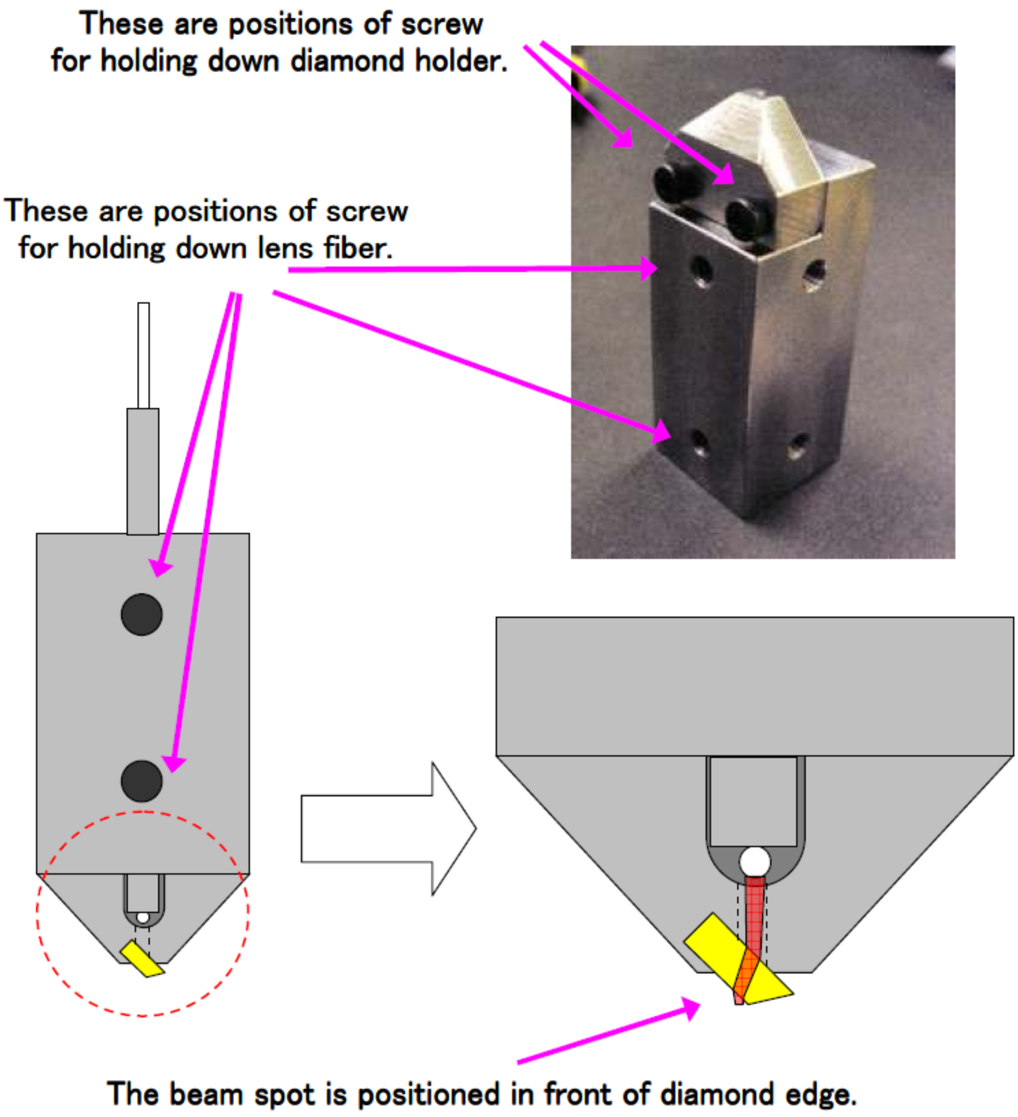

Figure 9.1. Illustration of the 1.4mm nose radius diamond cutting tool used in the experiment.

9.2.2.2. The μ-LAM System Setup

The IR laser beam is guided from the diode laser through a 10 μm fiber optic cable directly to the diamond cutting tool with a nose radius of 1.4mm, by using special connectors and adaptors. A simple μ-LAM system configuration used in this experiment is shown schematically in Figure 9.2.

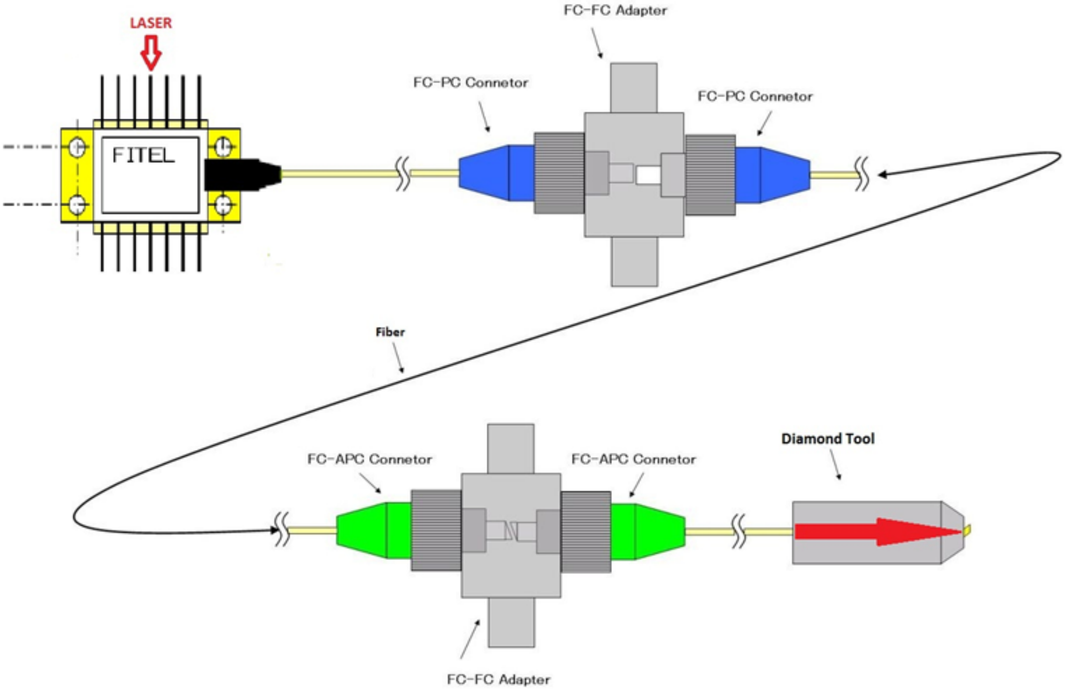

Figure 9.2. The µ-LAM system configuration for the 1.4mm nose radius diamond cutting tool setup.

9.2.2.3. Laser Power Output Results

The total laser power output was measured by using a high resolution (1 mW resolution) laser power meter with digital display (Model #3802 Sensor Interface Module (SIM) and #3831 Thermal Sensor, New Focus Inc.) which is explained in Chapter 5. Figure 9.3 shows the laser power output measurement results. The maximum power decreases from its original 350 mW to approximately ~300 (298) mW (at maximum laser diving current 1400 mA) after the tool is attached. It means that approximately 15% of the laser power is lost after attaching the diamond tool to the laser by using the adaptors. The potential reasons that could cause the observed power loss are explained in Chapter 5.

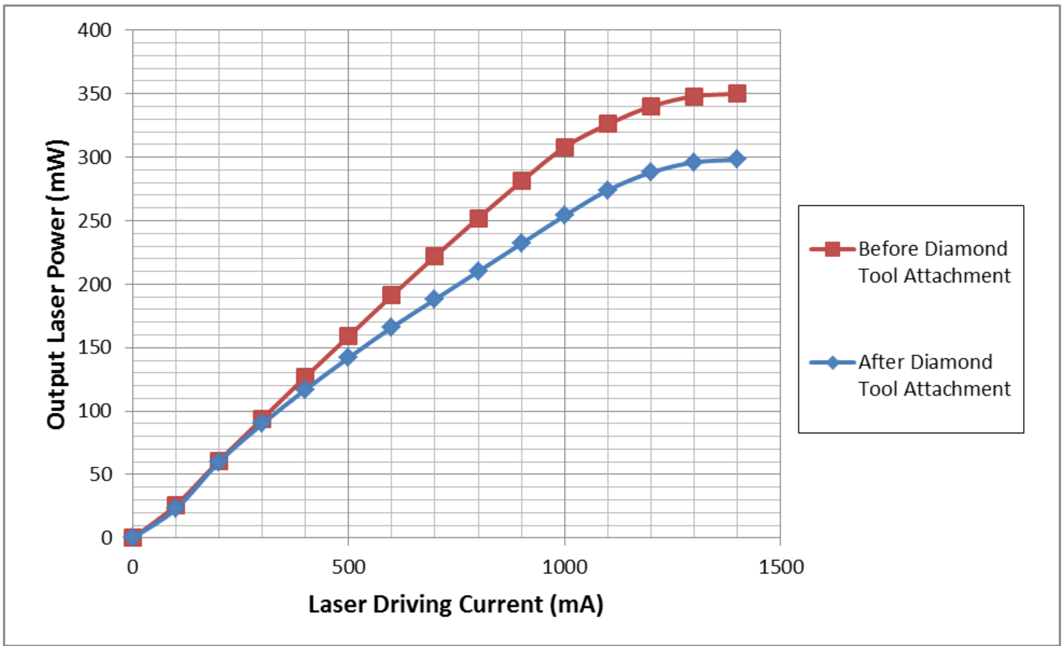

Figure 9.3. Laser output power measurements with and without the 1.4mm nose radius diamond tool attached.

9.2.2.4. Experimental Procedure

Scratches were performed with and without laser heating using an actual cutting tool similar to that used for SPDT. The loads (Fz) used for the scratch tests are 1g (~10mN), 1.5g (~15mN), 2g (~20mN), 2.5g (~25mN) and 5g (~50mN) with a cutting speed of 1μm/sec. Scratch lengths of 300 μm were produced on a single crystal Si wafer. The scratch test parameters are summarized in Table 9.2.

Table 9.2. Parameters used for the scratch tests on Si with 1.4mm nose radius diamond cutting tool setup.

Scratch #	**Load, F_z (mN)**	**Machining Condition**	**Cutting Speed (µm/sec)**	**Laser Power (mW)**
1	10	no laser	1	0
2	10	with laser	1	350*
3	15	no laser	1	0
4	15	with laser	1	350*
5	20	no laser	1	0
6	20	with laser	1	350*
7	25	no laser	1	0
8	25	with laser	1	350*
9	50	no laser	1	0
10	50	with laser	1	350*

**Only applicable for the scratches with laser heating. 350mW is the laser power, approximately 300mW is actually delivered to the work piece material, the remaining laser power is lost due to scattering and reflections.*

Only low loads were used in this study to maximize the laser heating; the laser beam size of approximately 10µm matched the lower applied loads, which yielded relatively shallow cuts with narrow widths (on the same size scale as the laser beam).

After scratch tests, the laser micro-Raman spectrometer was used to acquire Raman spectra to characterize the material structural changes after ductile mode machining with and without laser heating.

9.3. Results and Discussions

9.3.1. Results for 5µm Tip Radius Diamond Tool

Figure 9.4 shows two scratches with and without laser heating (scratches 2 and 1 respectively). The load range (20-70 mN) performed on these scratches exhibited both, the ductile and brittle regime (with a DBT zone) along the same scratch. The ductile to brittle transition is identified somewhere between the ductile and brittle regime of the scratch using optical microscopy, white light interferometry and force analysis (from variations in cutting forces). Figure 9.5 shows a high magnification optical microscope image used to identify brittle fracture along the scratch. It is seen in Figure 9.5 that the scratch performed without laser heating (top scratch) exhibits brittle fracture along the cut much before the scratch performed with laser heating (bottom scratch). The indication of brittle fracture for the scratch done with laser heating is not seen in Figure 9.5 as it is outside the field of view.

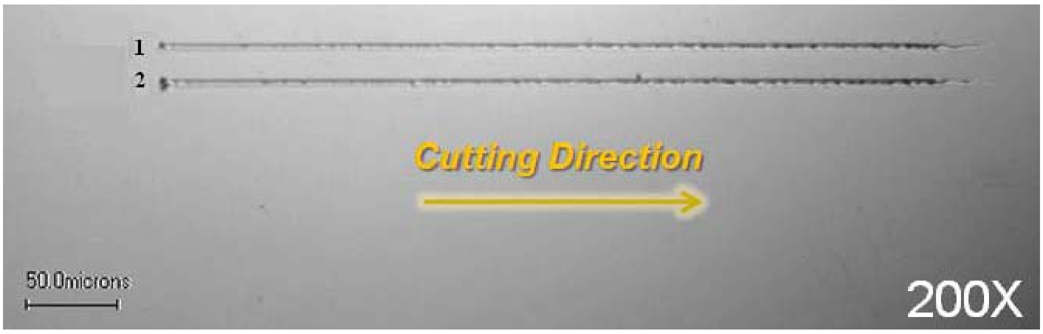

Figure 9.4. Scratches done with (2) and without laser heating (1).

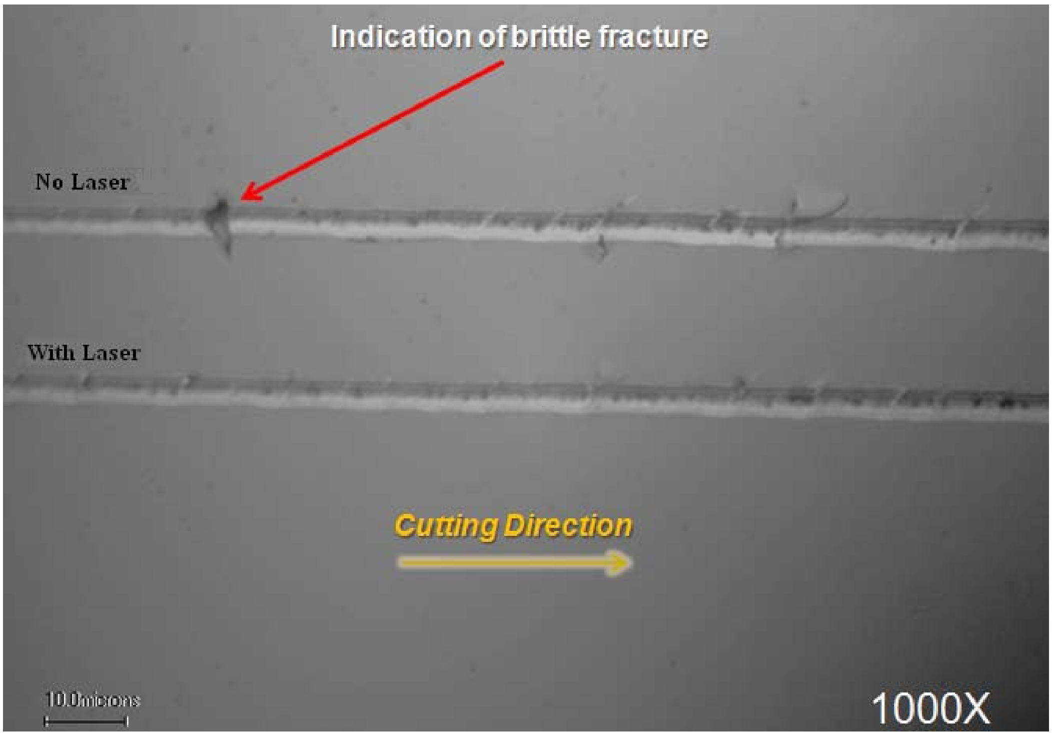

Figure 9.5. Micrograph showing brittle fracture along the scratch in Si.

In this study, there were two different analyses done based on the results obtained from the scratch tests. The first analysis compares the depth of cut and cutting forces (F_x) for a constant thrust force (F_z) for both cutting conditions (with and without laser heating). For this analysis, scratches analyzed for both conditions were in the ductile regime. The results summarized in Table 9.3 show that for the same amount of applied thrust force (F_z = 20mN), the scratch performed with laser heating yielded a greater depth of cut (400nm vs. 280nm). It is also evident that the scratch performed with laser heating yielded a slightly lower cutting force for an equal applied thrust force (although the scratch performed with laser heating was significantly deeper). A scratch without laser heating done at higher loads, to result in a depth of cut of 400nm, will most definitely result in higher cutting forces due to the hardness of the material.

Table 9.3. Scratch test results for Si.

Machining Condition	Load, F_z (mN)	Load, F_z (mN)	Depth of Cut, DoC (nm)	Scratch Nature
no laser	20	6.0	280	Ductile
with laser	20	5.5	400	Ductile
no laser	35	9.0*	***480****	DBT
with laser	42	8.0*	***710****	DBT

**Measurement taken just before the DBT occurs.*

Investigations were also carried out to understand the effects of laser heating on the DBT of the material. During these studies, the scratches were examined using a white light interferometer. Figure 9.6 shows the cross-section of the two scratches taken at an equal thrust force of approximately 35mN. It can be seen in Figure 9.6 that the scratch performed with laser heating (left) exhibits a perfectly ductile behavior (with a depth of 700nm) whereas the scratch done without laser heating indicates the onset of fracture at a depth of 480nm. The brittle behavior is identified by the imperfect pattern of the groove which is a representation of the stylus imprint on the material.

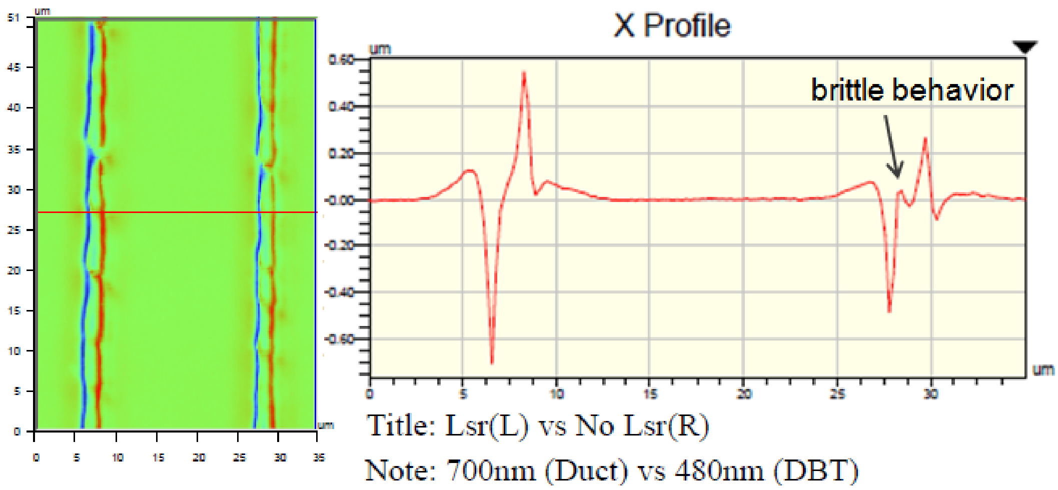

Figure 9.6. Cross-section of scratches on Si obtained from a white light interferometer.

Figure 9.7 illustrates a three-dimensional scratch profile that gives a clear illustration of the nature of the scratch: i.e., ductile or brittle. Here, it can be clearly identified that the scratch performed with laser heating (left hand side) still exhibits ductile behavior whereas the scratch performed with no laser heating (right hand side) shows brittle behavior for similar thrust forces. The clear and defined edges that depict the stylus imprint are a good indication of ductile response of the material (as seen in the scratch performed with laser heating).

Figure 9.7. 3D scratch profiles of the Si scratches with and without laser heating (related to the same area imaged in Figure 9.6).

Figure 9.8 shows the cross-section of these same scratches taken at an equal thrust force of approximately 42mN. It can be seen that the scratch performed with laser heating (left) indicates a ductile to brittle transition at a depth of 710nm whereas the scracth without laser heating indicates severe fracture. At this load, the scratch performed with no laser heating shows signs of severe fracture at a depth of 540nm. In comparison, the DBT depth of the scratch performed with laser heating was approximately 260nm greater than the DBT depth of the scratch performed without laser heating.

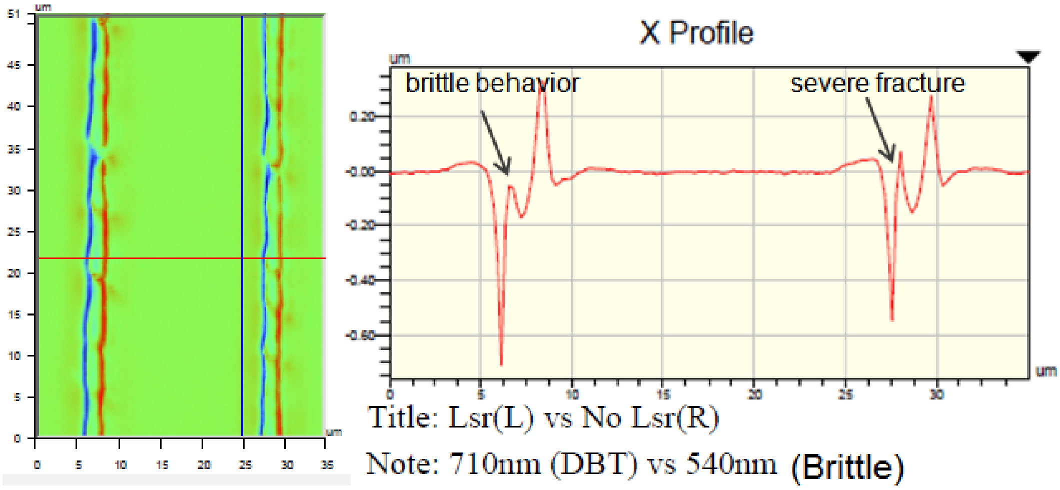

Figure 9.8. Cross-section of scratches on Si obtained from a white light interferometer.

Figure 9.9 shows the cutting force comparison for the scratch with and without laser heating for a linearly increasing thrust force/load. Force data analysis is yet another method used to confirm the DBT and identify the onset of fracture behavior in the material. As seen in the cutting force data (blue and red lines), instability (large peaks and valleys on a linearly increasing line) in cutting forces are usually correlated to fracture occurrence along the scratch. Another advantage of force analysis is that fracture can be observed in-situ via the instability observed in the cutting forces (blue and red lines) during the scratch experiments. This is an important aspect while attempting ductile mode machining of brittle materials as the force data will indicate the onset of brittle behavior (during the cutting process: in-situ) allowing the machinist to reduce the depth of cut of thrust force avoiding fracture or even catastrophic failure in the material. From the force data in Figure 9.9, it is clear that the cutting forces for the scratch performed with laser heating are lower than the cutting forces for the scratch with no laser heating (although scratch with laser heating yields a greater depth of cut) for a similar applied thrust force.

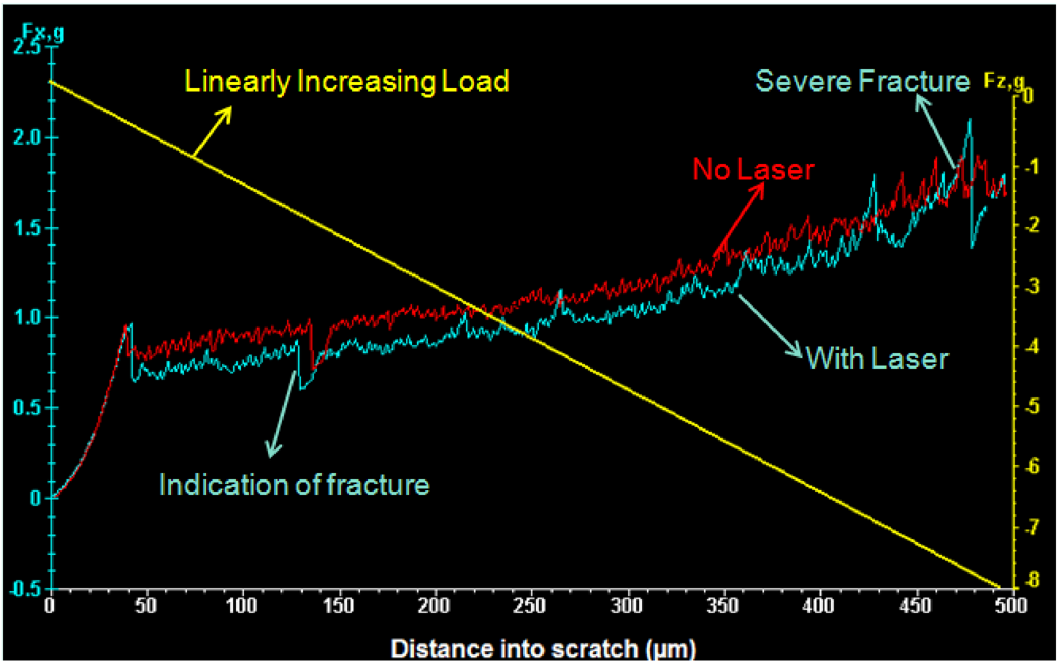

Figure 9.9. Force data (F_x = cutting force and F_z = thrust force) comparing the Si scratch with and without laser heating for equal loads (linearly increasing thrust force).

9.3.1.1. Micro-Raman Spectroscopy Results

Micro-Raman spectroscopy was used to examine the material inside the scratch grooves to probe for indications of phase transformations. The Raman laser was focused on the center of the groove of the scratch, where the greatest heating affect should occur, to evaluate the combined effect of the HPPT and laser heating. Preliminary Micro-Raman analysis has been carried out (at Argonne National Laboratory) successfully on cuts performed with and without laser heating on Si. In this preliminary analysis, two different laser excitation wavelengths were used; HeCd (442nm blue laser) and ArlON (514nm green laser). The micro-raman spectra of the scratches machined with and without laser, as well as unmachined surface of Si, are shown below in Figures 9.10. For the machined surfaces all the micro-Raman data are taken from the same ductile region.

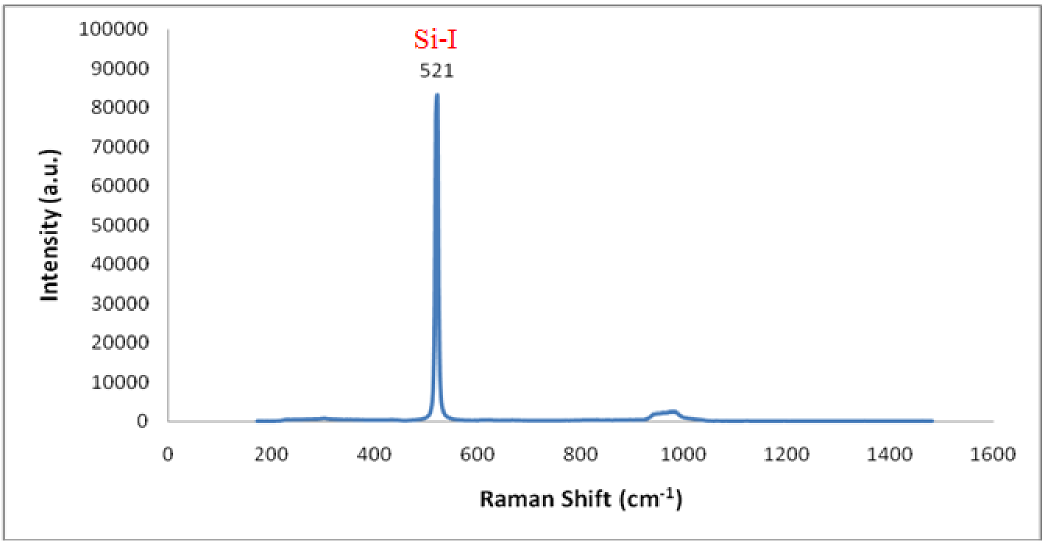

Figure 9.10. Micro-Raman spectrum using a 442nm wavelength excitation laser for the unmachined surface (showing only crytalline Si peak).

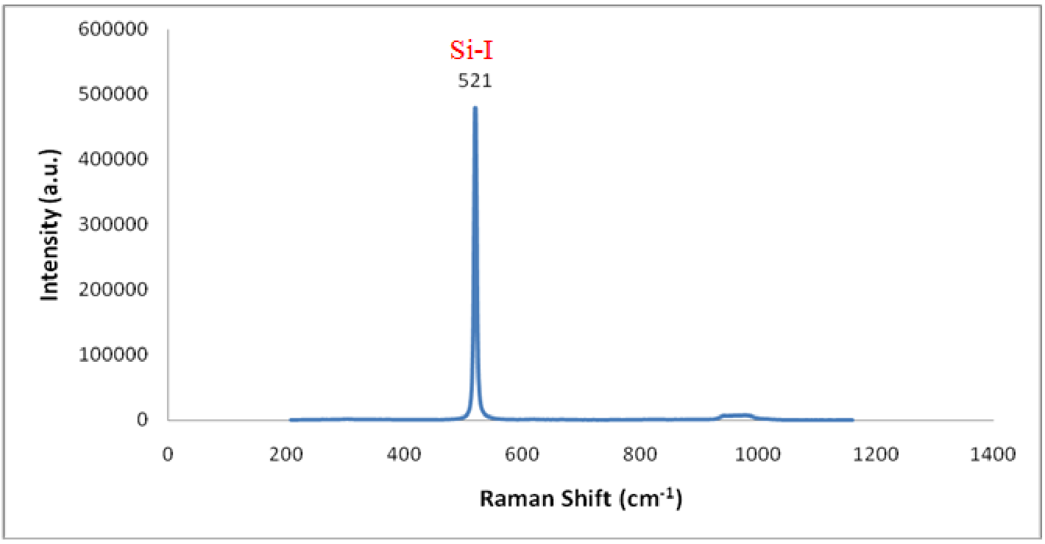

Figure 9.11. Micro-Raman spectrum using a 514nm wavelength excitation laser for the unmachined surface (showing only crytalline Si peak).

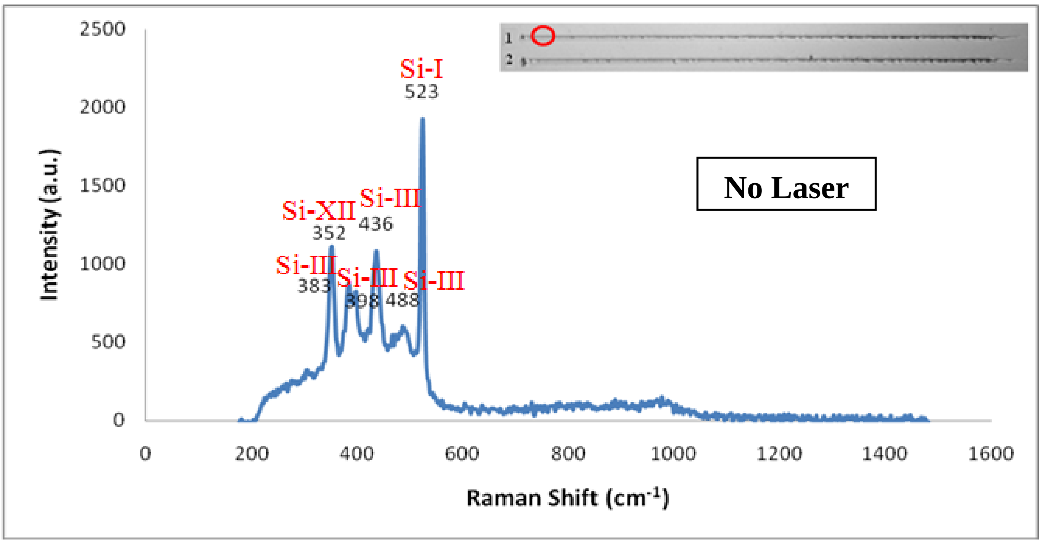

Figure 9.12. Micro-Raman spectrum using a 442nm wavelength excitation laser for the ductile mode material removed surface without laser heating.

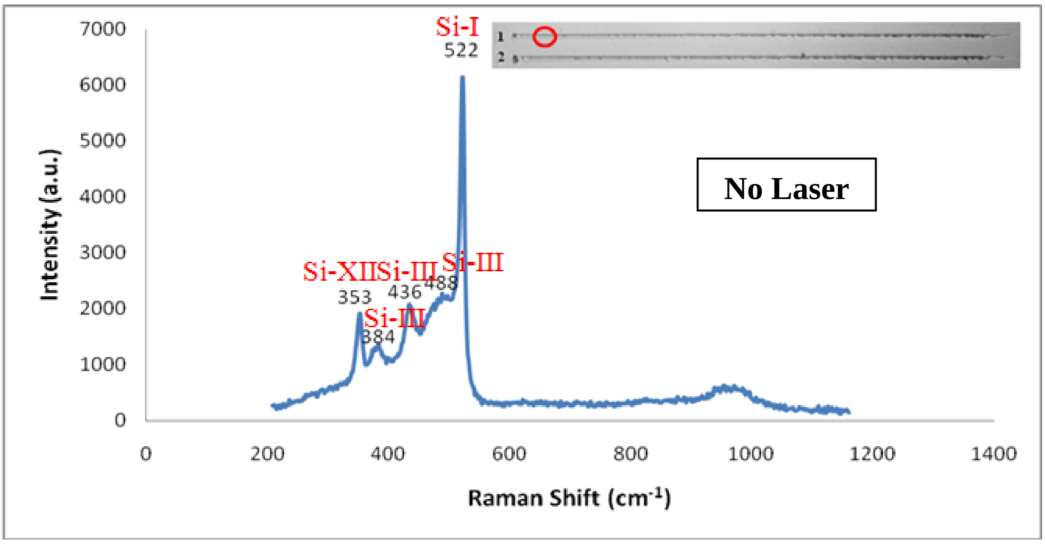

Figure 9.13. Micro-Raman spectrum using a 514nm wavelength excitation laser for the ductile mode material removed surface without laser heating.

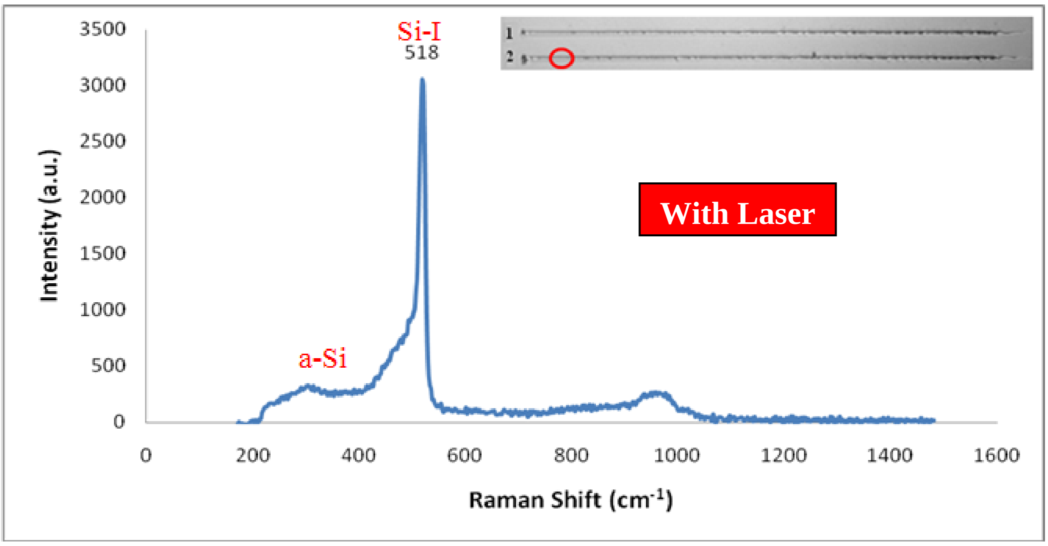

Figure 9.14. Micro-Raman spectrum using a 442nm wavelength excitation laser for the ductile mode material removed surface with laser heating.

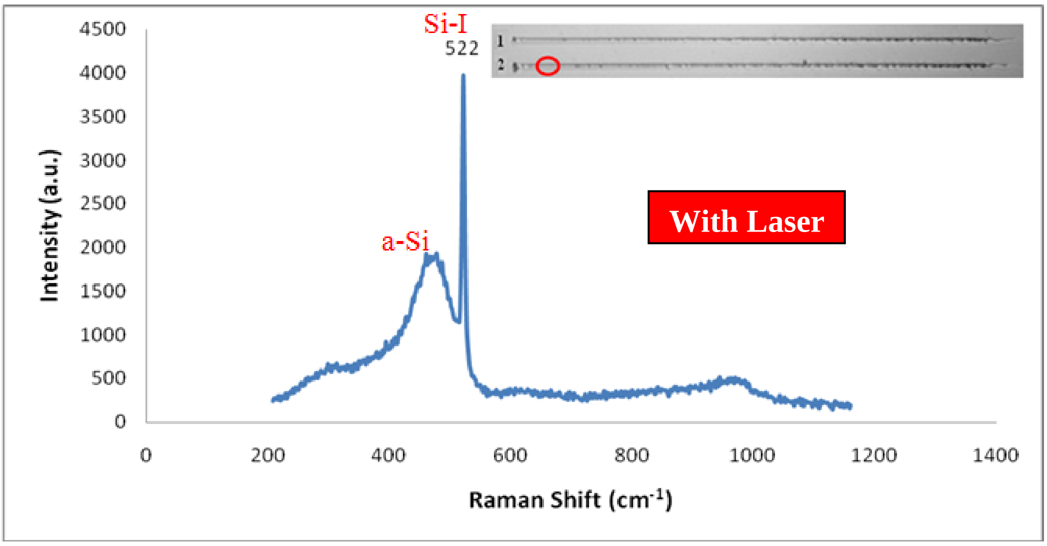

Figure 9.15. Micro-Raman spectrum using a 514nm wavelength excitation laser for the ductile mode material removed surface with laser heating.

The micro-raman spectra obtained from both wavelengths (442nm and 514nm) are identical. The micro-Raman spectra from the grooves of the scratches demonstrated the phase transformation and formation of metastable phases including a-Si, Si-I, Si-III and Si-XII. The phases that frequently appeared in the grooves are, semiconducting Si-I (*c*, cubic diamond structure), Si-III (*bc*8, body-centered cubic structure) [162], Si-XII (*r*8, the rhombohedral distortion of *bc*8) [163] and amorphous silicon (a-Si) [164]. Si-IV (*hd*, hexagonal diamond structure) [162] was never found in the scratch grooves.

From the micro-Raman spectra of the machined surfaces without laser heating (Figures 9.12 and 9.13), Si-XII and Si-III are the two most obvious peaks, besides the Si-I peak (between 518-523 cm^{-1}) in the chosen range of the Raman spectrum. No significant amorphous phase is observed in the scratches without laser heating, although there is some broadening (indicative of amorphous silicon, a-Si) presented in the scratches with laser heating (Figures 9.14 and 9.15).

From the micro-Raman spectra of the machined surfaces with laser heating (Figures 9.14 and 9.15), there is a significant amorphous Si (a-Si) phase is observed besides the Si-I peak (at about 520cm^{-1}) in the chosen range of the Raman spectrum. The amorphous phase, which also back transforms from the high pressure Si-II phase, typically occurs during fast unloading, such as during machining or scratching at higher speeds [52, 165]. But in this study the a-Si phase is observed within the laser heated scratches after slow unloading during scratching at a slower speed of 1µm/sec.

Si-XII and Si-III indicate the prior existence of Si-II during the scratching, i.e. Si-III and Si-XII form from unloading the Si-II high pressure metallic phase. Usually slow unloading results in polymorphous phases such as Si-XII and Si-III instead of amorphous silicon (a-Si) [52, 165].

From previous research studies it's known that under contact loading, Si undergoes a series of phase transformations [96]. If the hydrostatic pressure reaches 10–13GPa, high pressure metallic phase Si-II (*β*-Sn) forms from the semiconducting Si-I. Metallic Si-II is not stable below ~4GPa [52] on unloading and transforms to other phases depending on pressure release conditions.

Many brittle materials are capable of ductile behavior, but only under high hydrostatic pressure [27]. Thus, a high value of the hydrostatic pressure is the required driving force for phase transformation and a prerequisite for plastic flow of the ductile metallic phase of Si (Si-II) formed under pressure. All the diamond tools used in this study provide sufficient pressures to enable the transformation of Si-I to metallic Si-II and plastic deformation of the material beneath the tool.

9.3.2. Results for 1.4mm Nose Radius Diamond Cutting Tool

All scratches were imaged using an optical microscope to ensure that there were no surface cracks or any form of brittle fracture. All images showed fully ductile cuts comparing both conditions (with and without laser heating).

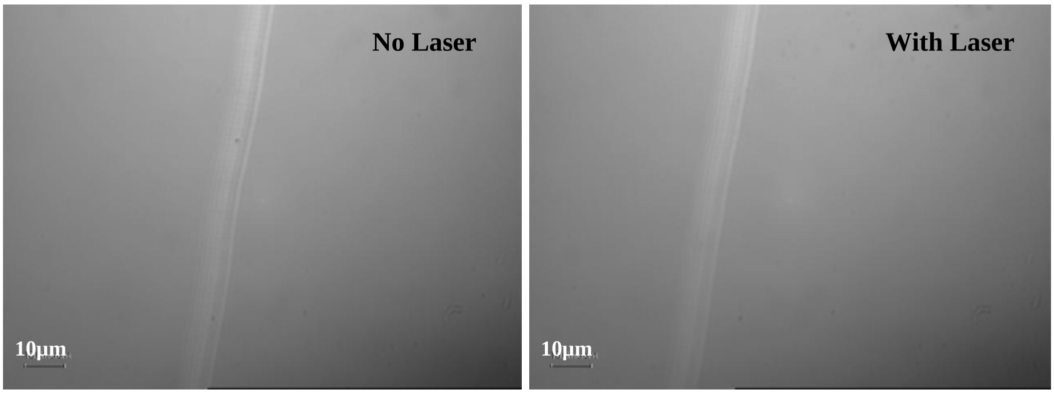

Figure 9.16. Image of part of the scratch done with a 10mN (1g) thrust force. (No visual difference seen under the optical microscope between a scratch done with and without laser heating. The image was taken at a 1000x magnification. The width of the scratches are approximately 10μm).

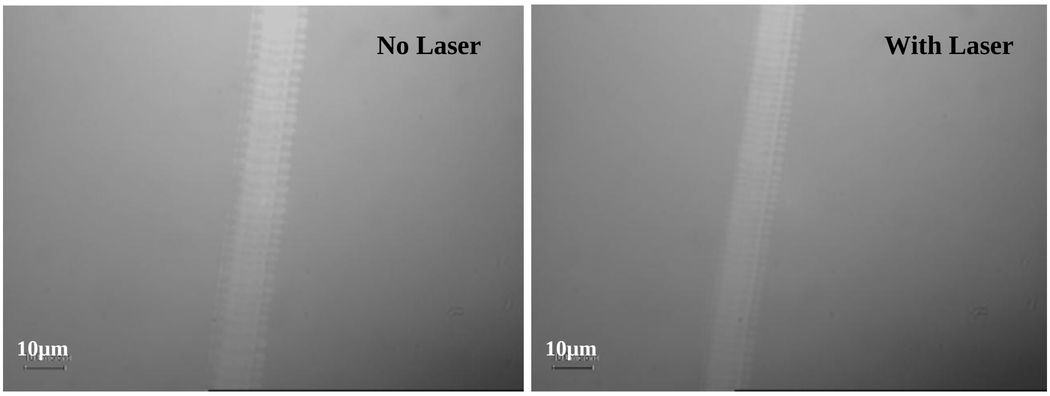

Figure 9.17. Image of part of the scratch done with a 15mN (1.5g) thrust force.
(No visual difference seen under the optical microscope between a scratch done with and without laser heating. The image was taken at a 1000x magnification. The width of the scratches are approximately 14µm).

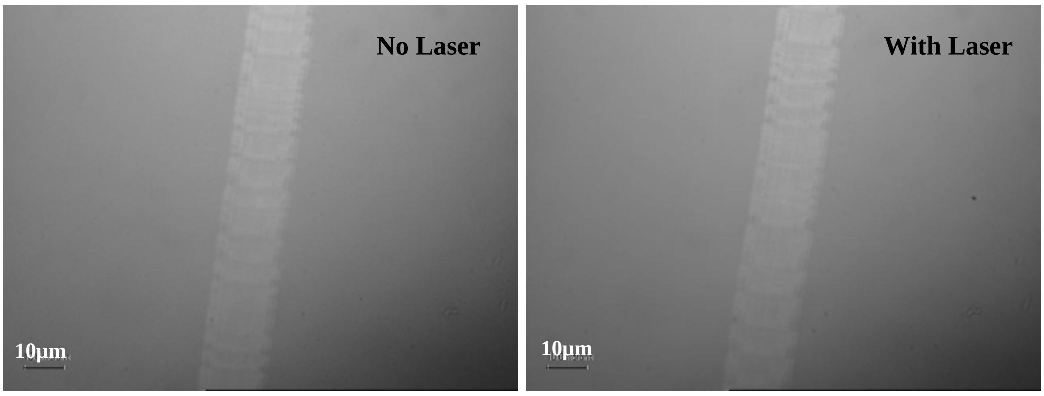

Figure 9.18. Image of part of the scratch done with a 20mN (2g) thrust force.
(No visual difference seen under the optical microscope between a scratch done with and without laser heating. The image was taken at a 1000x magnification. The width of the scratches are approximately 17µm).

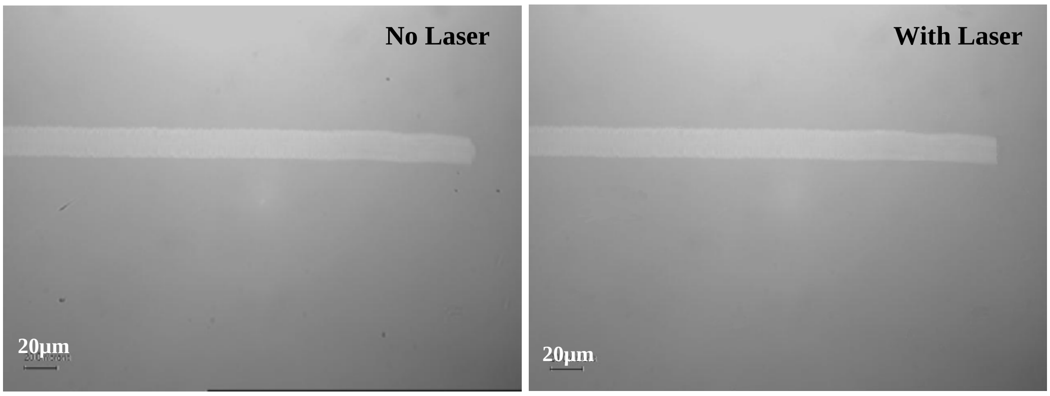

Figure 9.19. Image of part of the scratch done with a 25mN (2.5g) thrust force.
(No visual difference seen under the optical microscope between a scratch done with and without laser heating. The image was taken at a 400x magnification. The width of the scratches are approximately 18.5µm).

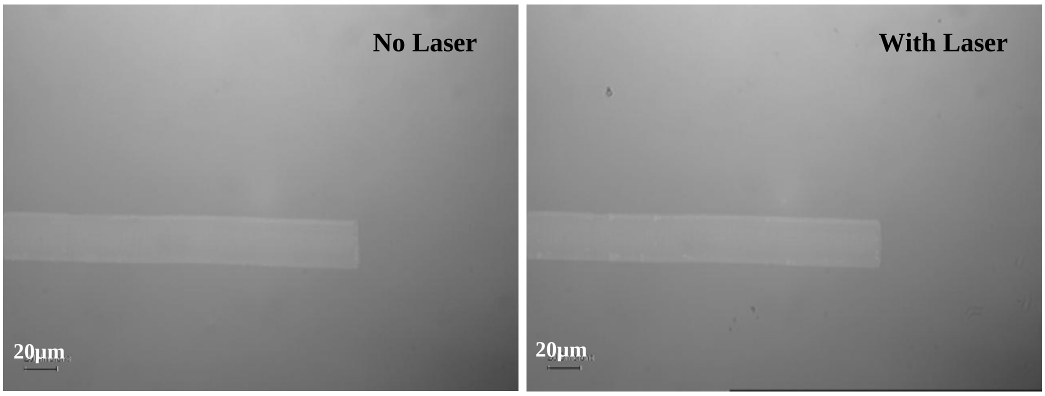

Figure 9.20. Image of part of the scratch done with a 50mN (5g) thrust force.
(No visual difference seen under the optical microscope between a scratch done with and without laser heating. The image was taken at a 400x magnification. The width of the scratches are approximately 30µm).

From all the images shown, there were no obvious differences seen between the cuts (the purpose of optical microscopy here was only to look for evidence of brittle fracture, if any). Images have shown fracture-free surfaces generated using µ-LAM.

Figure 9.21 shows the cutting force comparison for the scratch done with a constant 50mN (5g) thrust force/load during the ductile mode machining (with and without laser heating). Figure 9.21 represents the force data plot obtained from both scratching conditions (with and without laser heating) showing cutting force (F_x) and thrust force (F_z) data for both scratches on Si. From the force data in Figure 9.21, it is clear that the cutting forces for the scratch performed with laser heating are lower than the cutting forces for the scratch with no laser heating (although scratch with laser heating yields a greater depth of cut) for a similar applied thrust force.

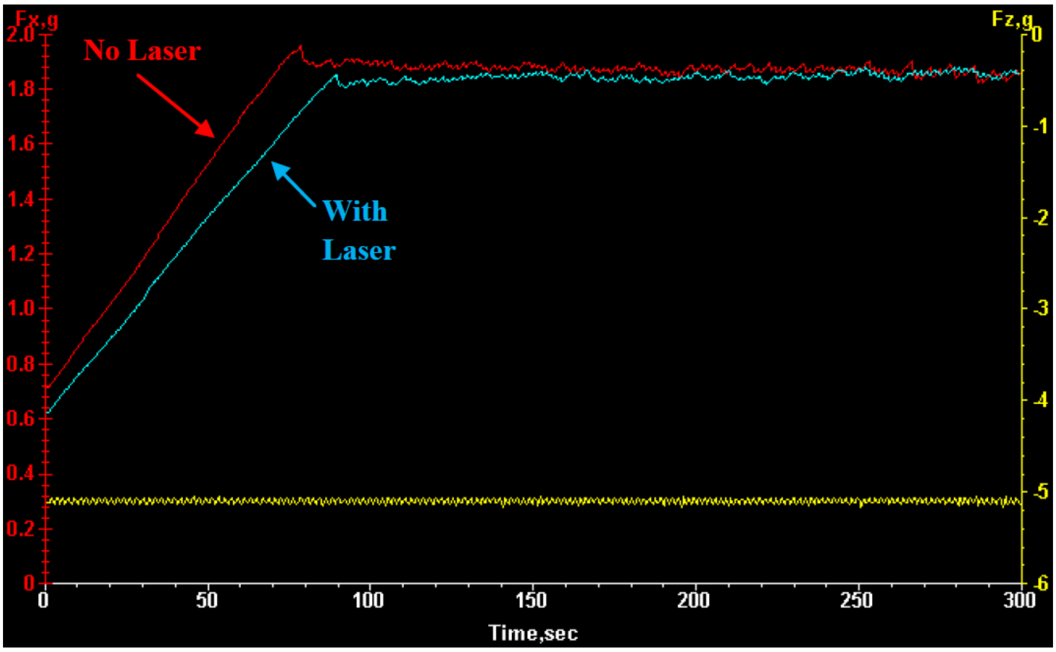

Figure 9.21. Cutting force data comparing the scratch done with laser heating and without laser heating at 50mN (5g).

All of the test results summarized in Table 9.4 show that for the same amount of applied thrust forces, the scratches performed with laser heating yielded greater depth of cuts.

Table 9.4. Test results of all the cuts performed on Si.

Scratch #	**Machining Condition**	**Thrust Force, F_z (mN)**	***Cutting Force, F_x (mN)**	***Width of Cut (µm)**	***Depth of Cut, DoC (nm)**	**%Increase in DoC**
1	no laser	10±2.9%	1.8±5.4%	10	16	-
2	with laser	10±2.8%	2.0±3.2%	10	20	25
3	no laser	15±1.7%	2.9±7.8%	14	26	-
4	with laser	15±1.7%	3.1±6.9%	14	28	8
5	no laser	20±1.5%	4.7±7.3%	17	28	-
6	with laser	20±1.3%	4.9±8.1%	17	32	14
7	no laser	25±1%	6.6±3%	18.5	31	-
8	with laser	25±1%	6.5±5%	18.5	35	13
9	no laser	50±0.5%	18.8±0.8%	30	50	-
10	with laser	50±0.5%	18.5±0.7%	30	60	20

** For the scratch performed at 10mN, 15mN and 20mN, the white light interferometer parameters were kept constant (i.e. light intensity) to minimize variation in readings. The cutting forces, width of cut and depth of cut recorded in the above table are the average of the maximum readings.*

Figure 9.22 compares the depth of cut with the applied thrust force for both testing conditions: with and without laser heating. From the figure it is clear that there is an increase in the depth of cut with laser heating for all applied loads experimented (i.e. 10mN, 15mN, 20mN, etc.). This is due to the enhanced ductility or reduced hardness and due to the thermal softening of the material.

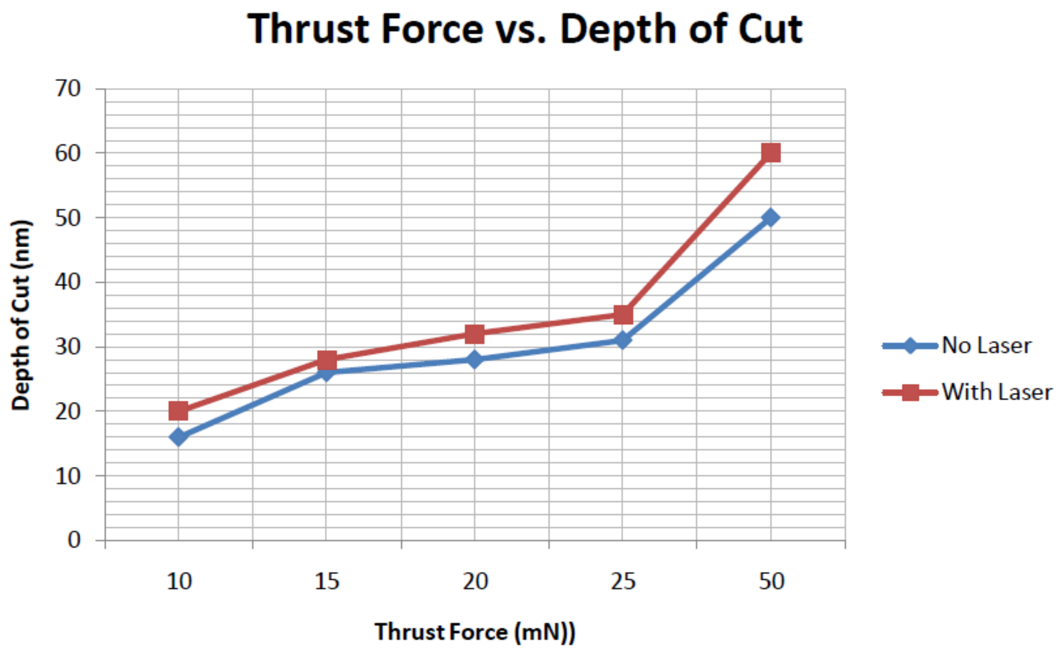

Figure 9.22. Depth of cut (DoC) versus the applied load for five different loads comparing with and without laser heating conditions.

9.3.2.1. Micro-Raman Spectroscopy Results

SEM studies have shown the ductile chip formation. Figure 9.23 shows SEM photomicrographs illustrating ductile chips formed after machining process of Si. The SEM image of the chips demonstrate that the chip formation mechanism involves plastic deformation and shear. Many other studies have shown and demonstrated similar ductile chip morphology [26, 58, 59, 64]. The chips are continuous and partially curled as seen in Figure 9.23.

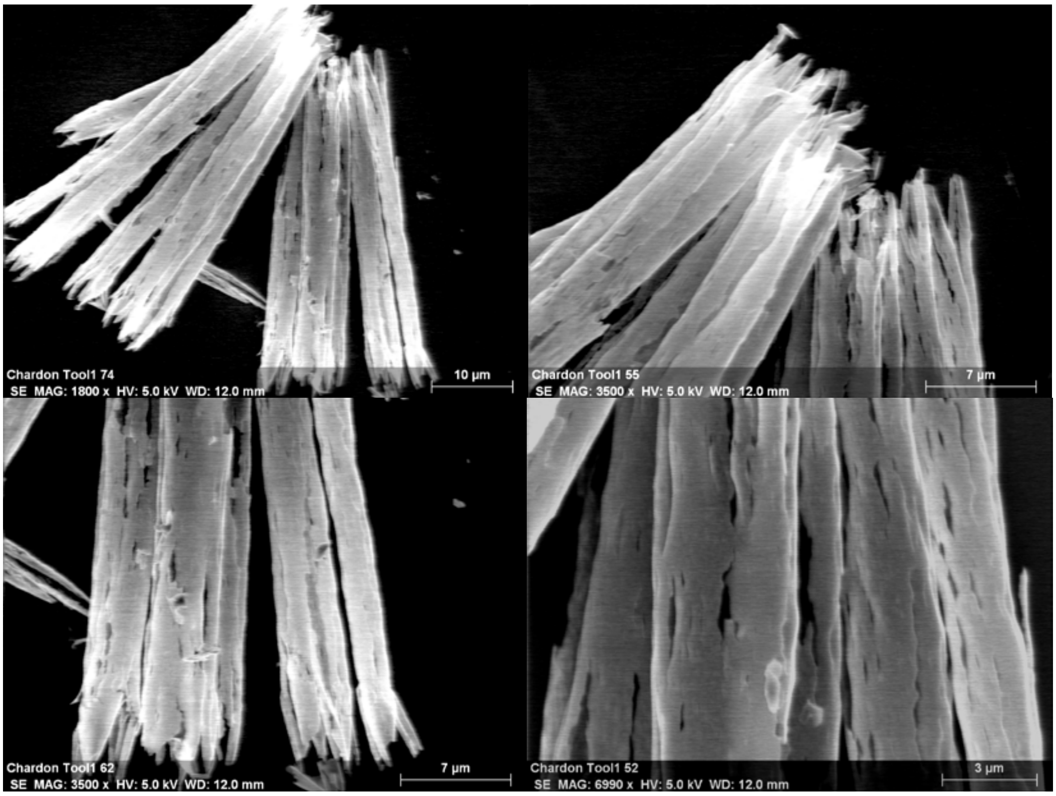

Figure 9.23. SEM images of ductile machined Si chips after machining.

The Raman laser was focused on the ductile chips formed after machining process to examine the ductile chips to probe for indications of high pressure phases. HeCd laser (blue laser) with a 442nm laser excitation wavelength was used to obtain the Raman spectra of five different locations on the chips. The micro-raman spectra of five spots on the chips are shown below (Figure 9.24).

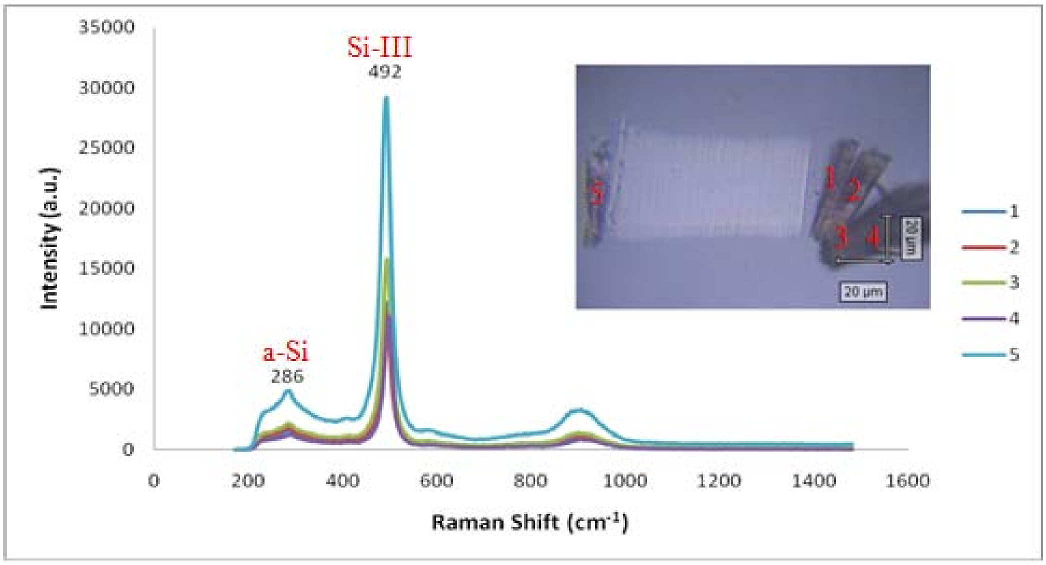

Figure 9.24. Micro-Raman spectra of five different spots on the chips using a 442nm wavelength excitation laser.

The micro-Raman spectra from the ductile chips demonstrated the phase transformation and formation of metastable phases including a-Si and Si-III. The chips produced during ductile mode machining were examined and found to be partially amorphous. The micro-raman spectra obtained from both points were identical and showed the same formation.

9.4. Conclusion

Micro-laser assisted scratch tests were successful in demonstrating the enhanced thermal softening of the material and a greater ductile to brittle transition depth. Laser heating was successfully demonstrated as evidenced by the significant increase in the ductile response of single crystal Silicon in the {100} plane along the <110> direction. Laser assisted (heating, thermal softening and reduced brittleness) material removal resulted in a greater depths of cuts at less applied thrust forces, smaller cutting forces and a larger critical DoC. It is clear from the experimental results that the cutting forces for the machined surface with laser heating are lower than the cutting forces for the machined surface without laser heating (although scratch with laser heating yields a greater depth of cut) for a similar applied thrust force. Due to the lower cutting forces and enhanced thermal softening of the material during the material removal process, lesser tool wear is predicted. The resultant material removal process did not cause any significant surface or subsurface cracks in ductile mode μ-LAM.

The occurrence of a HPPT of semiconductor and ceramic materials is often characterized by the amorphous remnant that exists on the surface and within the chips after machining. The HPP only exists while the transformation pressure is applied at the tip of the tool. When the pressure is released the HPP transforms to another phase that is stable at under that condition.

The micro-Raman spectra from the grooves of the scratches with and without laser demonstrated the phase transformation and formation of metastable phases including a-Si, Si-I, Si-III and Si-XII. From the micro-Raman spectra of the machined surfaces without laser heating, Si-XII and Si-III are the two most obvious peaks, besides the Si-I peak in the chosen range of the Raman spectrum. No significant amorphous phase is observed in the scratches without laser heating, although there is some broadening (indicative of amorphous silicon, a-Si) presented in the scratches with laser heating. It is clearly seen that the laser heating favors amorphization of the high pressure phase remnants which occur after μ-LAM.

Phase transformation also occurs in machining chips. That is, after unloading, a phase transformation from metallic phase to amorphous phase takes place in the chip material near the tool, as shown in Figure 9.25 [166].

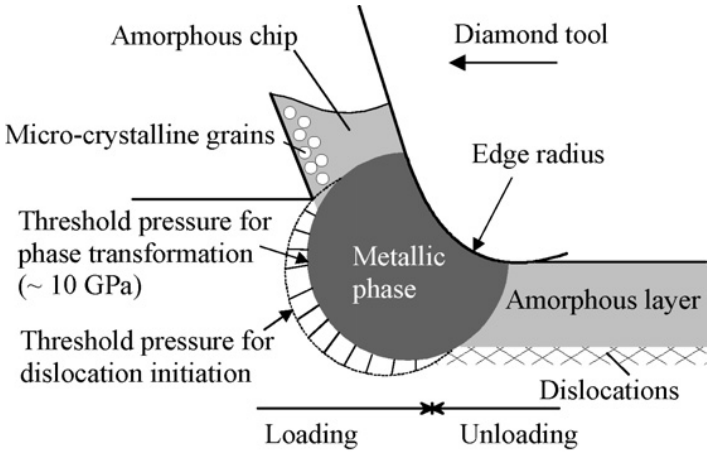

Figure 9.25. Schematic model for subsurface damage mechanism in Si during ductile machining.

Optical microscopy and SEM studies have shown ribbon-like ductile chip formation and fracture-free surfaces generated using ductile regime machining with and without laser heating. The micro-Raman spectra and the SEM images of the chips indicate that the chip is a mixture of amorphous Si and microcrystalline Si (Si-III). Because the pressure in the material near the free surface of the workpiece is lower than that beneath the tool, the phase transformation in the chip will be incomplete (see Figure 9.25). As a result, the chip becomes partly amorphous and partly crystalline (microcrystalline grains included in the amorphous phase), as seen in Figure 7.24. A similar phenomenon has been also confirmed by Morris et al. and Yan et al. [26, 166].

Force analysis (thrust and cutting), optical microscopy, SEM, white light interferometric profilometry and micro-Raman spectrescopy served as useful analyses methods to detect the enhanced ductile response and reduced brittle fracture as a result of preferential material heating (of the high pressure phase transformed material). Results obtained from this study are promising to further implement micro-laser assisted machining (μ-LAM) in operations such as single point diamond turning.

The results from this study also will benefit the manufacture of brittle materials as laser heating is proven to decrease the brittle response in ceramics and semiconductors, which can result in high productivity rates (i.e. higher material removal rate).

10. CONCLUSIONS, ONGOING and FUTURE WORK

10.1. Conclusions

A micro (µ) laser assisted machining (LAM) system has been designed, built, tested and evaluated. The µ-LAM system has been used to process difficult to machine materials such as, Si and SiC, which are typically very hard and extremely brittle and therefore not easily formed or shaped. Both workpieces are semiconductor-grade single-crystal materials. Results achieved include a substantial reduction in hardness of the material (~50% reduction) and a corresponding significant reduction in the cutting forces (also ~50%). This combination of reduced hardness and concomitant lower cutting forces promotes less tool wear, and consequently increases tool life. Another potential related benefit of the process is a reduction in fracture or brittle behavior of the material. While this was not the primary goal of the µ-LAM innovation/technology, it is a byproduct and benefit associated with the process. The heating and thermally induced softening can reduce the propensity of these nominally brittle materials to fracture, as a result of an overall increase in fracture toughness due to the elevated temperatures. While it is not yet easy or practical to actually measure the process temperatures during processing, the estimated temperatures are greater than 600°C [151], and can be higher depending upon the process conditions (primarily related to laser power and cutting speed).

For this study, machining of semiconductors and ceramics, the sharpness of the diamond cutting tool provided an additional benefit of creating conditions at the cutting edge (a highly negative rake angle tool is also used) to achieve an extremely high stress state in the chip formation zone and cause a pressure-induced phase transformation, i.e., a high-pressure phase transformation (HPPT). While this effect is not needed for this process to be useful for all materials, it is particularly advantageous for semiconductors and ceramics, as these high-pressure phases tend to be metallic (not covalent), and thus are conducive to ductile or plastic deformation under proper conditions (using suitable machining or process parameters, such as speed, feed, and depth of cut, along with proper tool geometry).

In essence, the infrared laser was used to heat the workpiece during the machining process. As the laser beam passes through the tool, the laser wavelength used can achieve absorption and heating of the workpiece, and that can pass through the diamond cutting tool (i.e., the diamond is optically transparent to the laser). Other combinations of laser wavelengths can be used, depending on the workpiece and cutting tool materials. Fiber lasers are typically used, as they are compact, lower cost, and effective.

In the scratching tests performed in this work, low scratching speeds (1µm/sec) were used. While in the precision machining processes, cutting speeds are often orders of magnitudes time faster (m/sec). High processing speeds will shorten the resident heating time significantly, thus higher power lasers or an improved optical delivery system (or a combination of the two) will be required to achieve commercial applications. When adapting the preferential heating technique to SPDT machining, the heat source needs to be designed to guarantee that sufficient heat is supplied to achieve the desired thermal softening effect. This dissertation study demonstrated the feasibility and capability of developing the technology to adapt a µ-LAM to practical machining operations

Ductile regime machining of semiconductors and ceramics (Si and SiC) have been confirmed by the analysis of the chips and the smooth surfaces acquired. The observed amorphous region via micro-Raman studies supports the claims that the HPPT has happened for both for the hard and brittle semiconductors Si and SiC. The evidence of the formation of metallic Si (Si-II), which is beneficial for ductile-regime machining, has been indirectly confirmed by using micro-Raman spectroscopy. Metallic Si-II transforms to Si-XII and Si-III or amorphous silicon behind the moving tool. Semiconductor-to-metal transition (pressure-induced metallization) has been shown to play a key role in the process of ductile regime machining of brittle materials. A combination of scratch tests and Raman spectroscopy analysis can be used to optimize and monitor ductile regime machining of semiconductor and ceramic materials. Laser heated scratches were examined and found to be partially amorphous. It has been found that laser heating has an effect on amorphizing the metastable phases (Si III and Si-XII).

Micro-Raman studies have also shown that the chips removed from the workpiece during cutting (without laser heating) are a mixture of an amorphous phase and a polycrystalline phase.

In conclusion, it has been demonstrated that it is feasible to preferentially heat the high pressure phases of Si and SiC during the material deformation process, using laser heating via µ-LAM technology. The thermal softening effect resulting from the localized heating enhances the ductility, and thus improves the material's machinability. Laser heating plays a significant role in enhancing the ductile regime machining of Si and SiC. There was no brittle mode material deformation during all the µ-LAM of Si and SiC, when performed in ductile mode.

Finally, the novel µ-LAM prototype system can be used on semiconductor and ceramic materials (silicon, silicon carbide-SiC and silicon nitride-Si_3N_4) to improve the machinability and enhance the overall manufacturing process. The µ-LAM system can be integral to the machining process and implemented on an experimental or commercial diamond turning machine (DTM).

10.2. Ongoing and Future Work

Medium power laser (Visotek Fiber Laser System, 976nm wavelength and 10W max. laser power) will be coupled using optical components to a variety of diamond tools, as seen in Figure 10.1 (multiple tool vendors are used such as Chardon Tool & Supply Inc., Ohio, USA and K&Y Diamond, Canada).

Figure 10.1. Various types of diamond tools will be used in μ-LAM.

To further study the effects of high power laser heating on Si and SiC, an IPG fiber laser system (IPG Photonics Co., USA) (see Figure 10.2) (maximum power = 100W and wavelength, λ = 1070nm) will be tested with a 1 mm nose radius diamond cutting tool.

Figure 10.2. High power IPG laser system (1070 nm, 100 W).

A significant improvement to the laser delivery system was achieved with the addition of a laser head (from Laser Mechanisms Inc., Michigan, USA), which provides precise x, y, and z positioning of the laser beam with a complete adjustment relative to the cutting tool's edge (see Figure 10.3).

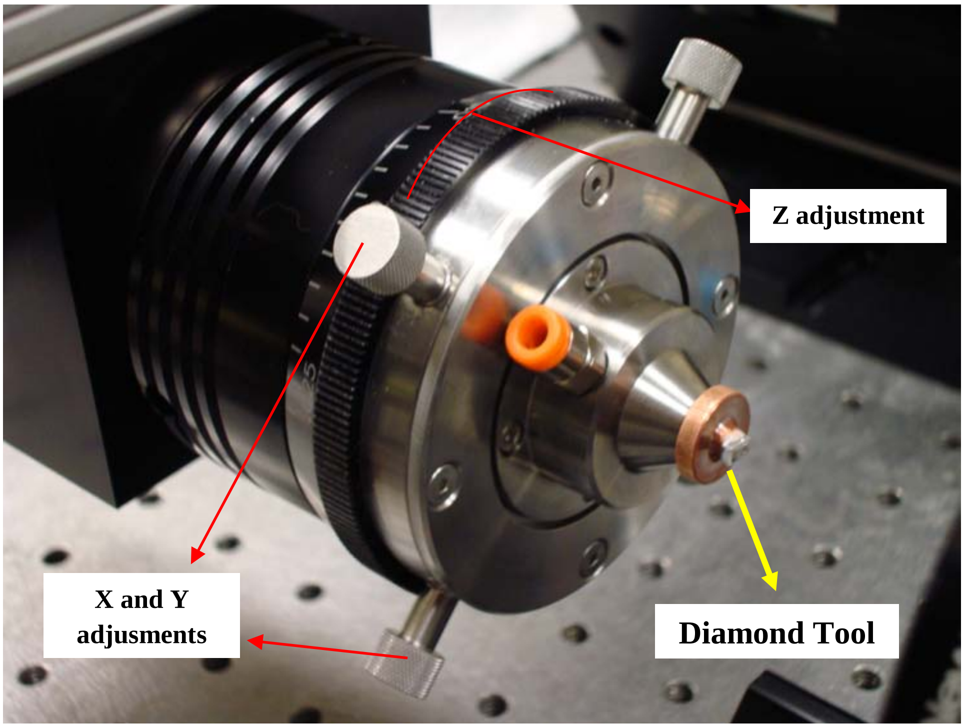

Figure 10.3. Laser mechanisms head with a beam delivery optics.

The IPG laser system is coupled with a modular head component which has beam delivery optics (from Laser Mechanisms, Inc.) that facilitates the diamond cutting tool (shown in Figure 10.4). The main objective is to study the material behavior with increased laser power (i.e. higher laser powers heat the surface more, resulting in enhanced ductility). Also, the machining parameters such as laser power, depth of cut and cutting speed will be optimized to obtain good surface finish with a higher material removal rate.

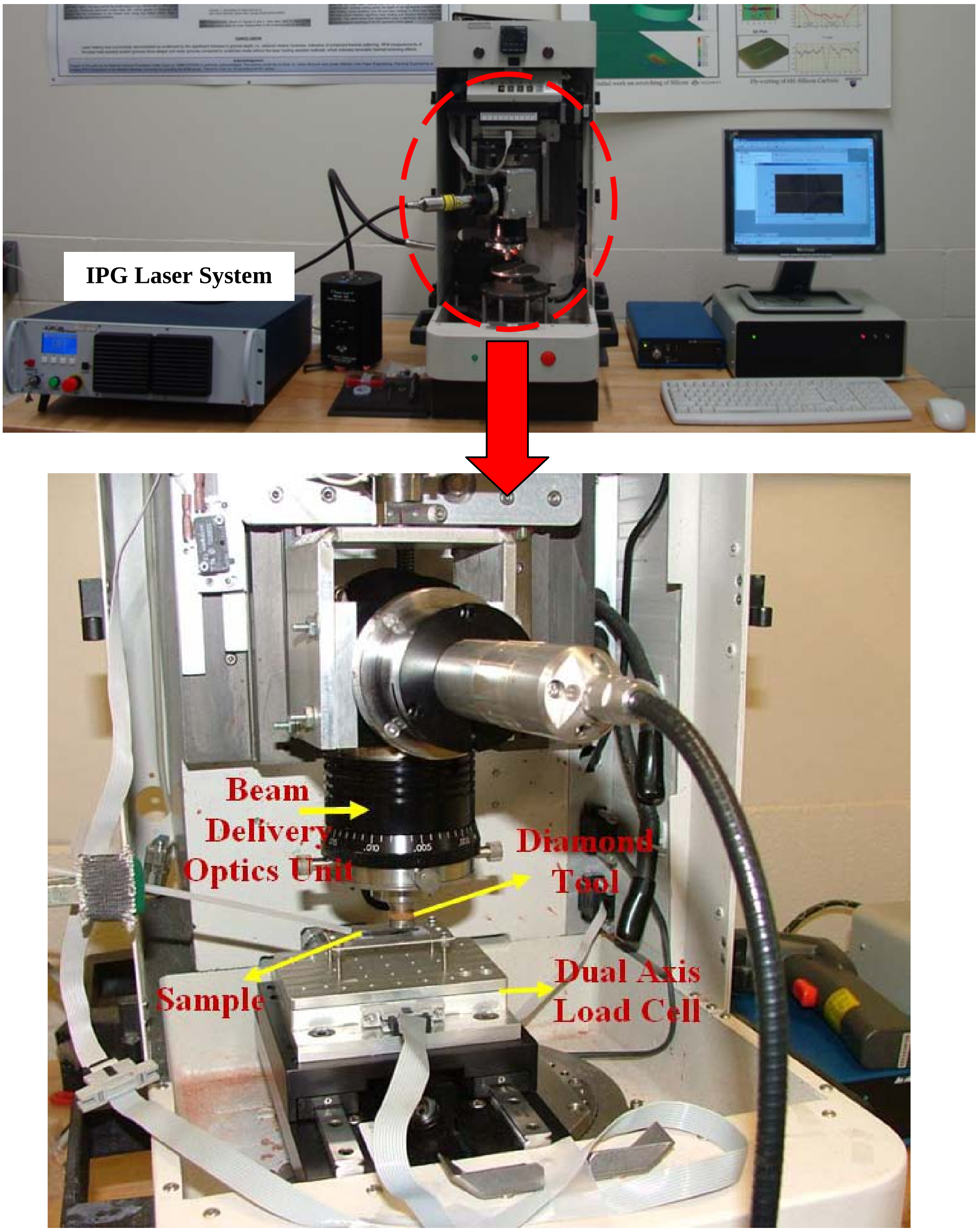

Figure 10.4. IPG Laser system coupled with a laser beam delivery optics unit.

TEM work of the cross-section of IR laser heated scratches on Si and SiC may be performed to corroborate with the micro-Raman analysis.

Raman spectroscopy measurements of IR laser heated scratches and chips will be performed under different scratching parameters, such as a wider range of scratching speeds.

High pressure and temperature tests were conducted at Argonne National Laboratory (ANL), Advanced Photon Source (APS) to determine the phase transition conditions and parameters of 4H, 6H and 3C SiC. The phase change in these SiC materials was seen over a pressure range of 66 - 88 GPa and at 1500 - 1600 K. It is believed (from preliminary results) that all three polytypes appear to form a dense cubic phase (3C) at these conditions. The data from these experiments is still being analyzed to determine the characteristics of the newly formed high pressure phase, such as optical absorption over the wide range of wavelengths (UV through IR).

The ongoing simulation work includes 3-D simulations of different depth of cuts as that of similar to the experiments and at room temperature to compare the cutting and thrust forces and cutting pressures. This comparison work will validate the simulation results. Further, 3D simulations will be conducted at elevated temperatures to compare with the experimental scratch tests done with the laser. Future work would also involve the study of the material behavior, i.e. thermal softening, beyond the thermal cutoff point up until the melting point. The experimental µ-LAM process will hopefully assist in determining those data points.

The development of the µ-LAM system will provide an entirely new tool and capability for fabricating components for advanced engineering systems from difficult to machine materials such as semiconductors and ceramics. The resulting µ-LAM system will also be portable and capable of being transported to various machine tools for use and evaluation.

Industrial interest in the technology and application of the µ-LAM technology to help solve real world industrial problems is expected to be significant when the system is demonstrated, validated and characterized. The study will be extended to industrial end users and technology providers (such as TWS, MLPC and Adamant Kogyo Co. Ltd.) to pursue applications of the technology, such as in virtual manufacturing (machining simulations) and manufacturing of advanced components (semiconductor, optical and structural ceramics).

Industries are interested in using the µ-LAM technology in producing high power semi-conductors of SiC for hybrid vehicles. Electric Power Research Institute (EPRI) has shown interest in using µ-LAM technology in the renewable energy generation especially in wind turbines. Outside the US, a Japanese company called Adamant Kogyo Co. Ltd. is pursuing to develop manufacturing semiconductors based on µ-LAM technology.

REFERENCES

[1] Askeland, D.R., The science and engineering of materials, 3rd edition, PWS Publishing Company, ISBN 0-534-93423-4, (1994).

[2] Lawn, B.R., ”Indentation of ceramic with spheres: A century after Hertz”, J. Am. Ceram. Soc., 81(8), 1977-1994 (1998).

[3] Jahanmir, S., Ives, L. K., Ruff, A. W., Peterson, M. B., “Ceramic Machining: Assessment of Current Practice and Research Needs in the United States”, NIST Special Publication, Vol. 834, 102. (1992).

[4] Patten, J.A., Fesperman, R., Kumar, S., McSpadden, S., Qu, J., Lance, M., Nemanich, R., Huening, J., “High-pressure phase transformation of silicon nitride”, Applied physics letters, 83(23), 4740-4742 (2003).

[5] Patten, J.A., Gao, W., Yasuto, K., “Ductile Regime Nanomachining of Single-Crystal Silicon Carbide”, Journal of Manufacturing Science and Engineering ASME, 127 (3), 522-532 (2005).

[6] Patten, J.A., Jacob, J., Bhattacharya, B. and Grevstad, A., “Comparison Between Numerical Simulations and Experiments for Single Point Diamond Turning of Silicon Carbide”, Transactions NAMRI/SME, Volume 35, pp. 89-96, (2007).

[7] Patten, J.A., Cherukuri, H., and Yan, J.W., “Ductile regime machining of semiconductors and ceramics”, Institute of Physics Publishing, pp. 661 (2004).

[8] Harris, G.L., “Properties of Silicon Carbide”, INSPEC, London (1995).

[9] Kamitani, K., Grimsditch M., Nipko, J.C., Leong, C.K., Okada, M., Kimura, I., “The Elastic Constants of Silicon Carbide: A Brillouin-scattering Study of 4H and 6H SiC Single Crystals”, Journal of Applied Physics, v82 (6), pp 3152-3154, (1997).

[10] Patten, J.A., Bhattacharya, B., “Single point diamond turning of CVD coated silicon carbide”, Journal of Manufacturing Science- ASME, Vol. 127, pp. 522, (2006).

[11] Patten, J.A., Bhattacharya, B., and Grevstad, A., “Comparison Between Numerical Simulations and Experiments for Single Point Diamond

Turning of Silicon Carbide", Transactions NAMRI/SME, Volume 35, pp. 89-96, (2007).

[12] Patten, J.A., Jacob, J., "Comparison between numerical simulations and experiments for single point diamond turning of single crystal silicon carbide", Journal of Manufacturing Processes, Vol. 10, pp. 28-33 (2008).

[13] Harris, G.L., "Properties of Silicon Carbide", INSPEC, London (1995).

[14] Walker, J., "Machining Fundamentals: From Basic to Advanced Techniques" Goodheart-Willcox, Illinois, (1999).

[15] Black, J.T., "Mechanics of chip formation", In: Davis, J.R. (ed) ASM Handbook: Machining, ASM International, Ohio, vol. 16, pp. 7–12 (1989).

[16] Pandey, P.C., Shan, H.S., "Modern Machining Processes", McGraw-Hill, New Delhi, (1980).

[17] King, R.I., "Handbook of high-speed machining technology", Chapman & Hall, New York, (1985).

[18] DeVries, W.R., "Analysis of Materials Removal Processes", Springer, New York, (2006).

[19] Springborn, R.K., "Non-traditional machining processes", American Society of Tool and Manufacturing Engineers, Michigan (1967).

[20] Benedict, G.F., "Non-traditional machining processes: introduction", In: Davis JR (ed) ASM Handbook: Machining, ASM International, Ohio, vol. 16, pp. 509–510 (1989).

[21] Zan, P. V., "Microchip Fabrication", McGraw-Hill Professional Publishing, 4th edition, ISBN: 0071356363, (2000).

[22] Shin, YC, Lei,S, Pfefferkorn, FE, Rebro, P., Rozzi, JC, Incropera, FP, "Laser assisted machining: its potential and future", Machining Technology, 11(3), 1-7 (2000).

[23] Wobker, H.G. and Tonshoff, H.K., "High efficiency grinding of structural ceramics", International conference on machining of Advanced Materials, NIST special publication 847, Gaithersburg, MD, 455-463 (1993).

[24] Blake, P. N., Scattergood, R. O., "Ductile-regime machining of germanium and silicon ", Journal of the American Ceramic Society, 73 (4), 949-957 (1990).

[25] Blackley, W. S., Scattergood, R.O., " Chip topography for ductile-regime machining of germanium", Journal of Engineering for Industry, 116, 264-266 (1994).

[26] Morris, J. C., Callahan, D.L., Kulik, J., Patten, J. A., "Origins of the Ductile Regime in Single-Point Diamond Turning of Semiconductors", Journal of American Ceramic Society, 78 (8), 2015-2020 (1995).

[27] Leung, T.P., Lee, W.B., Lu, X.M., "Diamond turning of silicon substrates in ductile-regime", Journal of Materials Processing Technology, 73, 42-48 (1998).

[28] Sreejith, PS, Ngoi, BKA," Material removal mechanisms in precision machining of new materials", International journal of machine tools & manufacture 41, 1831-1843 (2001).

[29] Yan, J. W., Syoji, K, Kuriyagawa, T. And Suzuki, H., "Ductile regime turning at large tool feed", Journal of Materials Processing Technology 121 (2-3): 363-372 (2002).

[30] Yan, J.W., Maekawa, K, Tamaki, J, et al., "Experimental study on the ultra-precision ductile machinability of single-crystal germanium", JSME INT J C-MECH SY 47 (1): 29-36 (2004).

[31] Yan, J., "Laser micro-Raman spectroscopy of single-point diamond machined silicon substrates", J. Appl. Phys. 95, 2094-2101, (2004).

[32] Flinn, R.A., Trojan, P.K., "Engineering materials and their applications", 4^{th} edition, Houghton Mifflin Company, (1990).

[33] Hall, H.T., "Ultrahigh-Pressure Research", Science, vol. 128, No. 3322, 445-449 (1958).

[34] Carter, G.F. and Paul, D.E., "Materials Science &Engineering", ASM International, ISBN: 0-87170-399-8, (1991).

[35] Clarke, D.R., Kroll, M.C., Kirchner, P. D., Cook, R. F., "Amorphization and conductivity of silicon and germanium induced by indentation", Physical review letters, 60(21), 2156-2159 (1988).

[36] Callahan, D.L., Morris, J.C., " The extent of phase transformation in silicon hardness indentations", J. Mater. Res., 7(7), (1992).

[37] Juliano, T., Gogotsi, Y., Domnich, V., “Effect of indentation unloading conditions on phase transformation induced events in silicon”, J MATER RES 18 (5), 1192-1201 (2003).

[38] Hu, J.Z., Merkle, L.D., Menoni, C.S., Spain, I.L., HU J. Z.,”Crystal data for high-pressure phases of silicon”, PHYSICAL REVIEW B, 34 (7), 4679-4684 (1986).

[39] Minowa, K. and Sumino, K., “ Stress-indeuced amorphization of a silicon crystal by mechanical scratching”, Physical Review Letters, 69(2), 320-325 (1992).

[40] Nix, W.D., Gao, H.J., “Indentation size effects incrystalline materials: a laws for strain gradient plasticity”, J. Mech. Phys. Solids, 46(3), 411-425 (1998).

[41] Morris, J. C., Callahan, D.L., “Origins of microplasticity in low-load scratching of silicon”, J MATER RES 9 (11), 2907-2913 (1994).

[42] Yin, L., Vancoille, E.Y.J., Ramesh, K., Huang, H., “Surface characterization of 6H-SiC (0001) substrates in indentation and abrasive machining”, Internationa Journal of Machine Tools and Manufacture, vol. 44, 607-615 (2004).

[43] Gerk, A.P., Tabor, D., “Indentation hardness and semiconductor-metal transition of germanium and silicon”, NATURE, 271 (5647): 732-733 (1978).

[44] Born, D. K., Goodman, W.A., “An empirical survey on the influence of machining parameters on tool wear in diamond turning of large single-crystal silicon optics”, PRECIS ENG 25 (4), 247-257 (2001).

[45] Pharr, G.M., “The anomalous behavior of silicon during nanoindentation”, Mat. Res. Soc. Symp. Proc., vol. 239, 301-313 (1992).

[46] Lawn, B. R., Hockey, B. J., Richter, H., “Indentation analysis: applications in the strength and wear of brittle materials”, Journal of Microscopy, 130(3), 295-308 (1983).

[47] Minomura, S. and Drickamer, H.G., “Pressure induced phase transitions in silicon, germanium and some III-V compounds”, J. Phys. Chem. Solids. Vol. 23, 451-456 (1962).

[48] Bridgman, P. W.,"The resistance of 72 elements, alloys and compounds to 100,000 kg/cm^2", Proc. Am. Acad. Arts. Sci., vol 81, 167-251 (1952).

[49] Sutton, A.P., Balluffi, R.W.," Overview no.61: On geometric criteria for low interfacial energy", Acta. Metallurgica, 35(9), 2177-2201 (1987).

[50] Hirata, N., Abbott, D., Patten, J.A., Hocken, R.J., "Measurements of the electrical conductivity of Silicon during scratching", http://www.micro.physics.ncsu.edu (2002).

[51] Kailer, A., Nickel, K. G. and Gogotsi, Y. G., "Raman Microspectroscopy of Nanocrystalline and Amorphous Phases in Hardness Indentations", Journal of Raman Spectroscopy, 30, 939-946, (1999).

[52] Domnich, V., Gogotsi, Y., and Dub, S., "Effect of phase transformations on the shape of the unloading curve in the nanoindentation of silicon", Appl. Phys. Lett. 76, 2214 (2000).

[53] Gogotsi, Y.G., Domnich, V., Dub, S., Kailer, A. and Nickel, K. G., "Cyclic nanoindentation and Raman microspectroscopy study of phase transformations in semicondcutors", J. Mater. Res., Vol. 15, No. 4, 871-879, (2000).

[54] Gogotsi,Y.G., G. Zhou, S.S. Ku, S. Cetinkunt, "Raman microspectroscopy analysis of pressure-induced metallization in scratching of silicon", Semicond. Sci. Tech. 16, 345, (2001).

[55] Pharr, G.M., Oliver, W.C. and Harding, D.S., "New evidence for a pressure-induced phase transformation during the indentation of silicon", J. Mater. Res., Vol. 6, No. 6, 1129-1130, (1991).

[56] Bridgman, P.W., "The compression of 39 substances to 100,000 kg/cm^2", Proc. Am. Acad. Arts. Sci., vol.76, 55-70 (1948).

[57] Jamieson, J. C., "Crystal Structures at High Pressures of Metallic Modificaitons of Silicon and Germanium", Science. Vol.139, (1963).

[58] Hu, J. Z. and I. L. Spain, "Phases of silicon at high pressure", Solid State Communications, 51(5), 263-266 (1984).

[59] Mujica, A., Rubio, A., Munoz, A, Needs, RJ," High-pressure phases of group-IV, III-V, and II-VI compounds", REVIEWS OF MODERN PHYSICS, vol. 75, 863-912 (2003).

[60] Yoshikawa, H., "Brittle-Ductile Behavior of Crystal Surface in Finishing," Journal of the Japan Society for Precision Engineering, 35-10, 662-667 (1969).

[61] Bifano, T.G., Dow, T. A., Scattergood, R.O., “Ductile-regime grinding - a new technology for machining brittle materials”, J ENG IND-T ASME, 113 (2), 184-189 (1991).

[62] Patten, J.A., Gao, W., Fespermann, R., “Ductile regime nanocutting of silicon nitride”, ASPE 2000 Annual Metting Proceedings, 106 (2000).

[63] Patten, J.A., Fesperman, R., Kumar, S., McSpadden, S., Qu, J., Lance, M., Nemanich, R., Huening, J., “High-pressure phase transformation of silicon nitride”, Applied physics letters, 83(23), 4740-4742 (2003).

[64] Yan, J. W., Syoji, K, Tamaki, J, “Some observations on the wear of diamond tools in ultra-precision cutting of single-crystal silicon”, Wear 255: 1380-1387 (2003).

[65] Jasinevicius, R.G., Santos, F.J.D., Pizani, P.S., Duduch, J.G. and Porto, J.V., “Surface amorphization in diamond turning of silicon crystal Surface amorphization in diamond turning of silicon crystal”, Journal of Non-Crystalline Solids 272, 174-178 (2000).

[66] Komanduri, R., “On material removal mechanisms in finishing of advanced ceramics and glasses”, Ann. CIRP 45(1), 509-514, (1996).

[67] Zhang, L.C., Mahdi, M., “Applied mechanics in grinding-IV. The mechanism of grinding induced phase transformation”, Int. J. Mach. Tools Manufact., 35(10), 1397-1409, (1995).

[68] Nix, W.D., Gao, H.J., “Indentation size effects incrystalline materials: a laws for strain gradient plasticity”, J. Mech. Phys. Solids, 46(3), 411-425, (1998).

[69] Shibata, T., Fujii, S., Makino, E., Ikeda, M., “Ductile-regime turning mechanism of single-crystal silicon”, Precision Engineering, 18, 129-137, (1996).

[70] Gilman, J.J., “Chemical theory of dislocation mobility”, MAT SCI ENG A-STRUCT 409, (1-2), 7-12 (2005).

[71] Nakasuji, T., Kodera, S., Hara, S.,matsunaga, H., "Diamond turning of brittle material for optical components", Annuals of the CIRP, 39(1), 89-92, (1990).

[72] Rebro, P.A., Pfefferkorn, F.E., Shin, Y.C., "Comparative assessment of laser-assisted machining for various ceramics", Transactions of NAMRI/SME, Vol.xxx, 153-226, (2002).

[73] Zhang, M., Hobgood, H.M., Demenet, J.L., and Pirouz, P., "The brittle-to-ductile transition in 4H-SiC", Materials Science Forum, Vol. 389-393: 767-770 (2002).

[74] Yan, J., Takahashi, H., Tamaki, J., Gai, X., Harada, H. And Patten, J.A., "Nanoindentation tests on diamond-machined silicon wafers", Applied physics letters, 86, 181913.1-3 (2005).

[75] Patten, J.A. and Gao, W., "Extreme negative rake angle technique for single point diamond nano-cutting of silicon", Precision Engineering, 25, 165-167 (2001).

[76] Ahn, S.J., Kim, D.W., Kim, H.S., et al. "Laser fabrication of micron-size apertures for electron beam microcolumns", APPL PHYS A-MATER, 69, S527-S530, (1999).

[77] Chen, MJ., Zhan, QL., Dong. S. and Li, D., "The critical conditions of brittle-ductile transition and the factors influencing the surface quality of brittle materials in ultra-precision grinding", Journal of materials processing technology, vol.168, 75-82 (2005).

[78] Sreejith, P.S., Ngoi, B.K.A., "Material removal mechanisms in precision machining of new materials", International Journal of Machine Tools & Manufacture, Vol.41, pp. 1831-1843, (2001).

[79] Maiman, T.H., "Stimulated Optical Radiation in Ruby," Nature 187, 493–494 (1960).

[80] Steen, W.M., "Laser Materials Processing", Springer, London, (1991).

[81] Wolbarsht, M.L., "Laser Applications in Medicine and Biology", Plenum Press, New York, (1991).

[82] Dausinger, F., Lichtner, F., Lubatschowski, H., "Femtosecond Technology for Technical and Medical Applications", Springer, Berlin, (2004).

[83] Ion, J., “Laser Processing of Engineering Materials: Principles, Procedures and Industrial Applications”, Butterworth-Heinemann, Oxford, (2005).

[84] Welch, A.J., Gardner, C., “Optical and thermal response of tissue to laser radiation”, In: Waynant RW (ed) Lasers in Medicine, CRC Press, Boca Raton, FL, pp. 27–45, (2002).

[85] Duley, W.W., “Laser Processing and Analysis of Materials”, Plenum Press, New York (1983).

[86] Ready, J.F., “Industrial Applications of Lasers”, Academic Press, San Diego, CA (1997).

[87] Dahotre, N. B. and Harimkar, S. P., “Laser Fabrication and Machining of Materials”, Springer, New York, NY, (2008).

[88] Samant, A.N. and Dahotre, N.B., “Laser machining of structural ceramics—A review”, J. Eur. Ceram. Soc. 29 (6) p. 969 (2009).

[89] Chryssolouris, G., “Laser Machining Theory and Practice”, Springer-Verlag, New York, (1991).

[90] Albright, C., Laser Welding, Machining and Materials Processing. IFS (Publications) Ltd. and Springer-Verlag, New York, (1985).

[91] Springborn, R.K., “Non-traditional machining processes”, American Society of Tool and Manufacturing Engineers, Michigan (1967).

[92] Pandey, P.C., Shan, H.S., “Modern Machining Processes”, McGraw-Hill, New Delhi (1980).

[93] Sun, S., Durandet, Y. and Brandt, M., “Parametric investigation of pulsed Nd:YAG laser cladding of stellite 6 on stainless steel”, Surf. Coat. Technol., 194(2–3), 225–231, (2005).

[94] Islam, M. U. and Campbell, G., “Laser machining of ceramics: A review”, Mater. Manuf. Processes, 1993, 8(6), 611–630, (1993).

[95] Chryssolouris, G., Anifantis, N., Karagiannis, S., “Laser assisted machining: an overview”, Journal of Manufacturing Science and Engineering, Transactions of ASME 119:766–769 (1997).

[96] Gogotsi, Y., Domnich, V., Editors, “High Pressure Surface Science and Engineering”, Institute of Physics Publishing, Bristol, UK, (2004).

[97] Gilman, J.J., “Why silicon is hard”, Science 261, 1436-1439, (1993).

[98] Gilman, J.J., “Shear Induced Metallization”, Philosophical Magazine B, 67, (2) 207-214, (1993).

[99] Pharr, G.M., Oliver, W.C., Cook, R.F., Kirchner, P.D., Kroll, M.C., Dinger, T.R., and Clarke, D.R., “Electrical-Resistance of Metallic Contacts on Silicon and Germanium During Indentation”, J. Mater. Res., 7(4), 961-972, (1992).

[100] Zhang, M., Hobgood, H. M., Demenet, J. L., Pirouz, P., “Transition from Brittle Fracture to Ductile Behavior in 4H-SiC”, JMR, 18 (5) pp. 1087-1095, (2003).

[101] Pirouz, P., “Transition from Brittle Fracture to Ductile Behavior in 4H-SiC”, Philos. Mag. A 78 p. 727, (1998).

[102] Gilman, J.J., “Flow of Covalent Solids at Low Temperatures”, Journal of Applied Physics, 46, (12), 5110-5113, (1975).

[103] Lei, S., Xinwei, S., “Finite Element Analysis of Temperature Distribution and Distinct Element Simulation of Laser Assisted Machining of Silicon Nitride Ceramics”, Proceedings 2005 NSF DMII Grantees Conference, Scottsdale AZ, Grant # DMI-0134579, (2005).

[104] Lei, S., Liu, W., Deines, T., “A Feasibility Study on Laser Assisted Milling of Silicon Nitride Ceramics by Integrating Experimental Study with FEA”, Proceedings 2006 NSF Design, Service and Manufacturing Grantees and Research Conference, St. Louis, MO, Grant # DMI-0134579, (2006).

[105] Stock, M., “Ultrafast Lasers”, Technology Report, Industrial Laser Solutions for Manufacturing 22 (1) pp. 15-16 (2007).

[106] http://www.kjet.com.tw/product/Micromachining with Picosecond Laser Pulses.pdf

[107] Gower, M.C., “Laser micromachining for manufacturing MEMS devices”, Proceedings of the SPIE 4559:53–59, (2001).

[108] Samant, A. N., Daniel, C., Chand, R. H., Blue, C. A. and Dahotre, N. B., “Computational approach to photonic drilling of silicon carbide”, Int. J. Adv. Manuf. Technol., 45: 704-713, (2009).

[109] Sciti, D. and Bellosi, A., “Laser-induced surface drilling of silicon carbide”, Appl. Surf. Sci., 180, 92–101, (2001).

[110] Singh, R., Alberts, M. J. and Melkote, S. N., “Characterization and prediction of the heat-affected zone in a laser-assisted mechanical micromachining process”, Int. J. Mach. Tools Manuf., 48(9), 994–1004, (2008).

[111] Chen, T.C. and Darling, R.B., “Laser micromachining of the materials using in microfluidics by high precision pulsed near and mid-ultraviolet Nd:YAG lasers”, J. Mater. Process. Technol., 98, 248–253, (2008).

[112] Pfefferkorn, F. E., Incropera, F. P., Shin, Y. C., “Heat Transfer Model of Semi-Transparent Ceramics Undergoing Laser-Assisted Machining”, International Journal of Heat and Mass Transfer, Volume 48, Issue 10, pp. 1999-2012, (2005).

[113] Tian, Y. and Shin, Y. C., “Multiscale Finite Element Modeling of Silicon Nitride Ceramics Undergoing Laser-Assisted Machining”, ASME Journal of Manufacturing Science and Engineering, Vol. 129, No.2, pp. 287-295, (2007).

[114] Singh, R.K., Melkote, S.N., “Force Modeling in Laser-Assisted Mechanical Micromachining (LAMM) Process for Hardened Mold Steel”, 2nd International Conference on Micromanufacturing, Clemson University, Sept. 10, (2007).

[115] Lei, S., Shin, Y.C., Incropera, F.P., “Deformation mechanisms and constitutive modeling for silicon nitride undergoing laser-assisted machining”, International Journal of Machine Tools and Manufacture, Volume 40, Issue 15, Pages 2213-2233, (2000).

[116] Lei, S., Shin, Y. C. and Incropera, F. P., “Experimental investigation of thermo-mechanical characteristics in laser-assisted machining of silicon nitride ceramics”, J. Manuf. Sci. Eng., 123, 639–646, (2001).

[117] Rozzi, J. C., Pfefferkorn, F. E., Incropera, F. P. and Shin, Y. C., “Transient thermal response of a rotating cylindrical silicon nitride workpiece subjected to a translating laser heat source. Part I. Comparison of surface

temperature measurements with theoretical results”, J. Heat Transfer, 120, 899–906, (1998).

[118] Rozzi, J. C., Incropera, F. P. and Shin, Y. C., “Transient thermal response of a rotating cylindrical silicon nitride workpiece subjected to a translating laser heat source. Part II. Parametric effects and assessment of a simplified model”, J. Heat Transfer, 120, 907–915, (1998).

[119] Rozzi, J. C., Pfefferkorn, F. E., Incropera, F. P. and Shin, Y. C., “Transient, three-dimensional heat transfer model for the laser assisted machining of silicon nitride. I. Comparison of predictions with measured surface temperature histories”, Int. J. Heat Mass Transfer, 2000, 43(8), 1409–1424, (2000).

[120] Rozzi, J. C., Incropera, F. P. and Shin, Y. C., “Transient, three-dimensional heat transfer model for the laser assisted machining of silicon nitride. II. Assessment of parametric effects”, Int. J. Heat Mass Transfer, 43(8), 1425–1437, (2000).

[121] Pfefferkorn, F.E., Shin, Y.C., Tian, Y. and Incropera, F.P., “Laser-assisted machining of magnesia-partially-stabilized zirconia”, J. Manuf. Sci. Eng., 126, 42–51, (2004).

[122] Chang, C.W. and Kuo, C.P., “An investigation of laser-assisted machining of Al_2O_3 ceramics planning”, Int. J. Mach. Tools Manuf., 47(3–4), 452–461, (2008).

[123] O'Connor, B.P., Marsh, E.R., Couey, J.A., “On The Effect of Crystallographic Orientation On Ductile Material Removal in Silicon”, Precision Engineering 29 (1), pp. 124-132, (2004).

[124] Blackley, W. S., Scattergood, R.O., “Ductile Regime Model for Diamond Turning of Brittle Materials”, Precision Engineering, 13 (2), p: 95-102, (1991).

[125] Zhang, M., Zarudi, I., “Towards a Deeper Understanding of Plastic Deformation in Mono-Crystalline Silicon”, Int. Mech. Sci., 43, pp. 1985-1996 (2001).

[126] Noreyan, A., Amar, J.G., Marinescu, I., “Molecular Dynamics Simulations of Nanoindentation of Beta-SiC with Diamond Indenter”, Materials Science & Engineering B 117, 235, (2005).

[127] Komanduri, R., Raff, L.M., “A Review On The Molecular Dynamics Simulation of Machining at The Atomic Scale”, Proceedings of the I MECH E Part B Journal of Engineering Manufacture 215 (12), pp. 1639-1672, (2001).

[128] Cheong, W.C.D., Zhang, L.C., “Molecular Dynamics Simulation of Phase Transformations in Silicon Monocrystals Due to Nano Indentation”, Nanotechnology 11, pp. 173-180, (2000).

[129] Blake, P.N., Bifano, T.G., Dow, T. A., Scattergood, R.O., “Precision machining of ceramic materials”, Ceram. Bull., vol.67, 1038-1044, (1988).

[130] Jang, J., Lance, M.J., Wen, S.Q., Ting Y. Tsui and Pharr, G. M., “Indentation-induced gogtsıs in silicon: influences of load, rate and indenter angle on the transformation behavior”, Acta Materialia 53, 1759-1770, (2005).

[131] Demangeot, F, Puech, P, Domnich, V., “Raman mapping devoted to the phase transformation and strain analysis in Si micro-indentation”, Adv. Eng. Mater., 4(8), 543-546, (2002).

[132] Juliano, T, Domnich, V, Gogotsi, Y., “Examining pressure-induced phase transformations in silicon by spherical indentation and Raman spectroscopy: A statistical study”, J MATER RES 19 (10): 3099-3108, (2004).

[133] Ge, D.B., Domnich, V, Gogotsi, Y., “High-resolution transmission electron microscopy study of metastable silicon phases produced by nanoindentation”, J. Appl. Phys., 93 (5), 2418-2423, (2003).

[134] Ge, D.B., “TEM investigation of contact loading induced phase transformation in silicon”, Dissertation, Drexel University, (2004).

[135] Lewis, S.P., Cohen, M.L., “Theoretical study of high-pressure orthorhombic silicon”, Physical Review B, 48(21), 144-147, (1993).

[136] Patten, J.A., “High pressure phase transformation analysis and molecular dynamics simulations of single point diamond turning of germanium”,

Ph.D. Dissertation, North Carolina State University, Department of Mechanical Engineering, (1996).

[137] Gilman, J.J., "Mechanism of shear-induced metallization", CZECH J PHYS 45 (11), 913-919, (1995).

[138] Gilman, J.J., "Electro-plastic effect in semiconductors", MAT SCI ENG A-STRUCT 287 (2), 272-275, (2000).

[139] Zarudi I., Zou J., McBride W., "Amorphous structures induced in monocrystalline silicon by mechanical loading", APPLIED PHYSICS LETTERS 85 (6), 932-934, (2004).

[140] http://www.cree.com/products/pdf/MAT-CATALOG00L.pdf

[141] http://www.universitywafer.com

[142] Wilks, J., "Performance of Diamonds as Cutting Tools for Precesion Machining", Journal of Precision Engineering, v 2 (2), pp. 57-72, (1980).

[143] http://www.cetr.com/Brochures/CETR2005_Brochures/CETR2005UMT_web_01.htm

[144] Palik, E.D., "Handbook of Optical Constants of Solids", New York: Academic Press, (1998).

[145] http://www.ee.byu.edu/photonics/opticalconstants.phtml

[146] Hanfland, M., Alouani, M., Syassen, K., & Christensen, N. E., "Optical Properties of Metallic Silicon", Physical Review B , 38 (18), (1988).

[147] Laine, A. D., Mezzasalma, A. M., Mondio, G., Parisi, P., Cubiotti, G., & Kucherenko, Y. N., "Optical Properties of Cubic Silicon Carbide", Journal of Electron Spectroscopy and Related Phenomena, 93, 251-257, (1998).

[148] Zollner, S., Chen, J. G., Duda, E., Wetteroth, T., Wilson, S. R., & Hilfiker, J. N., "Dielectric functions of bulk 4H and 6H SiC and spectroscopic ellipsometry studies of thin SiC films on Si", Journal of Applied Physics , 85 (12), 8353-8361, (1999).

[149] Forouhi, A.R., & Bloomer, I., "Optical Properties of Crystalline Semiconductors and Dielectrics", Phys. Rev. B., 38 (3), 1865-1874, (1988).

[150] Dong, L. and Patten, J.A., Unpublished work, UNC Charlotte, (2005).

[151] Yonenaga, I., Hoshi, T. and Usui, A., "High-Temperature Hardness of Bulk Single-Crystal Gallium Nitride- in Comparison with Other Wide-Gap Materials", J. Phys.: Condens. Matter 12 10319-10323, (2000).

[152] Pfefferkorn F.E., Lei S., Jeon Y., and Haddad G., "A metric for defining the energy efficiency of thermally assisted machining", International Journal of Machine Tools & Manufacture 49, 357-365, (2009).

[153] Ajjarapu S.K., Cherukuri, H., Patten, J., Brand, C.J., "Numerical Simulations of Ductile Regime Machining of Silicon Nitride using Drucker Prager model", Proc. Inst. Mech. Engrs., 218 (C), pp. 1-6, (2004).

[154] Shim, S., Jang, J-I., Pharr, G.M., "Extraction of flow properties of Single Crystal Silicon Carbide by Nanoindentation and Finite Element Simulation," Act. Materia., 58, pp. 3824-3832, (2008).

[155] Yonenaga, I., "Thermo-Mechanical Stability of Wide-Bandgap Semiconductors:High Temperature Hardness of SiC, AlN, GaN, ZnO and ZnSe," Physica B. (308-310), pp. 1150-1152, (2001).

[156] Yonenaga, I., Hoshi, T., Usui, A., "High Temperature Strength of III-IV Nitride Crystals," J. Phys: Condens. Matter, 14, pp. 12947-12951, (2000).

[157] Samant, A.V., Zhou, W.L., Pirouz, P., "Effect of Test Temperature and Strain Rate on the Yield Stress of Monocrystalline 6H-SiC," Phys. Stat. Sol. (a) 166, pp. 155, (1998).

[158] Tsvetkov, V.F., Allen, S.T., Kong, H.S., Carter, C.H., "Recent Progress in SiC Crystal Growth," Inst. of Phys. Serial No. 142, pp. 17, (1996).

[159] Naylor, M.G., Page, T.F., "The effect of temperature and load on the indentation hardness behavior of Silicon Carbide engineering ceramics", Proceedings of International Conference on Erosion of Soil and Impact, pp. 32, (1979).

[160] Virkar, S., "Numerical Simulations and Analysis of Ductile mode Micro Laser Assisted Machining of Silicon Carbide", Master's Thesis, Western Michigan University, (2010).

[161] Gupta, M.C., Ruoff, A.L.,"Static compression of silicon in the [100] and in the [111] directions", Journal of applied physics 51 (2), 1072-1075 (1980).

[162] Kobliska, R.J. and Solin, S.A., “Raman Spectrum of Wurtzite Silicon”, Phys. Rev. B, Vol.8, pp. 3799-3802, (1973).

[163] Gogotsi, Y.G., Kailer, A. and Nickel, K.G., “Phase transformations in materials studied by micro-Raman spectroscopy of indentations”, Mater. Res. Innovat. 1, pp. 3–9, (1997).

[164] Lucazeau, G. and Abello, L., “Micro-Raman analysis of residual stresses and phase transformations in crystalline silicon under microindentation”, J. Mater. Res., 12, pp. 2262, (1997).

[165] Domnich, V. and Gogotsi, Y., “Phase transformation in silicon under contact loading”, Rev. Adv. Mater. Sci., vol. 3, 1-36 (2002).

[166] Yan, J., Asami, T., Harada, H., Kuriyagawa, T., “Fundamental investigation of subsurface damage in single crystalline silicon caused by diamond machining”, Precision Engineering 33, pp. 378–386, (2009).

Appendix-1 Heat Calculations

The cross-sectional area of scratch with laser is computed as:

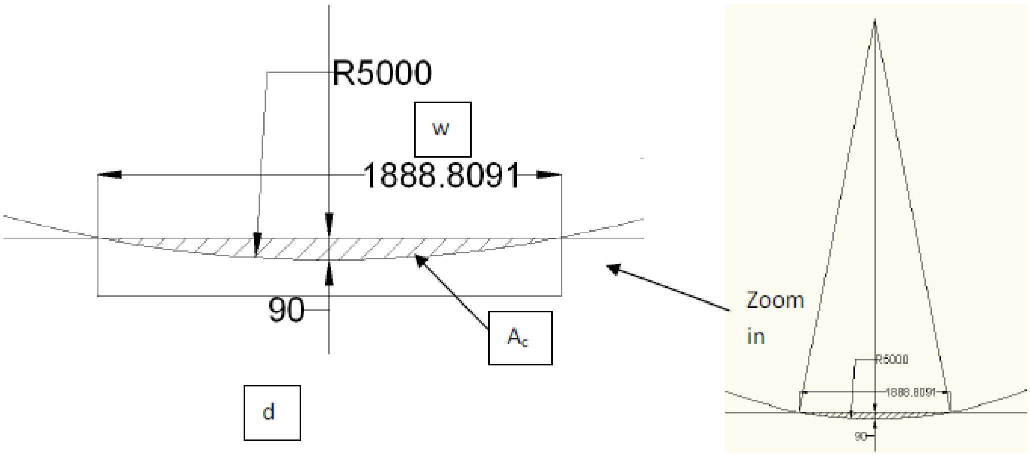

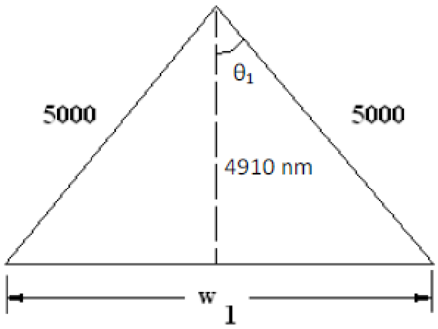

Sketch of the d = 90 nm deep scratch on 4H-SiC,

R: radius of cutting tool tip,

w: width of scratch;

A_c: Crescent Area (the units in the figure are in nm).

$w_1 = 2\sqrt{5000^2 - 4910^2}$=1889nm=1.89µm

$\theta_1 = \cos^{-1}\left(\frac{4910}{5000}\right) = 10.88^o$

$2\theta_1 = 21.76^o$

$$A_c = \pi R^2\left(\frac{2\theta}{360°}\right) - \frac{1}{2}(4910)(1890) = 0.10735\mu m^2 = 1.7035\times 10^{-13} m^2$$

Since the cutting speed (v_c) is 1 μm/sec, therefore the volume being swept per second is:

$$\dot{V} = A_c.v_c = 0.10735.10^{-13}(\frac{1\mu m}{sec}) = 1.0735.10^{-19} m^3/sec$$

Absorbed heat by the machined substrate,

considering ρ = 3211 kg/m^3,

C = 682 J/kg.K, and

ΔT = 700 - 25 = 675K is given by:

$$\dot{Q} = \dot{m}.C.\Delta T = \rho.\dot{V}.C.\Delta T = 1.0735.10^{-19}.3211.682.675 = 1.59\frac{10^{-10}J}{sec} \approx 0.16\ (nW)$$

Melting heat for the 4H-SiC, considering ρ =3211 kg/m3, C=682 J/Kg.K; melting point of

Tm=3200°C, ΔT=3200-25=3175K,

and 10% latent heat is given by;

$$\dot{Q} = 1.1\dot{m}.C.\Delta T = \rho.\dot{V}_1.C.\Delta T = (1.1)1.0735.10^{-19}.3211.682.3175 \approx 0.82(nW)$$

Appendix-2 1480nm IR Laser Diode

FOL1425RUZ-317
FLT-A4316
A4316A01

L-I curve

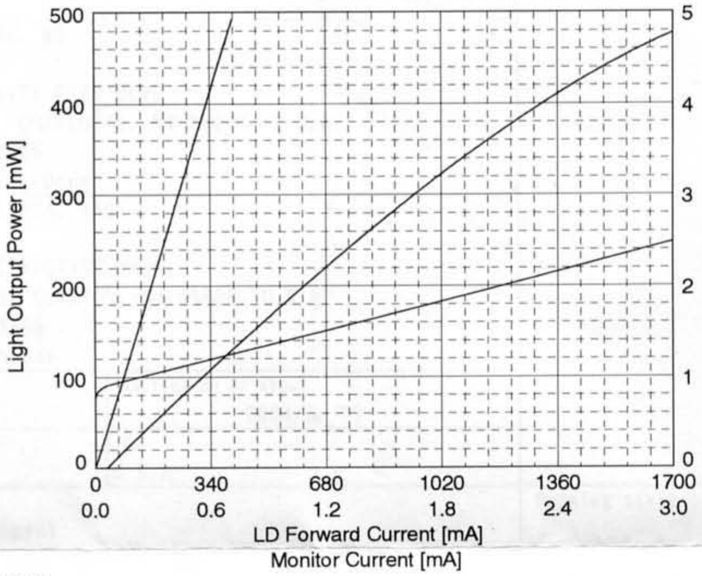

Spectrum

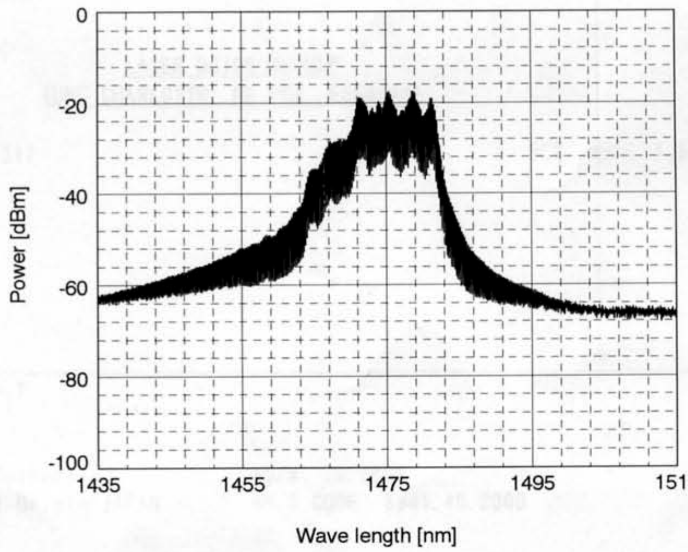

Measured at Ts=25℃, Tc=70℃

Item	Serial#	Threshold Current	Forward Current If(BOL)	Optical Output Power(Pf)	Forward Voltage	Monitor Current	Center Wavelength RMS	Spectral Width RMS	TEC Current	TEC Voltage
Condition			@Pf		@Pf	@Pf	@Pf	@Pf	@If(BOL) × 1.2	@If(BOL) × 1.2
Unit		mA	mA	mW	V	mA	nm	nm	A	V
Test Data	A4316A01	36.3	1318.6	400	2.11	0.583	1475.8	3.7	2.532	2.90